Photochemical Properties and Ultrafast Dynamics of Azobenzene-Functionalized Gold Nanoparticles

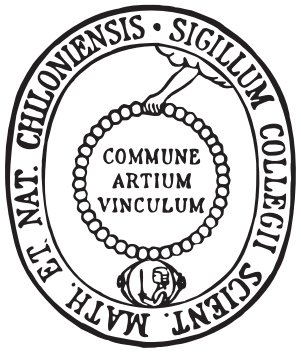

Dissertation

zur Erlangung des Doktorgrades

der Mathematisch-Naturwissenschaftlichen Fakultät

der Christian-Albrechts-Universität zu Kiel

vorgelegt von

Anja Köhntopp

Kiel 2015

Erster Gutachter: Prof. Dr. Friedrich Temps
Zweiter Gutachter: Prof. Dr. Gernot Friedrichs

Tag der mündlichen Prüfung: 14. Dezember 2015
Zum Druck genehmigt: 14. Dezember 2015

gez. Prof. Dr. Wolfgang J. Duschl, Dekan

ERKLÄRUNG

Hiermit erkläre ich, dass die vorliegende Abhandlung - abgesehen von der Beratung durch meinen Betreuer Prof. Dr. Friedrich Temps - nach Inhalt und Form meine eigene Arbeit ist. Diese Arbeit hat weder in Auszügen noch in ganzer Form einer anderen Stelle im Rahmen eines Prüfungsverfahrens vorgelegen. Sie wurde in ihrer Gesamtheit nicht veröffentlicht und auch nicht zur Veröffentlichung eingereicht. Teile dieser Arbeit wurden in fachwissenschaftlichen Zeitschriften veröffentlicht oder zur Veröffentlichung eingereicht. Dies bezieht sich auf die folgenden Kapitel:

Kapitel 3
A. Köhntopp, A. Dabrowski, M. Malicki, F. Temps, Photoisomerisation and ligand-controlled reversible aggregation of azobenzene-functionalised gold nanoparticles, *Chem. Commun.* **2014**, *50*, 10105-10107.

Kapitel 4
A. Köhntopp, M. Dittner, F. Temps, Femtosecond Time-Resolved Dynamics of *trans*-Azobenzene on Gold Nanoparticles, *to be submitted to J. Phys. Chem. Lett.*.

Die Arbeit ist unter Einhaltung der Regeln guter wissenschaftlicher Praxis der Deutschen Forschungsgemeinschaft entstanden.

Kiel, im Oktober 2015

Anja Köhntopp

ABSTRACT

The main goal of the present Thesis was the investigation of the photo-induced isomerization processes of azobenzenes (ABs) attached to small gold nanoparticles (AuNPs) by static and femtosecond time-resolved transient absorption spectroscopy. ABs functionalized with thiolated alkyl linker chains of three different lengths (C3, C7, C11) were brought onto the surface of ~ 4 nm diameter AuNPs in a mixed self-assembled monolayer (mSAM) with decanethiol or pentanethiol as co-ligand. The AB-functionalized AuNPs show excellent photoisomerization yields independent from the linker chain length and without degradation over several subsequent *trans-cis* and *cis-trans* isomerization cycles. AuNPs functionalized with ABs bearing long alkyl linker chains (C7, C11) and short co-ligands (pentanethiol) reversibly aggregate when switched to their *cis* state and disaggregate when isomerized back to their *trans* state. The time-resolved absorption data reveal excited-state absorption of AB around $\lambda = 400$ nm and strong signals of the simultaneously excited localized surface plasmon resonance (LSPR). The excited-state dynamics of AB show surprisingly little difference compared to the AB dynamics in solution, leading to the conclusion that the AB photochrome and the AuNP core are efficiently decoupled by the long (C11) linker chain. Furthermore, the excited-state dynamics of the *push-pull* substituted AB derivative Disperse Red 1 (DR-1) in a mSAM with decanethiol on a AuNP surface were investigated. The results hint at substantial energy and charge-transfer from the excited AuNP into the ligand, which significantly alters the excited-state absorption of DR-1. The close proximity of the $\pi\pi^*$ absorption of DR-1 and the LSPR should play an essential role for this effect.

A second goal of this Thesis was the spectroscopic investigation of the ultrafast relaxation dynamics of functionalized AuNPs themselves, especially the hot electron cooling dynamics, and how they are influenced by different ligands. AB-functionalized AuNPs show the same hot electron lifetime of $\tau_{\text{e-ph}} \approx 2$ ps as purely decanethiol functionalized AuNPs, revealing that the electronic states of AB do not participate in the electron cooling process. A study investigating the influence of (i) the ligand heat capacity and (ii) resonant coupling between ligand absorption band and LSPR was performed for AuNPs functionalized with (i) naphthol- and phenanthrol-thiolates and (ii) coumarin- and DR-1-thiolates. The same hot electron lifetimes of $\tau_{\text{e-ph}} \approx 2$ ps were extracted from the transient absorption data for all investigated samples, suggesting that neither of the two factors has significant influence on the relaxation dynamics of AuNPs.

ZUSAMMENFASSUNG

Das Hauptziel dieser Arbeit war die Untersuchung der Photoisomerisierung von Azobenzolen (ABs) gebunden an Goldnanopartikel (AuNPs) mittels statischer und femtosekunden-zeitaufgelöster transienter Absorptionsspektroskopie. Die ~ 4 nm großen AuNPs wurden mit gemischten Monolagen (mSAMs) aus einem von drei verschiedenen AB-Derivaten mit unterschiedlichen Alkylkettenlängen (C3, C7, C11) und Decanthiol bzw. Pentanthiol funktionalisiert. Diese AB-funktionalisierten AuNPs können unabhängig von der Linkerkettenlänge des AB-Liganden mit hohen Ausbeuten mehrmals zwischen zwei definierten photostationären Zuständen hin und her geschaltet werden, ohne dass Ermüdungserscheinungen sichtbar werden. Zusätzlich dazu zeigen AuNPs, welche mit einer Kombination aus einem langkettigen AB-Liganden (C7 oder C11) und kurzkettigem Pentanthiol beschichtet sind, photoinduzierte und vollständig reversible Aggregation im *cis*-Zustand. Die zeitaufgelösten Absorptionsdaten zeigen ein Signal im Bereich von 400 nm, das dem AB-Chromophor zugeordnet werden kann, sowie intensive Signale der Plasmonresonanzbande (LSPR) der AuNPs über den gesamten gemessenen Wellenlängenbereich. Die ultraschnelle Dynamik des ABs auf den AuNPs zeigt überraschend geringe Unterschiede zur bekannten AB-Dynamik in Lösung. Dies deutet darauf hin, dass die AB-Einheit und der AuNP-Kern durch die lange Linkerkette (C11) effizient entkoppelt werden. Untersuchungen von AuNPs mit einer mSAM aus Decanthiol und dem *push-pull*-substituierten AB-Derivat Dispersrot 1 (DR-1) offenbaren einen erheblichen Energie- und Ladungstransfer vom angeregten AuNP zum Liganden, der die Absorption des DR-1 aus dem angeregten Zustand stark beeinflusst. Die Nahe-Resonanz der $\pi\pi^*$-Absorptionsbande des DR-1 zur LSPR des AuNP dürfte dabei eine wesentliche Rolle spielen.

Das zweite Ziel dieser Arbeit war die Untersuchung der Abkühlungsdynamik der AuNP, insbesondere der e-ph-Kopplung, und des Einflusses verschiedener Liganden darauf. AB-funktionalisierte NP zeigen die gleiche Abkühlungskonstante von $\tau_{\text{e-ph}} \approx 2$ ps wie rein Decanthiol-beschichtete AuNP, was deutlich macht, dass die elektronischen Zustände des AB-Liganden nicht an der Relaxation des AuNP beteiligt sind. Eine Untersuchung des Einflusses (i) der Wärmekapazität der Liganden und (ii) einer möglichen resonanten Kopplung zwischen der Ligandenabsorptionsbande und der LSPR des Goldkerns wurde anhand von AuNPs funktionalisiert mit (i) Naphthol- und Phenanthrolthiolen und (ii) Coumarin- und DR-1-thiolen durchgeführt. In allen untersuchten Systemen wurde eine Abkühlungskonstante von $\tau_{\text{e-ph}} \approx 2$ ps gefunden, was zeigt, dass keiner der beiden Faktoren die Relaxationsdynamik der AuNP wesentlich beeinflusst.

CONTENTS

Part I

INTRODUCTION AND EXPERIMENTAL PART

1

INTRODUCTION

Modern technology is present in virtually all areas of life nowadays, from displays and memory devices in modern electronics over sensors and optical devices to drug delivery systems and biofunctionalized medical implants. New functional materials therefore comprise an amazingly large area of scientific research.

The development of digital memory devices exemplifies the need for increasingly sophisticated methods to tailor material properties for specific applications. Punch cards represent the earliest form of digital memory devices on which the information is stored as a pattern of holes in specific positions. Optical memory devices such as CDs and DVDs have the data engraved into a transmissive polycarbonate disc in the form of a sequence of small indentations. The disc is coated with a thin aluminium layer and for read-out it is scanned with a laser that detects the indentations through differences in light reflection.[1] Modern memory devices such as flash drives and solid state drives use tiny semiconductive elements to store and access information electronically[2] and the individual building blocks of such devices are constantly being improved. For example, many field-effect transistors (FET) based on organic semiconductors now use gold nanoparticles (AuNPs) as charge carrier traps to enhance their performance, i.e. the response time, the contrast between ``on'' and ``off'' states, and the stability of both states.[3–7] In addition, this strategy allows for fast and easy manufacturing of the layers from solution in comparison to high vacuum layer deposition techniques required for the commonly used FETs with a thin metal layer embedded between two dielectric layers.[4]

Further improvement of the device performance can be achieved through functionalization of the AuNPs with organic molecules, e.g. photochromic molecular switches such as azobenzene (AB). For example, Tseng et al. constructed an organic FET (OFET) in which AuNPs covered with a self-assembled monolayer (SAM) of thiolated ABs were positioned at the interface of a dielectric insulating SiO_2 layer and a semiconducting pentacene film.[8] The incorporation of AB introduces additional charge trapping sites and the charge trapping process in the AuNPs is more efficient because the monolayer acts as a barrier between the AuNP and its surroundings. Therefore, an accelerated response time, a higher contrast between on and off state, and a longer retention time (time the information can be stored) compared to devices using simple alkylated AuNPs is achieved. While in this example the AB layer is used simply as a charge trap and to

isolate the single AuNPs from the semiconducting layer, Samori and coworkers built an OFET that also benefits from the photochromic capabilites of AB.[9] To these ends, they embedded AuNPs coated with SAMs of a thiol-substituted azo-biphenyl into the organic semiconducting layer comprised of poly(3-hexylthiophene). The azo units are initially present in their *trans* form. Upon irradiation with UV light they can be switched to the *cis* form, which induces a variation of the tunneling barrier between AuNP and semiconductor. In this manner, the current passing through the device can be modulated by light. Thus, the OFET can not only be controlled electrically, as conventional transistors, but also photochemically with light.

These two examples comprise only a small selection of cases where the functionality of a complex system is based on the systematic combination of different materials and building blocks which interact with each other in a specific way. For the conscious design of such devices, good understanding of the specific interactions of the different components is required. The literature already offers a great number of publications concerned with the basic properties of AuNPs in different environments and coated with a multitude of organic molecules, e.g. alkylthiols, amines, acids, organic dyes, DNA building blocks, and other biologically relevant substances.[10–18] However, the currently available works concerned with molecular switches on AuNPs mainly focus on the effects of light-induced switching of the photochromic molecules[19–23] and less on the details of the switching process itself.

This Thesis investigates the interactions of AuNPs and organic molecules, especially photochromic ABs, immobilized on the metal surface and their ultrafast dynamics using femtosecond time-resolved transient absorption spectroscopy. The present introduction gives an overview of the unique optical properties of AuNPs and describes the influences which different environments exert on them. Special attention is paid to the dynamics of AuNPs after photoexcitation and the interactions between AuNP and organic ligands. The photochromic properties of AB and its dynamics are presented in short and the current state of research on photochromic molecules on AuNPs is summarized.

1.1 GOLD NANOPARTICLES

Metal nanoparticles have been used for medical and decorative purposes for centuries. During the middle ages gold colloids were considered to be able to cure various diseases, such as heart problems, dysentery, epilepsy and tumors. In the 15th century, Italian ceramicists used a fine glaze containing copper and silver nanoparticles to give their works a metallic or iridescent look as in the lustered plate shown in Figure 1.1 (left). Since ancient Roman times, silver and

gold nanoparticles have been used to color glass. Many examples can still be admired today in the ornate stained glass windows of gothic churches, cathedrals and castles. The window in Figure 1.1 (right) is a Swiss armourial glass from 1564 showing the Arms of Unterwalden in which silver and gold nanoparticles were used to stain the glass, giving it its vibrant colours.[24]

Figure 1.1: Left: Lustered Armorial Plate, Gubbio, Italy, 1524. The J. Paul Getty Museum, Los Angeles. © The J. Paul Getty Museum.
Right: Swiss armourial Glass of the Arms of Unterwalden, 1564, with typical painted details, extensive silver stain and flashed ruby glass, Sułkowski castle in Bielsko-Biała, Poland.[24]

Although colored glasses and ceramics utilizing the optical properties of noble metal nanoparticles have been manufactured for several millenia,[25] the nature of nanoparticles was unknown until the mid 19th century. In 1857 Michael Faraday was the first to explain the bright red color of gold stained glass with the presence of very finely divided colloidal gold, gold nanoparticles (AuNPs) as we call them today.[26] He also observed that thin films of dried gold nanoparticle solutions reversibly changed color from bluish-purple to green upon compression, indicating the great importance of particle size and environmental conditions for the optical properties of AuNPs. Another important milestone in the investigation of AuNPs are the works published by Gustav Mie in 1908 which explain the optical properties of spherical metal nanoparticles theoretically. Mie solved Maxwell's equations with the appropriate boundary conditions to obtain a quantitative description of the absorption properties of spherical NPs.[27] In the 20th century a number of simple and reliable methods for the synthesis of AuNPs have been developed and since the groundbreaking publications of Brust in the 1990s research in the area has increased tremendously.[28,29] Brust's method allows for the preparation of AuNPs stabilized with organic thiols in organic sol-

vents, a simple concept that is extremely versatile and widely used nowadays.

As the optical properties and not the synthesis and structural characterization of AuNPs were in the focus of this Thesis, only the former shall be discussed here. Detailed information on the latter two topics can be found in the literature.[10,30–34]

1.1.1 Optical Properties of Gold Nanoparticles

The strikingly bright red color of AuNP solutions, which sparked interest in their decorative use in the first place, is the most prominent of the unique size-dependent optical, electronic, and chemical properties of AuNPs. In order to give an introduction into the fundamental aspects of spectroscopic investigations on functionalized AuNPs, the optical properties of AuNPs and the basic physics with which they can be described shall be presented in the following. Special attention is paid to the strong influences of particle size and environment on the optical properties as their complex relationship is essential for the systematic investigation of functionalized AuNPs. Furthermore, some examples for the application of functionalized AuNPs are given to emphasize their great potential.

The red color of AuNP solutions is due to an absorption band in the visible, the Localized Surface Plasmon Resonance (LSPR) band. The absorption is caused by a collective oscillation of the conduction band electrons induced by incident light. The electric field of the light induces a uniform polarization over the whole AuNP, dislocating the free moving conduction band electrons from the positively charged Au atom cores. The arising linear restoring force causes the electrons to oscillate around the Au core with the frequency of the incident light, as schematically shown in Figure 1.2.

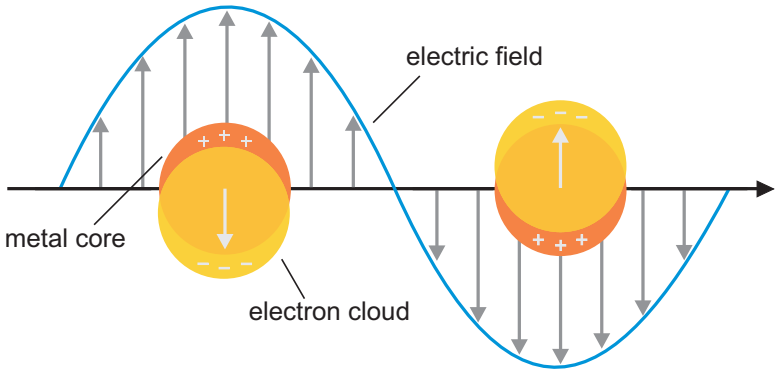

Figure 1.2: Schematic representation of the polarization induced in a AuNP by a light wave with a wavelength larger than the NP diameter.

If the frequency of the incoming light is resonant with the oscillation frequency of the conduction electrons, a strong absorption oc-

curs, the LSPR. The absorption cross section of AuNPs is very large (see below), larger even than the absorption coefficient of highly absorbing dyes.[35–38]

Gold nanoparticles possess a large number of electronic states that come together in bands similar to the situation in bulk metals. As gold has a $5d^{10}\,6s^{1}$ structure, the valence band containing the d electrons is completely filled, the conduction band containing the s electrons is half-filled. In addition to the LSPR, intraband transitions within the conduction band ($s \rightarrow s$) and interband transitions from the valence band to the conduction band ($d \rightarrow s$) can occur. The intraband transitions lie at lower energies than the LSPR. The onset of the interband transitions occurs at ~ 2.4 eV very close to the LSPR. In the spectra the overlap of LSPR and interband transitions leads to an asymmetric LSPR lineshape and the presence of a strong absorption at energies higher than the LSPR frequency.[11]

Mie theory mathematically describes the interaction of an electromagnetic lightwave with small metal spheres in dependence of the material dielectric constant ϵ. The absorption cross section σ_{abs} of nanoparticles is subsequently described by a series of multipole oscillations. For NPs much smaller than the wavelength of the light only the dipole oscillation contributes significantly to σ_{abs} (dipole approximation)[11,39]. Scattering effects can also be neglected, thus the resulting Mie theory expression is:

$$\sigma_{abs}(\omega) = 9\frac{\omega}{c}\epsilon_m^{3/2} V \frac{\epsilon''(\omega)}{[\epsilon'(\omega) + 2\epsilon_m]^2 + \epsilon''(\omega)^2}. \tag{1.1}$$

Here, V is the particle volume, ω is the angular frequency of the light, and ϵ_m and $\epsilon(\omega) = \epsilon'(\omega) + i\epsilon''(\omega)$ are the dielectric functions of the surrounding medium and the NP material, respectively, with the real part $\epsilon'(\omega)$ and the imaginary part $i\epsilon''(\omega)$. The resonance condition is approximately fullfilled when $\epsilon'(\omega) = -2\epsilon_m$, if ϵ'' is small or only weakly dependent on ω. The resonance position is given by $\omega = \omega_P/\sqrt{1 + 2\epsilon_m}$.[11]

Even though equation 1.1 suggests that the absorption spectra of small AuNPs are size-independent, a size dependence is observed experimentally.[39,40] The position as well as the bandwidth of the LSPR change dramatically with the AuNP size.[39] As shown in Figure 1.3, for particles of 22 nm size it appears at approximately 520 nm and is relativly sharp with a bandwidth of $\Delta\lambda \approx 80$ nm. As the particle size increases the LSPR is red-shifted and broadened so that in nanoparticles with a diameter of 100 nm it appears at 575 nm with a bandwidth of $\Delta\lambda \approx 150$ nm. For particles smaller than 20 nm the LSPR is slightly blue-shifted, broadened and decreases in intensity until it finally vanishes for particles smaller than ≈ 2 nm.[39–42]

The LSPR bandwidth is associated with the dephasing time of the coherent electron oscillation, faster dephasing results in a broader

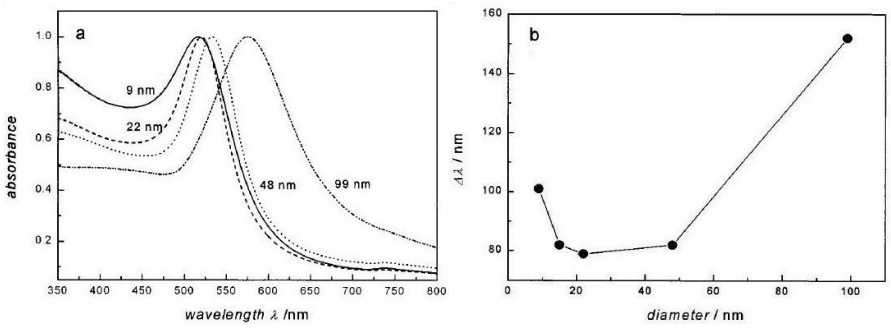

Figure 1.3: (a) Size-dependent shift of the LSPR maximum, shown are the absorption spectra of 9 nm, 22 nm, 48 nm and 99 nm sized AuNPs. (b) Change of the LSPR bandwidth $\Delta\lambda$ with the AuNP particle size. Adapted with permission from S. Link and M. A. El-Sayed *J. Phys. Chem. B* 1999, *103* (21), 4212-4217. Copyright 1999, American Chemical Society.

plasmon resonance. In small AuNPs the loss of coherence is accelerated due to increased electron scattering on the NP surface as the particle size becomes smaller than the mean free path of the electrons ($\approx$ 40-50 nm in bulk gold).[11,39] Therefore, small AuNPs ($d \leqslant 5$ nm) exhibit broadened LSPR bands compared to AuNPs of $d \approx 20$ nm. The dephasing time can directly be calculated from the absorption spectra: For AuNPs of 22, 44, and 99 nm size one obtains 4.1, 3.9, and 2.6 fs, respectively.[41]

For core sizes smaller than $\approx$ 2 nm sharp spectral features have been observed, indicating a molecule-like electronic structure with separated energy levels instead of electronic bands found in bulk metals.[42] Generally, the electronic structure of larger AuNPs is regarded to be analogous to bulk metals, where the electronic states form bands in which the electrons can move freely between the states. As AuNPs become smaller the density of electronic states decreases until they can no longer be considered continuous. Thus, for particles smaller than 20 nm the bulk dielectric function no longer describes the real situation, and $\epsilon(\omega)$ becomes size-dependent.[11,39] To account for the size dependence, $\epsilon(\omega)$ is written as the sum of dielectric functions of the bound (valence band) electrons ϵ_{bound} and the free (conduction band) electrons ϵ_{free}. The latter is described by the Drude model

$$\epsilon_{\text{free}}(\omega, r) = 1 - \frac{\omega_P^2}{\omega^2 + i\gamma_{\text{free}}\omega}, \tag{1.2}$$

with ω_P being the bulk plasmon frequency, and γ_{free} being a damping constant related to the lifetimes of all electron scattering processes in the AuNP, including electron-surface scattering. γ_{free} is size-dependent through

$$\gamma_{\text{free}}(r) = \gamma_0 + \frac{A\nu_F}{r} \tag{1.3}$$

wherein γ_0 is the damping constant in the bulk material, A is a theory-dependent parameter, v_F is the Fermi velocity of the electrons, and r is the particle radius. For small AuNPs one thus finds an intrinsic size dependence, as the absorption cross section is size-dependent only indirectly through ϵ. In contrast to that, for AuNPs with a diameter larger than $d \approx 20$ nm the dipole approximation is no longer valid and σ_{abs} directly depends on the particle radius r (extrinsic size regime).[39]

Classical Mie theory is strictly limited to spherical particles. To describe spheroidal particles, the generalization introduced by Richard Gans in 1912 has to be used.[43] The Gans theory considers the three dimensions of the particle to each have a different depolarization factor and finds an analytical solution for spheroidal particles. For particles with more complex shapes the solutions to Maxwell's equations have to be found numerically using different methods, e.g. finite difference time domain (FDTD), discrete dipole approximation (DDA), or the finite element method (FEM).[14,44] A number of extensions to Mie theory considering different effects , e.g. core shell particles, substrate effects, nonlinear optical effects and non-uniform illumination of particles, have been made over the years. A detailed description is beyond the scope of this Thesis and can be found in the literature.[11]

To describe AuNPs at elevated temperatures, e.g. after photoexcitation, a temperature-dependent Mie theory model is needed. Therein σ_{abs} is temperature-dependent through the dielectric function of the bound electrons ϵ_{bound}. In this Thesis, this model is used to analyze the transient absorption data of functionalized AuNPs and will be explained in detail in Chapter 2.3.2, where it is applied to the measured UV/Vis spectra of AuNPs.

In addition to its size dependence, the LSPR is very sensitive to changes in the AuNP surroundings.[11,12,14,45–49] The dielectric constant of the surrounding medium enters into equation (1.1), thus directly influencing the absorption. There are essentially two ways to change the refractive index of the AuNP surroundings: (i) Exchanging the surrounding matrix (solid or liquid) with a substance of different refractive index, and (ii) the attachment of ligands to the AuNP surface. Both variations are accomplished fairly easily and have been reported in the literature many times.[12,13,50–56] For example, Kreibig et al. investigated 2 nm sized silver nanoparticles (AgNPs) in vacuum, deposited onto a SiO_2 surface or embedded in a SiO_2 matrix, and found considerable differences in LSPR position and bandwidth.[12] For colloidal ligand-functionalized AuNPs dispersed in a solvent it will be shown in this Thesis, that it is questionable whether the continuum dielectric constant of the solvent can fully account for the shape of the spectrum, as the ligand sphere introduces a local change. In a more application-oriented approach, Chen et al. successfully used the LSPR shift of thiol-functionalized AuNPs, AgNPs and

gold nanoshells upon adsorption of volatile organic compounds, e.g. 1-pentanol, toluene, anisole, chlorobenzene and pyridine, to construct a sensor for the specific detection of nine different compounds.[53,54]

In fact, AuNPs are frequently used for sensing applications, especially the fields of medicine and biosensing seem to offer endless application possibilities.[10,14,15,32,57–67] Many of the developed methods rely on the optical properties of AuNP ensembles. If two AuNPs come in close proximity to each other, the LSPRs can couple which induces a strong red-shift in the absorption spectrum.[68] For this reason aggregation of AuNPs induced by the presence of a specific substance with subsequent color change is a concept widely used in sensing applications.

As another example, the research groups of Mirkin and Letsinger at Northwestern University developed a colorimetric detection system for polynucleotides using AuNP probes.[69,70] The AuNPs are capped with two types of oligonucleotides and can form a complex NP network if a complementary target molecule is present. In these networks, where the AuNPs are in close proximity to each other, the LSPR of the AuNPs is red-shifted, resulting in a color change of the solution from red to purple. The method is highly sensitive, allowing for the distinction of perfect targets from ones with single base mismatches by using the characteristic sharp ``melting transitions´´ of the polymeric networks. In a very similar manner detection of Hg^{2+} ions in aqueous media was realized by Lee at al.[71] A DNA-free method for Hg^{2+} detection was developed by Su et al. using thioctic acid functionalized AuNPs. The detection is highly mercury-specific and works at very low concentrations down to 10 nM, providing a very simple and reliable method for real-time Hg^{2+}-detection.[72]

The optical properties of AuNPs have also been used to increase the efficiency of electronic devices, e.g. organic light-emitting diodes (OLEDs) and solar cells.[67,73–78] Wu and coworkers introduced 20 nm AuNPs into the indium tin oxide (ITO) support of polymer light-emitting diodes and optimized the distance to the overlying light emitting polymer layer. Due to the far-field enhancement effect of the AuNPs, the brightness and luminous efficiency of the device were significantly increased.[74,75]

As detailed above, the position and bandwidth of the LSPR of AuNPs is determined by the complex interplay of the particle size and particle shape as well as the refractive index of the surrounding medium. Further influence comes from the NP core charge and the temperature.[13,41] Especially the influence of temperature will be treated in some detail in the following section concerning the relaxation dynamics of AuNPs.

A great part of this work deals with the isomerization and ultrafast relaxation dynamics of AB derivatives on AuNP surfaces after photoexcitation. Therefore, it is important to understand the basic processes which occur during the relaxation of a photoexcited AuNP system. The following paragraphs give an overview of the AuNP relaxation steps and the ways in which these processes are influenced by internal and external factors.

Gold nanoparticles can be excited directly in the LSPR, in the intraband transitions to the red of the LSPR, or in the interband transitions to the blue of the LSPR. In either case electrons are transferred to unoccupied electronic states above the Fermi level.[79] The events following NP excitation are schematically shown in Figure 1.4.

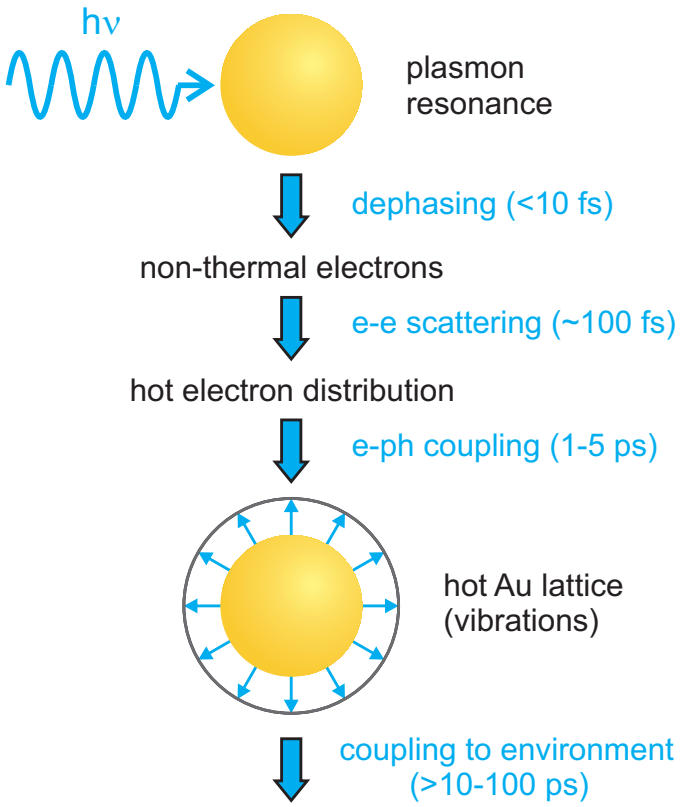

Figure 1.4: Stepwise relaxation of AuNPs after optical excitation.

The coherently excited electrons rapidly dephase within only a few femtoseconds, i.e. still within the duration of the excitation pulse, resulting in a non-equilibrium electron distribution.[41] Electron-electron (e^--e^-) scattering on a timescale of ~ 100 fs subsequently leads to the formation of an equilibrium distribution which can be described with Fermi-Dirac statistics using

$$f = \frac{1}{1 + \exp((E\text{-}E_F)/kT_e)}. \tag{1.4}$$

E_F and E are the Fermi energy and the energy of the electronic energy levels, respectively, k is the Boltzmann constant and T_e is the electronic temperature. As the equilibrium distribution possesses a higher electronic temperature T_e, it is often referred to as ``hot electron distribution''. The hot electrons then transfer their energy into vibrational modes of the Au core or the ligand shell *via* electron-phonon ($e^-$-ph) scattering. The time in which the hot electrons cool down has been termed ``hot electron lifetime'' and is usually on the order of 1-5 ps.[38,39,80,81] The inelastic electron-phonon (e^--ph) scattering heats the metal lattice and possibly also the ligands, which afterwards dissipate their energy into the surrounding medium. This latter process comprises two components: (i) heat transfer across the interface between the particle and the medium surrounding it and (ii) heat diffusion in the surroundings.[82–84] The timescale of coupling to the environment through these two processes depends on the heat capacity of the NP and the surrounding matrix, it is typically in the order of 10-100 ps.[79,85] As will be shown in this Thesis, this relatively long time scale has consequences for AB-functionalized AuNPs because possible *trans-cis* isomerization products find themselves in a ``hot'' environment for periods of 10-100 ps.

All the abovementioned processes depend on the size of the AuNP and the electronic structure of the NP-ligand hybrid system. Even though distinct timescales for each process are given, it needs to be made clear that they do not necessarily occur consecutively and that the timescales can overlap.[79]

Typically, the relaxation dynamics of AuNPs are investigated by femtosecond time-resolved transient absorption spectroscopy. Considering the timescales of the different relaxation processes, mainly e^--ph and ph-ph coupling processes have been investigated,[38,40,84,86,87] but some reports on the e^--e^- scattering process exist as well.[38,88–90] Analogous to the static absorption spectra the shape of the transient spectra depends on the particle shape and size. Following femtosecond excitation, one generally observes a negative absorption at the position of the LSPR and positive bands to both sides of the bleach. Typical transient absorption spectra of spherical AuNPs coated with alkylthiols prepared in this Thesis are shown in Figure 1.5.

After AuNP excitation the LSPR decreases in intensity, as the excited electrons no longer oscillate in phase with the conduction electrons, causing the bleach signal. The positive signals to both sides are due to a broadening of the LSPR compared to the unexcited (ground) state. They arise from the contribution of higher-pole oscillations, e.g. quadrupole oscillations, and possibly also interband transitions and intraband transitions of ``hot'' electrons. Physically, the LSPR broadening can be understood by a faster dephasing time of the coherent plasmon oscillation compared to the ground state.[38,91]

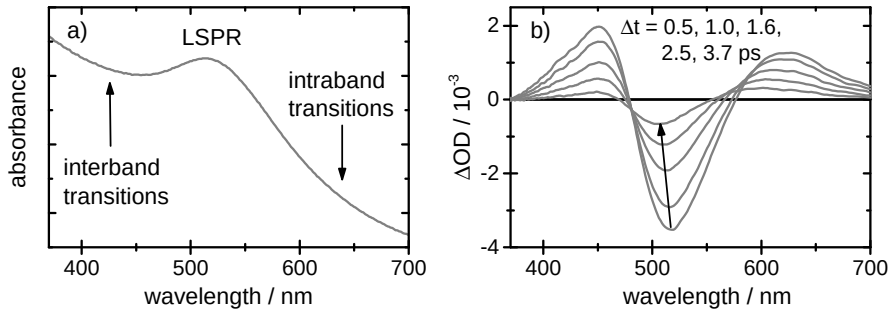

Figure 1.5: (a) Static absorption spectrum of spherical decanethiol-coated AuNPs with $d = 4$ nm. (b) Transient absorption spectra after femtosecond excitation at $\lambda = 350$ nm at different delay times showing a bleach at the position of the LSPR and positive signals to the blue and the red side of the bleach.

The spectral shape of the transient spectra does not change much for AuNPs of different sizes as long as a LSPR band is present.[40,86] However, for Au nanorods, which exhibit a longitudinal and a transversal plasmon oscillation, two bleach signals at the respective LSPR positions are observed.[91] For very small AuNPs ($d = 1.9$ nm) which exhibit no LSPR the transient spectra only show a featureless positive signal below 500 nm which is attributed to interband transitions.[40] Furthermore, in experiments on very small AuNPs ($d < 2$ nm) the excitation of vibrational modes of the Au lattice has been observed. The lattice vibrations lead to a periodical size change of the Au core and induce a LSPR shift which leads to modulations in the transient absorption signal.[92,93]

From the temporal evolution of the transient signals the time scales of the different relaxation processes have been extracted. Electron-electron scattering usually occurs within a few hundred femtoseconds.[40,86,94] The e^--e^- scattering time, $\tau_{e\text{-}e}$, is strongly power-dependent and decreases with increasing power. At higher excitation energies the electrons are excited higher above Fermi level. As $\tau_{e\text{-}e}$ is determined by the number of unoccupied electronic states into which the electron can scatter, it is inversely proportional to the energy an excited electron possesses above Fermi level. Usually $\tau_{e\text{-}e}$ is measured at very low excitation energies, but then the time scales of e^--e^- and e^--ph scattering become similar, making a clear separation difficult.[38] The size dependence of the e^--e^- scattering rate has been demonstrated by Voisin et al.[88,89] With decreasing particle diameter $\tau_{e\text{-}e}$ sharply decreases for NPs smaller than 5 nm, for larger particles only a small size dependence is observed.

The e^--ph scattering process is also strongly power-dependent, but the dependence is opposite to that observed for e^--e^- scattering: The higher the excitation energy is, the higher is the electronic temperature T_e after the initial thermalization, which in turn leads to a longer hot electron lifetime $\tau_{e\text{-}ph}$.[56,79] The hot electron cooling can be de-

scribed with the ``two temperature model'' (2TM) given by a pair of coupled differential equations

$$\gamma T_e \frac{dT_e}{dt} = -g(T_e - T_L) \tag{1.5}$$

$$C_L \frac{dT_L}{dt} = g(T_e - T_L). \tag{1.6}$$

The model relates the change in electronic temperature T_e and lattice temperature T_L to the electronic heat capacity coefficient, γ, the electron-phonon coupling magnitude g and the heat capacity of the lattice, C_L. Under the assumption that the lattice heat capacity is much larger than the electronic heat capacity, i.e. that the lattice temperature remains constant during the cooling process, equations (1.5) and (1.6) lead to an expression for the hot electron lifetime:

$$\tau_{e\text{-}ph} = \frac{\gamma(T_0 + \Delta T_e^{max})}{g} = \frac{\gamma T_0}{g} + \frac{\gamma \Delta T_e^{max}}{g}. \tag{1.7}$$

Therein, T_0 is the temperature of the system before excitation and ΔT_e^{max} is the initial electron temperature after electron thermalization. Equation (1.7) suggests a first-order kinetic decay of the hot electron temperature, in which $\tau_{e\text{-}ph}$ increases with increasing initial temperature ΔT_e^{max}, thus it is excitation power-dependent. A power-independent lifetime can be determined by measuring $\tau_{e\text{-}ph}$ at a series of excitation powers and then extrapolating the lifetime to zero power.[56,95]

A size dependence of $\tau_{e\text{-}ph}$ has been observed in the low-perturbation regime by the research group of Vallée.[96] They investigated Au- and AgNPs with diameters between 2.2 and 30 nm and found a steep decrease of $\tau_{e\text{-}ph}$ for particles smaller than ~ 5 nm. However, in the strong-perturbation regime no size dependence in AuNPs ranging from 1 to 25 nm in size was observed by El-Sayed and coworkers.[38,40,97] As the crystallinity of the AuNP lattice also possesses an influence on the e^--ph coupling magnitude by introducing additional vibrational modes, twinning defects in larger AuNPs could obscure signs of a size dependence.[98]

An influence of the environment, i.e. the surrounding matrix and the ligand shell, on $\tau_{e\text{-}ph}$ has frequently been reported.[18,56,79,90,99,100] The direct comparison of cooling times in different environments is complicated by the complexity of the interactions, as changes in the surface chemistry or the crystallinity induced by the matrix exchange will also influence $\tau_{e\text{-}ph}$.[85] There is a connection between the heat capacity of the matrix and the hot electron lifetime predicted by the 2TM, but the influence is only indirect, as a larger heat capacity facilitates dissipation of heat into the surroundings.[56]

Changes in the surface chemistry have a more direct influence on $\tau_{e\text{-}ph}$. Ligands modulate the hot electron cooling dynamics through

the electronic heat capacity C_e.[79,85] The electronic heat capacity depends upon the electronic density of states, $\rho(E)$, through

$$C_e(T_e) = \int_{-\infty}^{\infty} \frac{\mathrm{d}f(E, \mu, T_e)}{\mathrm{d}T_e} \rho(E) E \, \mathrm{d}E, \tag{1.8}$$

where f is the Fermi-Dirac distribution as a function of energy E, chemical potential μ, and electronic temperature T_e. Due to mixing of lattice and ligand states, the density of states is altered significantly upon ligand attachment, especially thiols have been reported to exert a strong influence.[56] The electronic heat capacity determines not only the initial electronic temperature after the absorption of a photon, but also the instantaneous electron cooling rate, giving the ligands a direct influence on $\tau_{\text{e-ph}}$. A larger electronic heat capacity translates into a smaller initial electronic temperature after excitation, and therefore a slow-down of the cooling dynamics.[56]

Ligands furthermore influence the rate of energy transfer between electrons and Au lattice, and thereby also $\tau_{\text{e-ph}}$, by changing the electron-phonon coupling magnitude, g. Electron-phonon coupling is influenced by the electronic density of states (as is the electronic heat capacity) and also the number and energetical distribution of available vibrational modes.[85] Organic ligands not only change the electronic density of states, but also introduce new vibrational modes into the system. A higher number of vibrational modes leads to an acceleration of electron cooling dynamics.[56]

The electronic heat capacity coefficient γ and the electron-phonon coupling magnitude g can be determined with the 2TM.[79,85] In order to do so, several issues have to be adressed: (i) The abovementioned overlap of timescales for the different relaxation processes can be circumvented by only analyzing times at which the electronic temperature is much higher than the lattice temperature. (ii) The relationship between T_e and the bleach intensity ΔA at the LSPR position is not necessarily linear as the increase of electronic temperature depends on the AuNP size and the surface chemistry. Description of the transient absorption spectra using a temperature-dependent dielectric function, $\epsilon(\omega, T_e)$, will allow for an accurate determination of T_e. (iii) The number of absorbed photons depends on the absorption coefficient of the AuNPs which changes with size, shape and surface chemistry.

A large number of works concerning the deactivation mechanism of AuNPs and the influence of the environment on the dynamics have been published in the last 25 years.[18,38,40,41,84,86–91,94,96–98,100–104] Several publications regarding the attachment and/or exchange of ligands, e.g. amines, anilines, citrate, sulfonates and thiols, report changes in the hot electron cooling dynamics.[18,56,87,100,103,105] Westcott et al. adsorbed *p*-aminobenzoic acid, aniline, *p*-mercaptobenzoic

acid and *n*-propylamine onto nanoparticles consisting of a gold sulfide core and a gold shell of 3 to 5 nm thickness and studied the e^--ph scattering process with ultrafast spectroscopy. Upon adsorption of *p*-aminobenzoic acid and aniline they found a significant shortening of $\tau_{e\text{-}ph}$, whereas the effect was much less pronounced for *p*-mercaptobenzoic acid and *n*-propylamine. Quantum chemical calculations of the dipole moment induced upon ligand adsorption showed that the perturbation responsible for changes in $\tau_{e\text{-}ph}$ is electronic in nature.[18] A more detailed investigation of the parameters through which surface chemistry determines the hot electron lifetimes was presented by Aruda et al.[56] Comparison of the hot electron cooling dynamics of aminated and thiolated AuNPs showed a longer $\tau_{e\text{-}ph}$ in thiolated AuNPs. The effect could be traced back to a larger electronic heat capacity and a larger e^--ph coupling magnitude compared to aminated AuNPs. In this important study, all the abovementioned issues regarding the use of the 2TM have been addressed. Especially the relationship between the electronic temperature and the differential absorption in the LSPR region has been clarified by using a Mie theory model based on a temperature-dependent dielectric function. This model will also prove essential for the present Thesis on AB-functionalized AuNPs.

The large number of variables that influence the electron cooling dynamics makes a systematic investigation difficult and is responsible for the fact that the picture is still ambiguous after more than two decades of intense research in the area.

1.2 MOLECULAR SWITCHES ON GOLD NANOPARTICLES

Molecular switches

Materials with light-tunable properties incorporating photochromic molecular switches are interesting in many applications in fundamental and technical sciences. Examples for the use of photochromic molecules include liquid crystal displays,[106,107] organic light emitting diodes (OLEDs),[108–111] optical data storage,[108,112–115] biological, medical and diagnostic applications,[116–120] and light-driven molecular machines.[121–125]

Photochromic molecular switches[121] can be reversibly interconverted by light at different wavelengths between two isomeric states with distinct optical, chemical, magnetic and electronic properties. Generally, the isomerization induces changes in the structure, the dipole moment, the conductivity or the magnetic state of the molecule. Ideally, a photoswitch possesses low photochemical fatigue, high photochemical conversion rates, large isomerization quantum yields for the interconversion between its two states, and high thermal stability of both isomers. A combination of the exceptional photochemical properties of molecular switches with the unique optical properties of

AuNPs promises the discovery of new methods for the construction of photoresponsive materials.

The most well known classes of photoswitchable molecules include azobenzenes,[126,127] fulgides,[128,129] diarylethenes,[127,130] and spiropyrans,[131,132] among which azobenzenes (ABs) are the most commonly used compounds due to their simple preparation, low photochemical fatigue, and high photostability.

The thermodynamically more stable *trans* form of AB can be converted to the *cis* form with UV light, *cis-trans* back-isomerization is achieved with visible light or thermally. The chemical structures of both isomers are shown in Figure 1.6. Photoisomerization of AB leads to a drastic change in the molecular properties: The planar *trans* form is $\approx$ 9 Å long while the more compact *cis* form is only $\approx$ 6 Å long and non-planar. Along with the geometry the dipole moment of AB changes from $\mu = 0$ D in the *trans* form to $\mu \approx 3$ D in the *cis* form.[133,134]

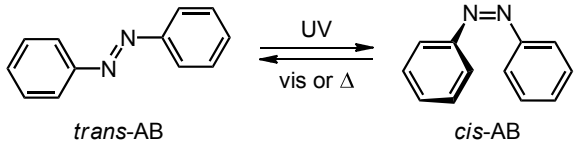

Figure 1.6: Photochemical interconversion of *trans*- and *cis*-AB.

The absorption spectra of both isomers shown in Figure 1.7 exhibit two transitions, the weak $n\pi^*$ transition ($S_0 \rightarrow S_1$) in the visible and the strong $\pi\pi^*$ transition ($S_0 \rightarrow S_2$) in the UV. The S_2 transition peaks at $\lambda \approx 320$ nm, possesses a large oscillator strength and dominates the spectrum of *trans*-AB. In the spectrum of *cis*-AB it is much weaker and appears at $\lambda = 275$ nm. The S_1 transition appears at $\lambda = 440$ nm in both isomers and is very weak as it is symmetry-forbidden. Due to the reduced symmetry of *cis*-AB the S_1 band is more intense than in the *trans* form.[134]

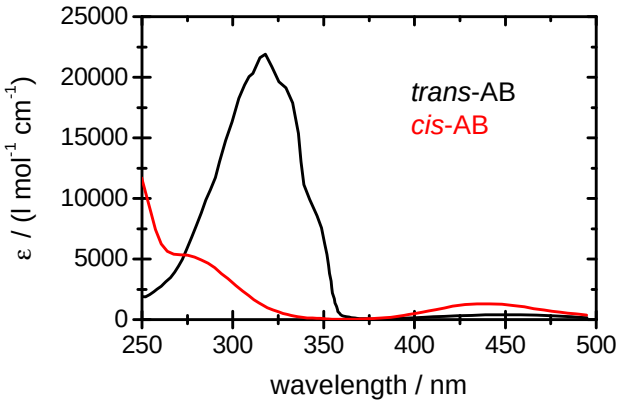

Figure 1.7: Absorption spectra of *trans*- and *cis*-AB in *n*-hexane.[135]

Substitution of the AB molecule strongly influences the $\pi\pi^*$ band position, whereas the $n\pi^*$ band is usually affected little. In special cases as for example *push-pull* substituted ABs, the $\pi\pi^*$ band possesses a strong charge-transfer (CT) character and is red-shifted by up to $\Delta\lambda \approx 100$ nm.[136,137] The drastic changes in the electronic structure by the substitution also affect the thermal lifetime of the *cis* isomer, which is shortened from a few hours in unsubstituted AB to milliseconds in *push-pull* ABs like Disperse Red 1 (DR-1).[136,138,139]

The ultrafast dynamics of the isomerization of unsubstituted AB have been investigated thoroughly and are known to occur on the femtosecond and picosecond time scale.[140–143] Satzger and coworkers performed femtosecond time-resolved transient absorption measurements on AB after $n\pi^*$ and $\pi\pi^*$ excitation, respectively, and determined the excited lifetimes and relaxation pathways.[141,142] After $n\pi^*$ excitation of *trans*-AB, the molecule is found in the Franck-Condon region of the S_1 state from which it departs with a time constant of $\approx$ 300 fs. *Via* the S_0/S_1 conical intersection the ground state (S_0) of the *trans* and / or the *cis* isomer is populated in $\approx$ 3 ps. The relaxation pathway after $\pi\pi^*$ excitation into the S_2 state is slightly different: The wavepacket rapidly leaves the Franck-Condon region of the S_2 state and relaxes to the energetically lower S_1 state *via* a conical intersection within $\approx$ 100 fs. Afterwards, isomerization and radiationless deactivation to the S_0 state take place with time constants of $\approx$ 500 fs and $\approx$ 3 ps. The dynamics of the *cis-trans* isomerization process are very similar.[141–143] The time scales found by Satzger et al. agree well with reports by other groups, only small deviations of the decay times are observed.[143–145] A detailed summary of the ultrafast dynamics of *trans*- and *cis*-AB after $n\pi^*$ and $\pi\pi^*$ excitation based on experimental and computational results can be found in a joint paper by Ernsting and coworkers.[140]

Substitution of AB can have severe influence on the relaxation dynamics. In *push-pull* substituted ABs such as DR-1 the energetic ordering of the electronic states and therefore the relaxation pathway is changed compared to plain AB.[136,137,146,147] Bahrenburg et al. investigated the ultrafast dynamics of DR-1 after $\pi\pi^*$ excitation in solution in 2-fluorotoluene and found an ultrafast relaxation to the $n\pi^*$ state in less than 100 fs followed by isomerization within 1 ps and vibrational ground state cooling within 6 ps.[137] The dynamics after S_2 excitation of amino or methoxy AB is rather similar to plain AB.[148,149]

Restrictive environments exhibiting mechanical forces onto AB can greatly enhance the excited state lifetimes as demonstrated in a study by Bahrenburg et al. on DR-1 and 4,4′-bis(acetamido)-azobenzene covalently attached to polybutylmethacrylate polymer colloids.[150] Due to strong mechanical forces in the complex micronetworks, the excited state lifetime of photoswitches covalently bound to the polymer side chain was enhanced 10-fold compared to DR-1 in solution.

For AB inserted into the polymer main chain the excited state lifetime was increased more than 20-fold.

Azobenzene on gold nanoparticles

The selected examples presented above demonstrate the strong impact complex environments and electronic effects have on the AB relaxation pathway. Anchoring photochromic ABs to metal NPs accordingly can have significant influence on their isomerization properties, i.e. the quantum yield, the conversion efficiency, or the excited state lifetime. For example, ABs directly adsorbed onto metallic surfaces suffer from a loss of photoreactivity due to steric hindrance, surface-specific changes of the electronic structure, and energy transfer between chromophore and metal.[151–155] A recovery of the photoresponsive behaviour can be achieved by introducing spatial distance between chromophore and substrate. The necessary distance can be created through functionalization of the AB with bulky *tert*-butyl groups which act as ``legs´´ that lift the molecule from the surface and reduce substrate-induced quenching.[151,152] However, the most widely used and most flexible concept to spatially and electronically separate chromophore and substrate is the adsorption of ligands with long alkyl chain linkers into ordered self-assembled monolayers (SAMs). SAMs of alkylthiols on gold surfaces show a highly ordered structure in which the alkyl chains are extended in an all-*trans* conformation. The molecules point away from the gold surface at a certain angle which depends on the chain length so that precise adjustment of the distance between head group and substrate is possible.[156]

SAMs of ω-azobenzene-alkylthiols on Au surfaces have often been shown to possess photoswitching abilities,[19–23,157–161] although steric and electronic effects still can limit the switching propensities of AB significantly. In densely packed monolayers on flat gold substrates steric constraints are known to significantly hinder the AB isomerization which is associated with a large-amplitude motion.[20,162] Moreover, excitonic coupling between neighbouring chromophores in the monolayer changes the optical properties of AB and decreases the isomerization yields.[22,163] Usually these hindrances are eliminated by diluting the AB ligands with simple alkylthiol coligands[22,23,158] or through the use of sterically demanding AB ligands like platform based chromophores[164] or multivalent linkers.[165,166] Both strategies successfully increase the distance between individual chromophores and reduce the unwanted side effects.

The surface curvature of AuNPs inherently creates more free space around the head groups of the ligands, and thus facilitates isomerization even at higher AB surface coverages.[157] Figure 1.8 schematically shows the dilution of SAMs on Au surfaces.

The dependence of substrate-induced quenching on the chromophore-NP distance was demonstrated by Whitesell and coworkers

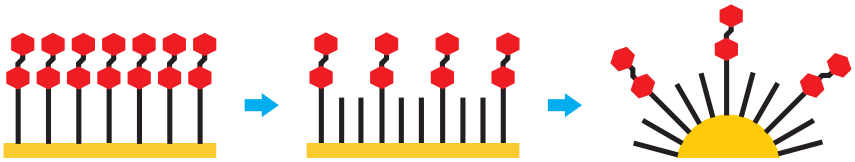

Figure 1.8: Dilution of SAMs through coadsorption of coligands and the effect of the surface curvature of AuNPs.

who investigated the isomerization of AB on 2.5 nm AuNPs as function of the alkyl linker chain length.[21] In their study, the isomerization quantum yield was reduced ~ 100 fold when the distance between AB moiety and AuNP was decreased from ~ 1.25 nm to ~ 0.5 nm. Irie and coworkers observed the reduction of photo-induced cyclization efficiencies of diarylethenes upon attachment to gold and silver nanoparticles (AgNPs).[159,160] In both cases the effect was attributed to quenching of the excited state by the LSPR of the metallic NP. In the latter study the effect was enhanced as the particle size and therewith the LSPR absorption was increased which confirms that the interaction between ligand and substrate is responsible for the reduced photoresponsivity. AuNPs are also known to quench the fluorescence of organic molecules at their surface through Förster resonance energy transfer (FRET) or photoinduced electron-transfer.[17,167–171] Dulkeith et al. found that attachment to AuNPs quenches the fluorescence of lissamine dye molecules with an efficiency of 99.8 %. Time-resolved fluorescence spectroscopy revealed an increase in the fluorescence lifetime with decreasing particle diameter which indicates a reduced energy transfer efficiency in smaller AuNPs.[168]

Just like gold nanoparticles influence the properties of molecules in their proximity, the AuNP properties are modulated by adsorbates on their surface. The optical properties of AuNPs can be altered by photochromic molecules in two different ways: (i) Isomerization of the switch changes the dielectric constant of the AuNP environment which induces shifts in the highly sensitive LSPR absorption. (ii) Molecular switches can control the distances between individual AuNPs and thus induce changes in the AuNP absorption. The latter strategy usually leads to more pronounced changes in the optical properties by aggregation of the NPs and many examples can be found in the literature.[23,161,172–176] For example, Klajn et al. used AB-functionalized AuNPs embedded in a polymeric matrix to construct a re-writable photoresponsive ``paper´´. The initially completely dispersed AuNPs colored the paper red and upon UV irradiation it turned purple and finally blue. The images or words written onto the paper could be erased using visible light or heat.[174] Another elegant example for the application potential of ligand-induced AuNP aggregation are dual-responsive nanoparticles that aggregate under the simultaneous action of light and CO_2.[176] The particles are functionalized with a

mixed SAM (mSAM) of AB and a diamine ligand that can bind CO_2. The AuNPs reversibly aggregate only when both light and CO_2 are present which makes the system a dual stimuli-responsive AND logic gate. The aggregation potential of AB-functionalized AuNPs is determined by a number of factors such as the polarity of the solvent/matrix, and the AB surface coverage,[16,173–175] and, if mSAMs are used, also the nature of the coligand.[175,176] In some cases it is even possible to control the size and the structure of the AuNP aggregates.[173]

Recently, Zep et al. used 2.5 nm sized AuNPs functionalized with a self-assembled monolayer of alkylthiols and AB-thiols for the construction of phototunable liquid-crystalline (LC) phases.[177] In the initial *trans* state the AuNPs formed lamellar LC phases which could be melted into an isotropic liquid under the influence of UV light. As soon as the UV light was removed the initial LC phase was restored, indicating a strongly accelerated thermal *cis-trans* back-isomerization of the AB compared to the free AB ligand where the *cis* isomer is stable for days. Interestingly, in LCs with a lower AB surface concentration UV irradiation leads to a decrease of the layer distance in the LC phase but not to melting. Larger silver nanoparticles coated with the same AB molecules do not form LC phases at all. The AB-functionalized AuNPs in this example do not only hold great promise for the construction of materials with light-controllable plasmonic properties, they also illustrate the delicate relationship between structure and functionality of such organic-inorganic hybrid systems.

The investigation of the relaxation pathways of photochromic molecules attached to AuNPs and of the AuNPs themselves could shed light on the complicated electronic structure of these hybrid systems. Owing to the complex nature of the investigations, only a few reports on the ultrafast dynamics of adsorbates on AuNPs exist to date. Most of them deal with organic dyes, e.g. rhodamine 6G and coumarin, and investigate the influence of the AuNP on the adsorbates emission.[178–181] In particular, Ghosh et al. investigated the ultrafast dynamics of a fluorescent coumarin derivative possessing two intramolecular charge transfer (ICT) states. In solution the locally excited ICT state relaxes to the second longer-lived ICT state that is formed through a twist of an amino group in the molecule. When the molecule is adsorbed onto AuNPs the emission of the twisted ICT completely vanishes due to restricted molecular twisting on the AuNP surface.[180,181] Little is known from direct experimental studies to date, however, about the ultrafast isomerization dynamics of ABs on AuNPs.

1.3 MOTIVATION AND AIM OF THIS THESIS

The relationship between the chemical and electronic structure of the ligand-AuNP hybrid system and its relaxation dynamics has been the

subject of intense research for almost 20 years. Even though many reports exist on AuNPs functionalized with photochromic molecules, direct information on the ultrafast dynamics of the photoisomerization process on AuNP surfaces is not available to the best of the author's knowledge. A number of questions about the electronic structure of the chromophore-AuNP hybrid system and the influence of energy transfer processes and resonant coupling on the isomerization process have to be answered. The stepwise relaxation dynamics of the AuNP core have frequently been investigated with regard to its mechanism and the influence of the ligand shell on the relaxation time scales. However, these studies were limited to the influence of the ligands anchoring groups and did not consider different functional head groups. Therefore, no information on the cooling dynamics of chromophore-functionalized AuNPs exists either. The work presented in this Thesis intends to shed some light on these fundamental issues.

The first goal of this Thesis was the investigation of the ultrafast dynamics of AB on AuNPs to determine the factors that influence the isomerization process. Figure 1.9 shows the thiolated AB derivatives and the alkanethiols which were brought onto the surface of 4 nm sized AuNPs in mixed self-assembled monolayers (mSAMs).

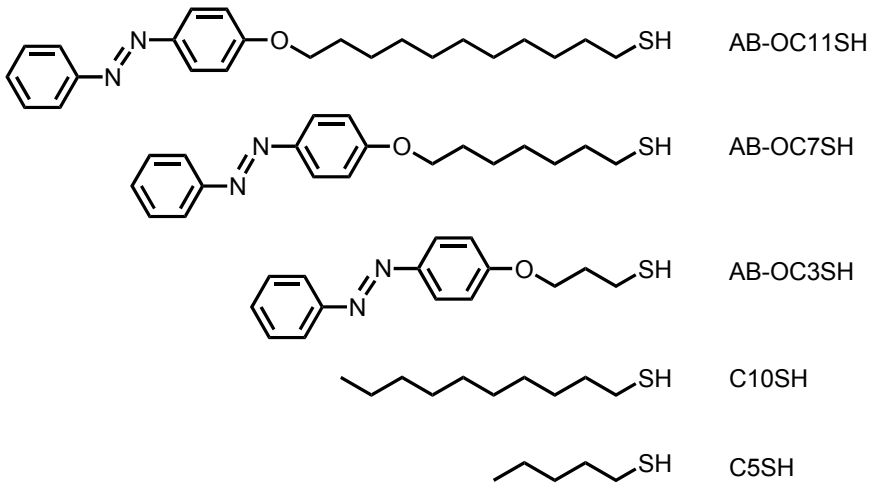

Figure 1.9: Structures of the AB ligands with different linker chain lengths and the two coligands, decanethiol and pentanethiol.

A schematic picture of the mSAM of azobenzenethiols and alkylthiols on the AuNPs is shown in Figure 1.10.

In order to examine possible energy transfer between AB and AuNP, which would influence the isomerization efficiency, three different linker chain lengths were used to adjust the chromophore-AuNP distance between 0.5 and 1.5 nm. The switching efficiencies of the AB functionalized AuNPs were investigated with static absorption spectroscopy after irradiation with UV and visible light to induce pho-

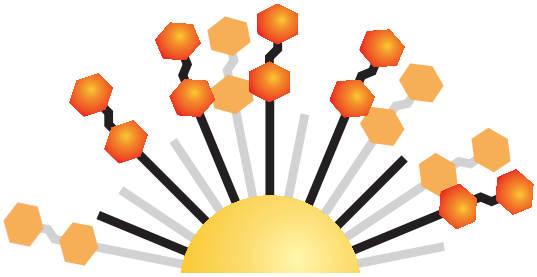

Figure 1.10: A mSAM of azobenzenethiols and alkylthiols on a AuNP.

toisomerization. The results of this study are presented in Chapter 3. High *trans-cis* and *cis-trans* conversion efficiencies are found for all three chain lengths, revealing that there is little significant energy transfer between the AuNP core and the chromophore in the investigated systems. Furthermore, a light-induced reversible AuNP aggregation is observed in systems where the chain length of the coligand is significantly shorter than the AB linker chain length, i.e. AB-OC11SH and AB-OC7SH combined with C5SH.

Subsequently, the ultrafast dynamics of AB-functionalized AuNPs were investigated by femtosecond time-resolved transient absorption spectroscopy. As aggregates were deposited on the flow cell windows during the measurement of aggregating AuNP samples, only AuNPs functionalized with AB-OC11SH and decanethiol (50:50) were examined. The results of this study are presented in Chapter 4. The ultrafast dynamics of AB show surprisingly little difference compared to the dynamics of free AB-OC11SH in solution. The relaxation dynamics of the AuNP core itself show no significant difference to the dynamics of AuNPs functionalized purely with decanethiol, indicating that the AB moiety and the AuNP core are efficiently decoupled by the long alkyl linker chain.

Based on the results of this study, the ultrafast dynamics of the *push-pull* AB derivative Disperse Red 1 (DR-1) attached to 4 nm sized AuNPs were investigated. DR-1 was chosen as a ligand because its ultrafast dynamics in solution are well understood and it exhibits large transient absorption signals which should facilitate the separation of ligand and AuNP signals. In this study, the AuNPs were functionalized with a mSAM of the thiol-functionalized DR-1 shown in Figure 1.11 and decanethiol.

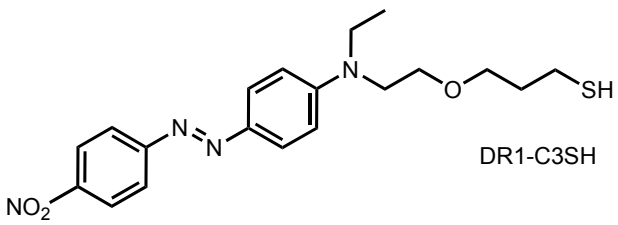

Figure 1.11: Chemical structure of thiol-functionalized DR-1.

The time-resolved data for DR1-functionalized AuNPs and their comparison to results for purely decanethiol-functionalized AuNPs and free DR-1 in solution are presented in Chapter 5. In this data, no permanent product formation of DR-1 is observed and the obtained transient signal intensities differ significantly. The results hint at the presence of electronic interaction, possibly a metal-to-ligand charge transfer, due to resonant coupling between the LSPR of the AuNP and the $\pi\pi^*$ absorption of DR-1. Further investigations will be necessary to comprehensively explain the effects observed in this study.

To examine the influence of ligands on the AuNP relaxation dynamics in some more detail, particles capped with different aromatic ligands were investigated by transient absorption spectroscopy. In this study the AuNPs were functionalized with mSAMs of decanethiol and the ligands shown in Figure 1.12 as well as the DR-1 derivative shown in Figure 1.11.

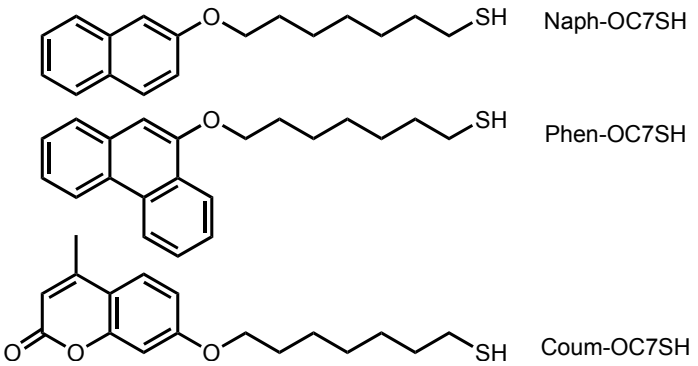

Figure 1.12: Aromatic ligands used to functionalize the AuNPs in order to investigate the influence of ligand heat capacity and resonant coupling between LSPR and ligand absorption bands on the AuNP relaxation dynamics.

The naphthol- and phenanthrol-derivatives were used to determine the effect of ligands with different heat capacities on the hot electron cooling dynamics. With the AuNPs coated with the coumarin- and DR1-derivatives the extent of resonant coupling between close-lying LSPR and ligand absorption bands was investigated. The data of the time-resolved measurements were compared to data of purely decanethiol-coated AuNPs. The results of this study are presented in Chapter 6. In the data of the DR1-functionalized AuNPs indications for coupling between chromophore and AuNP were found. However, neither the ligand heat capacity nor the presence of ligand-related absorption bands close to the LSPR had an observable effect on the AuNP relaxation dynamics as long as the pump light only excited the AuNP. The same hot electron lifetimes were found in all samples.

Before the presentation of the results, Chapter 2 will give the experimental details and the methods for data analysis. At the end of this Thesis, Chapter 7 gives a summary of all results and an outlook.

BIBLIOGRAPHY

[1] Waser, R., Ed. *Nanoelectronics and Information Technology - Advanced Electronic Materials and Novel Devices*; Wiley-VCH, Weinheim, 2003.

[2] Prince, B. *Semiconductor Memories*, 2nd ed.; Wiley-Teubner, Stuttgart, 1991.

[3] Lee, J.-S.; Cho, J.; Lee, C.; Kim, I.; Park, J.; Kim, Y.-M.; Shin, H.; Lee, J.; Caruso, F. *Nat. Nanotechnology* **2007**, *2*, 790–795.

[4] Wei, Q.; Lin, Y.; Anderson, E. R.; Briseno, A. L.; Gido, S. P.; Watkins, J. J. *ACS Nano* **2012**, *6*, 1188–1194.

[5] Kang, M.; Baeg, K.-J.; Khim, D.; Noh, Y.-Y.; Kim, D.-Y. *Adv. Funct. Mater.* **2013**, *23*, 3503–3512.

[6] Bozano, L. D.; Kean, B. W.; Beinhoff, M.; Carter, K. R.; Rice, P. M.; Scott, J. C. *Adv. Funct. Mater.* **2005**, *15*, 1933–1939.

[7] Zhou, Y.; Han, S.-T.; Xu, Z.-X.; Roy, V. A. L. *Adv. Mater.* **2012**, *24*, 1247–1251.

[8] Tseng, C.-W.; Huang, D.-C.; Tao, Y.-T. *ACS Appl. Mater. Interfaces* **2013**, *5*, 9528–9536.

[9] Raimondo, C.; Crivillers, N.; Reinders, F.; Sander, F.; Mayor, M.; Samorì, P. *Proc. Nat. Acad. Sci. U.S.A.* **2012**, *109*, 12375–12380.

[10] Daniel, M.-C.; Astruc, D. *Chem. Rev.* **2004**, *104*, 293–346.

[11] Kreibig, U.; Vollmer, M. *Optical Properties of Metal Clusters*; Springer-Verlag Berlin Heidelberg, 1995.

[12] Kreibig, U.; Gartz, M.; Hilger, A. *Ber. Bunsen-Ges. Phys. Chem.* **1997**, *101*, 1593–1604.

[13] Templeton , A. C.; Pietron, J. J.; Murray, R. W.; Mulvaney, P. *J. Phys. Chem. B* **2000**, *104*, 564–570.

[14] Mayer, K. M.; Hafner, J. H. *Chem. Rev.* **2011**, *111*, 3828–3857.

[15] Giljohann, D. A.; Seferos, D. S.; Daniel, W. L.; Massich, M. D.; Patel, P. C.; Mirkin, C. A. *Angew. Chem. Int. Ed.* **2010**, *49*, 3280–3294.

[16] Klajn, R.; Stoddart, J. F.; Grzybowski, B. A. *Chem. Soc. Rev.* **2010**, *39*, 2203–2237.

[17] Thomas, K. G.; Kamat, P. V. *Acc. Chem. Res.* **2003**, *36*, 888–898.

[18] Westcott, S. L.; Averitt, R. D.; Wolfgang, J. A.; Nordlander, P.; Halas, N. J. *J. Phys. Chem. B* **2001**, *105*, 9913–9917.

[19] Shin, K.; Shin, E. J. *Bull. Korean Chem. Soc.* **2008**, *29*.

[20] Evans, S. D.; Johnson, S. R.; Ringsdorf, H.; Williams, L. M.; Wolf, H. *Langmuir* **1998**, *14*, 6436–6440.

[21] Zhang, J.; Whitesell, J. K.; Fox, M. A. *Chem. Mater.* **2001**, *13*, 2323–2331.

[22] Moldt, T.; Brete, D.; Przyrembel, D.; Das, S.; Goldman, J. R.; Kundu, P. K.; Gahl, C.; Klajn, R.; Weinelt, M. *Langmuir* **2015**, *31*, 1048–1057.

[23] Manna, A.; Chen, P.-L.; Akiyama, H.; Wei, T.-X.; Tamada, K.; Knoll, W. *Chem. Mater.* **2003**, *15*, 20–28.

[24] Mehlich, J. Stained glass Standesscheibe of Unterwalden (1564), now in Sułkowski castle in Bielsko-Biała (Poland). www.wikipedia.org/wiki/Stained_glass, Reproduced under the Creative Commons Attribution-Share Alike 3.0 Unported license. Accessed September, 2nd, 2015.

[25] Sciau, P. In *The Delivery of Nanoparticles*; Hashim, A. A., Ed.; InTech, 2012; Chapter 25, *Nanoparticles in Ancient Materials: The Metallic Lustre Decorations of Medieval Ceramics*.

[26] Faraday, M. *Phil. Trans. R. Soc. Lond.* **1857**, *147*, 145–181.

[27] Mie, G. *Ann. Phys.* **1908**, *330*, 377–445.

[28] Brust, M.; Walker, M.; Bethell, D.; Schiffrin, D. J.; Whyman, R. *J. Chem. Soc., Chem. Commun.* **1994**, 801–802.

[29] Brust, M.; Kiely, C. J. *Colloids Surf. A: Physicochem. Eng. Asp.* **2002**, *202*, 175–186.

[30] Grzelczak, M.; Perez-Juste, J.; Mulvaney, P.; Liz-Marzan, L. M. *Chem. Soc. Rev.* **2008**, *37*, 1783–1791.

[31] Sardar, R.; Funston, A. M.; Mulvaney, P.; Murray, R. W. *Langmuir* **2009**, *25*, 13840–13851.

[32] Saha, K.; Agasti, S. S.; Kim, C.; Li, X.; Rotello, V. M. *Chem. Rev.* **2012**, *112*, 2739–2779.

[33] Zhao, P.; Li, N.; Astruc, D. *Coordin. Chem. Rev.* **2013**, *257*, 638–665.

[34] Li, N.; Zhao, P.; Astruc, D. *Angew. Chem. Int. Ed.* **2014**, *53*, 1756–1789.

[35] Jain, P. K.; Lee, K. S.; El-Sayed, I. H.; El-Sayed, M. A. *J. Phys. Chem. B* **2006**, *110*, 7238–7248.

[36] Rance, G. A.; Marsh, D. H.; Khlobystov, A. N. *Chem. Phys. Lett.* **2008**, *460*, 230–236.

[37] Liu, X.; Atwater, M.; Wang, J.; Huo, Q. *Colloids Surf., B* **2007**, *58*, 3–7.

[38] Link, S.; El-Sayed, M. A. *J. Phys. Chem. B* **1999**, *103*, 8410–8426.

[39] Link, S.; El-Sayed, M. A. *Int. Rev. Phys. Chem.* **2000**, *19*, 409–453.

[40] Logunov, S. L.; Ahmadi, T. S.; El-Sayed, M. A.; Khoury, J. T.; Whetten, R. L. *J. Phys. Chem. B* **1997**, *101*, 3713–3719.

[41] Link, S.; El-Sayed, M. A. *J. Phys. Chem. B* **1999**, *103*, 4212–4217.

[42] Schaaff, T. G.; Shafigullin, M. N.; Khoury, J. T.; Vezmar, I.; Whetten, R. L.; Cullen, W. G.; First, P. N.; Gutiérrez-Wing, C.; Ascensio, J.; Jose-Yacamán , M. J. *J. Phys. Chem. B* **1997**, *101*, 7885–7891.

[43] Gans, R. *Ann. Phys.* **1912**, *342*, 881–900.

[44] Zhao, J.; Pinchuk, A. O.; McMahon, J. M.; Li, S.; Ausman, L. K.; Atkinson, A. L.; Schatz, G. C. *Acc. Chem. Res.* **2008**, *41*, 1710–1720.

[45] Henglein, A. *J. Phys. Chem.* **1993**, *97*, 5457–5471.

[46] Persson, B. *Surf. Sci.* **1993**, *281*, 153–162.

[47] Hövel, H.; Fritz, S.; Hilger, A.; Kreibig, U.; Vollmer, M. *Phys. Rev. B* **1993**, *48*, 18178–18188.

[48] Linnert, T.; Mulvaney, P.; Henglein, A. *J. Phys. Chem.* **1993**, *97*, 679–682.

[49] Mulvaney, P. *Langmuir* **1996**, *12*, 788–800.

[50] Malinsky, M. D.; Kelly, K. L.; Schatz, G. C.; Duyne, R. P. V. *J. Am. Chem. Soc.* **2001**, *123*, 1471–1482.

[51] Thomas, K. G.; Zajicek, J.; Kamat, P. V. *Langmuir* **2002**, *18*, 3722–3727.

[52] Ghosh, S. K.; Nath, S.; Kundu, S.; Esumi, K.; Pal, T. *J. Phys. Chem. B* **2004**, *108*, 13963–13971.

[53] Cheng, C.-S.; Chen, Y.-Q.; Lu, C.-J. *Talanta* **2007**, *73*, 358–365.

[54] Chen, K.-J.; Lu, C.-J. *Talanta* **2010**, *81*, 1670–1675.

[55] Peng, S.; McMahon, J. M.; Schatz, G. C.; Gray, S. K.; Sun, Y. *Proc. Nat. Acad. Sci. U.S.A.* **2010**, *107*, 14530–14534.

[56] Aruda, K. O.; Tagliazucchi, M.; Sweeney, C. M.; Hannah, D. C.; Schatz, G. C.; Weiss, E. A. *Proc. Nat. Acad. Sci. U.S.A.* **2013**, *110*, 4212–4217.

[57] Eustis, S.; El-Sayed, M. A. *Chem. Soc. Rev.* **2006**, *35*, 209–217.

[58] Alex, S.; Tiwari, A. *J. Nanosci. Nanotechnol.* **2015**, *15*, 1869–1894.

[59] Yeh, Y.-C.; Creran, B.; Rotello, V. M. *Nanoscale* **2012**, *4*, 1871–1880.

[60] Zeng, S.; Yong, K.-T.; Roy, I.; Dinh, X.-Q.; Yu, X.; Luan, F. *Plasmonics* **2011**, *6*, 491–506.

[61] Bedford, E. E.; Spadavecchia, J.; Pradier, C.-M.; Gu, F. X. *Macromol. Biosci.* **2012**, *12*, 724–739.

[62] Boisselier, E.; Astruc, D. *Chem. Soc. Rev.* **2009**, *38*, 1759–1782.

[63] Wilson, R. *Chem. Soc. Rev.* **2008**, *37*, 2028–2045.

[64] Anker, J. N.; Hall, W. P.; Lyandres, O.; Shah, N. C.; Zhao, J.; van Duyne, R. P. *Nat. Mater.* **2008**, *7*, 442–453.

[65] Rosi, N. L.; Giljohann, D. A.; Thaxton, C. S.; Lytton-Jean, A. K. R.; Han, M. S.; Mirkin, C. A. *Science* **2006**, *312*, 1027–1030.

[66] Nie, L.; Liu, F.; Ma, P.; Xiao, X. *J. Biomed. Nanotechnol.* **2014**, *10*, 2700–2721.

[67] Hutter, E.; Fendler, J. *Adv. Mater.* **2004**, *16*, 1685–1706.

[68] Ghosh, S. K.; Pal, T. *Chem. Rev.* **2007**, *107*, 4797–4862.

[69] Elghanian, R.; Storhoff, J. J.; Mucic, R. C.; Letsinger, R. L.; Mirkin, C. A. *Science* **1997**, *277*, 1078–1081.

[70] Storhoff, J. J.; Elghanian, R.; Mucic, R. C.; Mirkin, C. A.; Letsinger, R. L. *J. Am. Chem. Soc.* **1998**, *120*, 1959–1964.

[71] Lee, J.-S.; Han, M. S.; Mirkin, C. A. *Angew. Chem. Int. Ed.* **2007**, *46*, 4093–4096.

[72] Su, D.; Yang, X.; Xia, Q.; Chai, F.; Wang, C.; Qu, F. *RSC Adv.* **2013**, *3*, 24618–24624.

[73] Notarianni, M.; Vernon, K.; Chou, A.; Aljada, M.; Liu, J.; Motta, N. *Sol. Energy* **2014**, *106*, 23–37.

[74] Wu, X.; Liu, L.; Yu, T.; Yu, L.; Xie, Z.; Mo, Y.; Xu, S.; Ma, Y. *J. Mater. Chem. C* **2013**, *1*, 7020–7025.

[75] Wu, X.; Liu, L.; Deng, Z.; Nian, L.; Zhang, W.; Hu, D.; Xie, Z.; Mo, Y.; Ma, Y. *Part. Part. Syst. Char.* **2015**, *32*, 686–692.

[76] Choi, H.; Ko, S.-J.; Choi, Y.; Joo, P.; Kim, T.; Lee, B. R.; Jung, J.-W.; Choi, H. J.; Cha, M.; Jeong, J.-R.; Hwang, I.-W.; Song, M. H.; Kim, B.-S.; Kim, J. Y. *Nat. Photonics* **2013**, *7*, 732–738.

[77] Heo, M.; Cho, H.; Jung, J.-W.; Jeong, J.-R.; Park, S.; Kim, J. Y. *Adv. Mater.* **2011**, *23*, 5689–5693.

[78] Li, X.; Choy, W. C. H.; Huo, L.; Xie, F.; Sha, W. E. I.; Ding, B.; Guo, X.; Li, Y.; Hou, J.; You, J.; Yang, Y. *Adv. Mater.* **2012**, *24*, 3046–3052.

[79] Hartland, G. V. *Chem. Rev.* **2011**, *111*, 3858–3887.

[80] Zhang, J. Z. *Acc. Chem. Res.* **1997**, *30*, 423–429.

[81] Voisin, C.; Fatti, N. D.; Christofilos, D.; Vallée, F. *J. Phys. Chem. B* **2001**, *105*, 2264–2280.

[82] Wilson, O. M.; Hu, X.; Cahill, D. G.; Braun, P. V. *Phys. Rev. B* **2002**, *66*, 224301.

[83] Plech, A.; Kotaidis, V.; Grésillon, S.; Dahmen, C.; von Plessen, G. *Phys. Rev. B* **2004**, *70*, 195423.

[84] Juvé, V.; Scardamaglia, M.; Maioli, P.; Crut, A.; Merabia, S.; Joly, L.; Del Fatti, N.; Vallée, F. *Phys. Rev. B* **2009**, *80*, 195406.

[85] Aruda, K. O.; Tagliazucchi, M.; Sweeney, C. M.; Hannah, D. C.; Weiss, E. A. *Phys. Chem. Chem. Phys.* **2013**, *15*, 7441–7449.

[86] Ahmadi, T. S.; Logunov, S. L.; El-Sayed, M. A. *J. Phys. Chem.* **1996**, *100*, 8053–8056.

[87] Bauer, C.; Abid, J.-P.; Girault, H. H. *Chem. Phys.* **2005**, *319*, 409–421.

[88] Voisin, C.; Christofilos, D.; Del Fatti, N.; Vallée, F.; Prével, B.; Cottancin, E.; Lermé, J.; Pellarin, M.; Broyer, M. *Phys. Rev. Lett.* **2000**, *85*, 2200–2203.

[89] Voisin, C.; Christofilos, D.; Loukakos, P. A.; Del Fatti, N.; Vallée, F.; Lermé, J.; Gaudry, M.; Cottancin, E.; Pellarin, M.; Broyer, M. *Phys. Rev. B* **2004**, *69*, 195416.

[90] Bauer, C.; Abid, J.-P.; Fermin, D.; Girault, H. H. *J. Chem. Phys.* **2004**, *120*, 9302–9315.

[91] Link, S.; Burda, C.; Mohamed, M. B.; Nikoobakht, B.; El-Sayed, M. A. *Phys. Rev. B* **2000**, *61*, 6086.

[92] Varnavski, O.; Ramakrishna, G.; Kim, J.; Lee, D.; Goodson, T. *ACS Nano* **2010**, *4*, 3406–3412.

[93] Miller, S. A.; Womick, J. M.; Parker, J. F.; Murray, R. W.; Moran, A. M. *J. Phys. Chem. C* **2009**, *113*, 9440–9444.

[94] Hodak, J. H.; Martini, I.; Hartland, G. V. *J. Phys. Chem. B* **1998**, *102*, 6958–6967.

[95] Hartland, G. V. *Phys. Chem. Chem. Phys.* **2004**, *6*, 5263–5274.

[96] Arbouet, A.; Voisin, C.; Christofilos, D.; Langot, P.; Fatti, N. D.; Vallée, F.; Lermé, J.; Celep, G.; Cottancin, E.; Gaudry, M.; Pellarin, M.; Broyer, M.; Maillard, M.; Pileni, M. P.; Treguer, M. *Phys. Rev. Lett.* **2003**, *90*, 177401.

[97] Link, S.; Burda, C.; Wang, Z. L.; El-Sayed, M. A. *J. Chem. Phys.* **1999**, *111*, 1255–1264.

[98] Huang, W.; Qian, W.; El-Sayed, M. A.; Ding, Y.; Wang, Z. L. *J. Phys. Chem. C* **2007**, *111*, 10751–10757.

[99] Yau, S. H.; Varnavski, O.; Goodson, T. *Acc. Chem. Res.* **2013**, *46*, 1506–1516.

[100] Bauer, C.; Abid, J.-P.; Girault, H. H. *J. Phys. Chem. B* **2006**, *110*, 4519–4523.

[101] Groeneveld, R. H. M.; Sprik, R.; Lagendijk, A. *Phys. Rev. B* **1995**, *51*, 11433–11445.

[102] Inouye, H.; Tanaka, K.; Tanahashi, I.; Hirao, K. *Phys. Rev. B* **1998**, *57*, 11334–11340.

[103] Bauer, C.; Abid, J.-P.; Girault, H. H. *C R Chimie* **2006**, *9*, 261–267.

[104] Busby, M.; Chiorboli, C.; Scandola, F. *J. Phys. Chem. B* **2006**, *110*, 6020–6026.

[105] Polavarapu, L.; Xu, Q.-H. *Nanotechnology* **2009**, *20*, 185606.

[106] Hafiz, H. R.; Nakanishi, F. *Nanotechnology* **2003**, *14*, 649–654.

[107] Ma, J.; Xuan, L. *Displays* **2013**, *34*, 293–300.

[108] Shallcross, R. C.; Zacharias, P.; Köhnen, A.; Körner, P. O.; Maibach, E.; Meerholz, K. *Adv. Mater.* **2013**, *25*, 469–476.

[109] Qian, Y.; Xu, X.; Li, W.; Wang, J.; Wei, B.; Wei, Q.; Yan, X.; Hu, W.; Lu, Y.; Xie, L.; Zhang, X.; Huang, W. *Org. Electron.* **2015**, *26*, 476–480.

[110] Zacharias, P.; Gather, M. C.; Köhnen, A.; Rehmann, N.; Meerholz, K. *Angew. Chem. Int. Ed.* **2009**, *48*, 4038–4041.

[111] Zhang, Z.; Liu, X.; Li, Z.; Chen, Z.; Zhao, F.; Zhang, F.; Tung, C.-H. *Adv. Funct. Mater.* **2008**, *18*, 302–307.

[112] Kawata, S.; Kawata, Y. *Chem. Rev.* **2000**, *100*, 1777–1788.

[113] Corredor, C. C.; Huang, Z.-L.; Belfield, K. D. *Adv. Mater.* **2006**, *18*, 2910–2914.

[114] Yuan, W.; Sun, L.; Tang, H.; Wen, Y.; Jiang, G.; Huang, W.; Jiang, L.; Song, Y.; Tian, H.; Zhu, D. *Adv. Mater.* **2005**, *17*, 156–160.

[115] Li, H.; Xu, Q.; Li, N.; Sun, R.; Ge, J.; Lu, J.; Gu, H.; Yan, F. *J. Am. Chem. Soc.* **2010**, *132*, 5542–5543.

[116] Pieroni, O.; Fissi , A.; Angelini, N.; Lenci, F. *Acc. Chem. Res.* **2001**, *34*, 9–17.

[117] Venkataramani, S.; Jana, U.; Dommaschk, M.; Sönnichsen, F. D.; Tuczek, F.; Herges, R. *Science* **2011**, *331*, 445–448.

[118] Tong, R.; Chiang, H. H.; Kohane, D. S. *Proc. Nat. Acad. Sci. U.S.A.* **2013**, *110*, 19048–19053.

[119] Dommaschk, M.; Peters, M.; Gutzeit, F.; Schütt, C.; Näther, C.; Sönnichsen, F. D.; Tiwari, S.; Riedel, C.; Boretius, S.; Herges, R. *J. Am. Chem. Soc.* **2015**, *137*, 7552–7555.

[120] Szymański, W.; Beierle, J. M.; Kistemaker, H. A. V.; Velema, W. A.; Feringa, B. L. *Chem. Rev.* **2013**, *113*, 6114–6178.

[121] Feringa, B. L.; Browne, W. R. *Molecular Switches*; Wiley-WCH, Weinheim, 2011; Vol. 1 & 2.

[122] Browne, W. R.; Feringa, B. L. *Nat. Nanotechnol.* **2006**, *1*.

[123] Balzani, V.; Credi, A.; Venturi, M. *Chem. Soc. Rev.* **2009**, *38*, 1542–1550.

[124] Basheer, M. C.; Oka, Y.; Mathews, M.; Tamaoki, N. *Chem. Eur. J.* **2010**, *16*, 3489–3496.

[125] Muraoka, T.; Kinbara, K.; Aida, T. *Chem. Commun.* **2007**, 1441–1443.

[126] Bandara, H. M. D.; Burdette, S. C. *Chem. Soc. Rev.* **2012**, *41*, 1809–1825.

[127] Russew, M.-M.; Hecht, S. *Adv. Mater.* **2010**, *22*, 3348–3360.

[128] Yokoyama, Y. *Chem. Rev.* **2000**, *100*, 1717–1740.

[129] Renth, F.; Siewertsen, R.; Temps, F. *Int. Rev. Phys. Chem.* **2013**, *32*, 1–38.

[130] Irie, M. *Chem. Rev.* **2000**, *100*, 1685–1716.

[131] Berkovic, G.; Krongauz, V.; Weiss, V. *Chem. Rev.* **2000**, *100*, 1741–1754.

[132] Minkin, V. I. *Chem. Rev.* **2004**, *104*, 2751–2776.

[133] Füchsel, G.; Klamroth, T.; Dokic, J.; Saalfrank, P. *J. Phys. Chem. B* **2006**, *110*, 16337–16345.

[134] Crecca, C. R.; Roitberg, A. E. *J. Phys. Chem. A.* **2006**, *110*, 8188–8203.

[135] Perkampus, H.-H. *UV-VIS Atlas of Organic Compounds*, 2nd ed.; VCH: Weinheim, 1992; Vol. 1.

[136] Poprawa-Smoluch, M.; Baggerman, J.; Zhang, H.; Maas, H. P. A.; De Cola, L.; Brouwer, A. M. *J. Phys. Chem. A* **2006**, *110*, 11926–11937.

[137] Bahrenburg, J.; Röttger, K.; Siewertsen, R.; Renth, F.; Temps, F. *Photochem. Photobiol. Sci.* **2012**, *11*, 1210–1219.

[138] Gille, K.; Knoll, H.; Quitzsch, K. *Int. J. Chem. Kinet.* **1999**, *31*, 337–350.

[139] Rau, H. In *Photochromism: Molecules and Systems*; Dürr, H., Bouas-Laurent, H., Eds.; Elsevier: Amsterdam, 2003.

[140] Quick, M.; Dobryakov, A. L.; Gerecke, M.; Richter, C.; Berndt, F.; Ioffe, I. N.; Granovsky, A. A.; Mahrwald, R.; Ernsting, N. P.; Kovalenko, S. A. *J. Phys. Chem. B* **2014**, *118*, 8756–8771.

[141] Satzger, H.; Spörlein, S.; Root, C.; Wachtveitl, J.; Zinth, W.; Gilch, P. *Chem. Phys. Lett.* **2003**, *372*, 216–223.

[142] Satzger, H.; Root, C.; Braun, M. *J. Phys. Chem. A* **2004**, *108*, 6265–6271.

[143] Nägele, T.; Hoche, R.; Zinth, W.; Wachtveitl, J. *Chem. Phys. Lett.* **1997**, *272*, 489–495.

[144] Fujino, T.; Arzhantsev , S. Y.; ; Tahara, T. *J. Phys. Chem. A* **2001**, *105*, 8123–8129.

[145] Fujino, T.; Arzhantsev, S. Y.; Tahara, T. *Bull. Chem. Soc. Jpn.* **2002**, *75*, 1031–1040.

[146] Schmidt, B.; Sobotta, C.; Malkmus, S.; Laimgruber, S.; Braun, M.; Zinth, W.; Gilch, P. *J. Phys. Chem. A* **2004**, *108*, 4399–4404.

[147] Hsu, C.-C.; Wang, Y.-T.; Yabushita, A.; Luo, C.-W.; Hsiao, Y.-N.; Lin, S.-H.; Kobayashi, T. *J. Phys. Chem. A* **2011**, *115*, 11508–11514.

[148] Hirose, Y.; Yui, H.; Sawada, T. *J. Phys. Chem. A* **2002**, *106*, 3067–3071.

[149] Tamai, N.; Miyasaka, H. *Chem. Rev.* **2000**, *100*, 1875–1890.

[150] Bahrenburg, J.; Renth, F.; Temps, F.; Plamper, F.; Richtering, W. *Phys. Chem. Chem. Phys.* **2014**, *16*, 11549–11554.

[151] Comstock, M. J.; Levy, N.; Kirakosian, A.; Cho, J.; Lauterwasser, F.; Harvey, J. H.; Strubbe, D. A.; Fréchet, J. M. J.; Trauner, D.; Louie, S. G.; Crommie, M. F. *Phys. Rev. Lett.* **2007**, *99*, 038301.

[152] Wolf, M.; Tegeder, P. *Surf. Sci.* **2009**, *603*, 1506–1517.

[153] Tegeder, P. *J. Phys. Condens. Matter* **2012**, *24*, 394001.

[154] Benassi, E.; Corni, S. *J. Phys. Chem. C* **2014**, *118*, 25906–25917.

[155] Benassi, E.; Granucci, G.; Persico, M.; Corni, S. *J. Phys. Chem. C* **2015**, *119*, 5962–5974.

[156] Love , J. C.; Estroff, L. A.; Kriebel, J. K.; Nuzzo, R. G.; Whitesides, G. M. *Chem. Rev.* **2005**, *105*, 1103–1170.

[157] Hu, J.; Zhang, J.; Liu, F.; Kittredge, K.; Whitesell, J. K.; Fox, M. A. *J. Am. Chem. Soc.* **2001**, *123*, 1464–1470.

[158] Tamada, K.; Akiyama, H.; Wei, T. X. *Langmuir* **2002**, *18*, 5239–5246.

[159] Matsuda, K.; Ikeda, M.; Irie, M. *Chem. Lett.* **2004**, *33*, 456–457.

[160] Yamaguchi, H.; Ikeda, M.; Matsuda, K.; Irie, M. *Bull. Chem. Soc. Jpn.* **2006**, *79*, 1413–1419.

[161] Kawai, T.; Nakamura, S.; Sumi, A.; Kondo, T. *Thin Solid Films* **2008**, *516*, 8926–8931.

[162] Wang, R.; Iyoda, T.; Jiang, L.; Tryk, D. A.; Hashimoto, K.; Fujishima, A. *J. Electroanal. Chem.* **1997**, *438*, 213–219.

[163] Gahl, C.; Schmidt, R.; Brete, D.; McNellis, E. R.; Freyer, W.; Carley, R.; Reuter, K.; Weinelt, M. *J. Am. Chem. Soc.* **2010**, *132*, 1831–1838.

[164] Jung, U.; Schütt, C.; Filinova, O.; Kubitschke, J.; Herges, R.; Magnussen, O. *J. Phys. Chem. C* **2012**, *116*, 25943–25948.

[165] Wagner, S.; Leyssner, F.; Kordel, C.; Zarwell, S.; Schmidt, R.; Weinelt, M.; Ruck-Braun, K.; Wolf, M.; Tegeder, P. *Phys. Chem. Chem. Phys.* **2009**, *11*, 6242–6248.

[166] van Delden, R. A.; ter Wiel, M. K. J.; Pollard, M. M.; Vicario, J.; Koumura, N.; Feringa, B. L. *Nature* **2005**, *437*, 1337–1340.

[167] Lakowicz, J.; Geddes, C.; Gryczynski, I.; Malicka, J.; Gryczynski, Z.; Aslan, K.; Lukomska, J.; Matveeva, E.; Zhang, J.; Badugu, R.; Huang, J. *J. Fluoresc.* **2004**, *14*, 425–441.

[168] Dulkeith, E.; Morteani, A. C.; Niedereichholz, T.; Klar, T. A.; Feldmann, J.; Levi, S. A.; van Veggel, F. C. J.; Reinhoudt, D. N.; Möller, M.; Gittins, D. *Phys. Rev. Lett.* **2002**, *89*, 203002–1.

[169] Kittredge, K. W.; Fox, M. A.; Whitesell, J. K. *J. Phys. Chem. B* **2001**, *105*, 10594–10599.

[170] Barazzouk, S.; Kamat, P. V.; Hotchandani, S. *J. Phys Chem. B* **2005**, *109*, 716–723.

[171] Fan, C.; Wang, S.; Hong, J. W.; Bazan, G. C.; Plaxco, K. W.; Heeger, A. J. *Proc. Nat. Acad. Sci. U.S.A.* **2003**, *100*, 6297–6301.

[172] Ahonen, P.; Schiffrin, D. J.; Paprotny, J.; Kontturi, K. *Phys. Chem. Chem. Phys.* **2007**, *9*, 651–658.

[173] Klajn, R.; Bishop, K. J. M.; Grzybowski, B. A. *Proc. Nat. Acad. Sci. U. S. A.* **2007**, *104*, 10305–10309.

[174] Klajn, R.; Wesson, P. J.; Bishop, K. J. M.; Grzybowski, B. A. *Angew. Chem. Int. Ed.* **2009**, *48*, 7035 –7039.

[175] Köhntopp, A.; Dabrowski, A.; Malicki, M.; Temps, F. *Chem. Commun.* **2014**, *50*, 10105–10107.

[176] Lee, J.-W.; Klajn, R. *Chem. Commun.* **2015**, *51*, 2036–2039.

[177] Zep, A.; Wojcik, M. M.; Lewandowski, W.; Sitkowska, K.; Prominski, A.; Mieczkowski, J.; Pociecha, D.; Gorecka, E. *Angew. Chem. Int. Ed.* **2014**, *53*, 13725–13728.

[178] Sen, T.; Patra, A. *J. Phys. Chem. C* **2008**, *112*, 3216–3222.

[179] Karthikeyan, B. *J. Appl. Phys.* **2010**, *108*, 084311.

[180] Debnath, T.; Dana, J.; Maity, P.; Lobo, H.; Shankarling, G. S.; Ghosh, H. N. *Chem. Eur. J.* **2015**, *21*, 5704–5708.

[181] Dana, J.; Debnath, T.; Maity, P.; Ghosh, H. N. *J. Phys. Chem. C* **2015**, *119*, 2046–2052.

2

EXPERIMENTAL SECTION AND DATA ANALYSIS

The ultrafast dynamics taking place in molecular photochromic switches and in gold nanoparticles (AuNPs) after excitation by a short laser pulse are of great importance for the understanding of the light-induced property changes in hybrid systems consisting of both components due to their use in various applications. The deactivation processes in molecular switches and AuNPs after excitation usually occur on the femtosecond to picosecond timescale. Spectroscopic investigation of these ultrafast processes therefore requires highly sensitive methods with a corresponding time resolution. A widely employed concept for the realisation of ultrafast measurements is the pump-probe principle depicted in Figure 2.1. The sample molecules are excited by an ultrashort laser pulse of appropriate wavelength. The molecular response is probed with another ultrashort laser pulse, which can be temporally delayed with respect to the pump pulse by a delay stage. The delay stage can be set to a number of different temporal delay times Δt, enabling a step-by-step detection of the dynamics over a large time window. Thus, the pump-probe concept allows for the detection of processes that are much faster than the response times of any available detectors. The time resolution is limited only by the temporal widths of the pump and probe laser pulses.

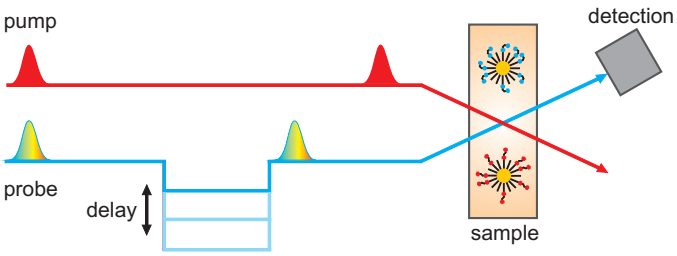

Figure 2.1: Scheme of the pump-probe principle.

The generation of laser pulses with different wavelengths from a single fundamental wavelength is realised through several nonlinear optical processes, which include second harmonic generation (SHG), third harmonic generation (THG), sum-frequency generation (SFG), difference-frequency generation (DFG), super continuum generation (SCG) and optically parametric amplification (OPA). All these processes are described in various textbooks[1–4] and theses of the workgroup[5–9] and will therefore not be explained in detail here.

In the scheme of this Thesis, femtosecond time-resolved transient absorption spectroscopy has been used to follow the ultrafast dynamics of azobenzene (AB) and some AB derivatives in solution and on

AuNP surfaces. The same setup has also been employed to investigate the electron cooling dynamics of AuNPs functionalized with different aromatic ligands after laser excitation. Additional spectroscopic techniques include static UV/Vis absorption spectroscopy, NMR spectroscopy and transmission electron microscopy (TEM), which can be considered standard techniques and will not be explained here.

2.1 FEMTOSECOND TRANSIENT ABSORPTION SPECTROSCOPY

The present experiments use a Ti:Sa laser (Clark-MXR CPA 2001) which delivers 1000 µJ pulses of 150 femtosecond duration (FWHM) at a repetition rate of 1010 Hz with a center wavelength of 775 nm. The details of the Ti:Sa laser system can be found in other theses of the work group.[5–7] Half of the laser output (500 µJ) was used to operate the transient absorption setup, the other half is used for a femtosecond time-resolved fluorescence up-conversion setup in our laboratory and laser diagnostics.

A schematic overview of the transient absorption setup as used for the measurements presented in this Thesis is shown in Figure 2.2. For the detection of dynamics in the deep-UV below $\lambda = 300$ nm an additional single-color probe scheme can be implemented into the setup. The details of the complete setup are given elsewhere,[10,11] explanation will therefore be limited to general aspects of pump and probe pulse generation and detection in the following paragraphs. The data analysis procedures are detailed in Section 2.3.

PUMP PULSE GENERATION

A non-collinear optical parametric amplifier (NOPA) operated with 250 µJ 387 nm pulses (by frequency doubling of the Ti:Sa fundamental beam) generated pump pulses of different wavelengths (450 nm $\leqslant \lambda \leqslant$ 700 nm) with typical energies of 5-20 µJ depending on wavelength. The operating principle and handeling of a NOPA are described in various theses of the work group.[7,9,12] The pulses delivered by the NOPA were temporally compressed to $\Delta t \approx 30 - 50$ fs in a prism compressor using two BK7, SF10 or F2 prisms (depending on the wavelength). The typical pulse energies after compression were 3-15 µJ. The compressed pulses were either used directly for excitation in the visible or focused into a β-bariumborate (BBO) crystal of appropriate cut angle for second harmonic generation (SHG) and then used for excitation in the UV. To ensure a Gaussian lineshape, the pump pulses were characterized temporally using an autocorrelator (APE, PulseScope). Temporal as well as spectral characterization of pulses in the visible and near IR is possible with an SHG FROG (Frequency-Resolved Optical Gating). After passing a half-waveplate used to set the polarization of the pump light to the magic angle

(54.7 °) with respect to the broadband probe pulses, the beam was focused into the sample cell. A large focus diameter of ~ 500 µm was needed to avoid damage to the AuNPs, which quickly becomes visible by the deposition of melted AuNPs on the cell window at the position of the pump beam. The pulse energy was attenuated to 0.1-0.3 µJ with a pinhole. An optical chopper was used to block every second laser pulse in order to detect background spectra of the probe pulses without excitation.

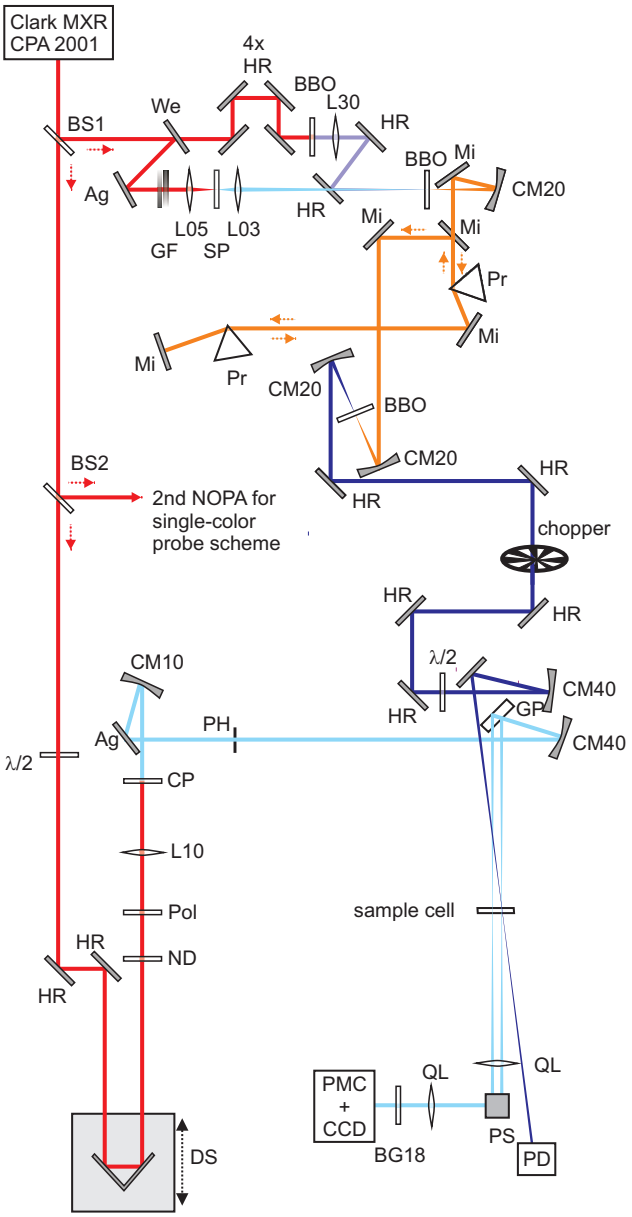

Ag	planar Ag mirror
BBO	β-BaB_2O_4 crystal
BG18	BG18 filter
BS1	beamsplitter, R=50%
BS2	beamsplitter, R=70%
CCD	FFT-CCD cameras
CM20	concave mirror, rcc = 0.2 m
CM40	concave mirror, rcc = 0.4 m
CP	CaF_2 plate (d = 2 mm)
DS	delay stage with retroreflector
GF	gradient filter
GP	quartz glass plate (planar)
HR	high reflective mirror
λ/2	half-wave plate
L03	lens, f = 30 mm
L05	lens, f = 50 mm
L10	lens, f = 100 mm
L30	lens, f = 300 mm
Mi	planar Ag or Al mirror
ND	neutral density filter
PD	photodiode
Pol	polarizer
PH	pinhole
PMC	prism monochromator
Pr	BK7, F2 or SF10 prism
PS	periscope
QL	quartz lens
SP	sapphire plate
We	wedge (30´)

Figure 2.2: Scheme of the transient absorption setup (left) and abbreviations for the optical components (right). The colors of the beams are chosen arbitrarily and do not reflect real wavelengths used in experiments.

BROADBAND PROBE PULSE GENERATION

In a second part of the experiment, $\approx 75\,\mu J$ of the laser fundamental passed a computer controlled delay stage with a retroreflector, before broadband probe pulses in the range $320\text{ nm} \leqslant \lambda \leqslant 750\text{ nm}$ were generated in a CaF_2 plate. The damage threshold of the used 2 mm thick CaF_2 plate is very low and requires a constant movement of the plate as well as precise adjustment of the energy to achieve stable whitelight generation. Therefore, the plate was continuously moved horizontally and vertically to ensure a fresh spot was hit by every laser pulse. The energy was first attenuated by a neutral density filter and afterwards adjusted precisely by the combination of a half-waveplate and a polarizer positioned in front of the CaF_2 plate. As even small changes in the energy of the laser fundamental focused on the CaF_2 plate lead to instabilities in the broadband pulse generation, the energy had to be re-adjusted every day. A detailed description of the white-light spectrum, its optimization and the stability are given in previous Theses of the work group.[9,11] After the CaF_2 plate the broadband probe pulses were split into probe and reference beam using a thin quartz plate and focused into the sample cell. The probe pulses with a focal diameter of $\approx 100\,\mu m$ were overlapped temporally and spatially with the pump pulses, the reference pulses passed unexcited sample.

PROBE PULSE DETECTION

After passing the sample cell the probe and reference pulses were directed into a prism spectrograph, where they were spectrally dispersed, separated and independently detected by two FFT-CCD cameras. The cameras were read out with the laser repetition frequency by a computer, which then calculated the change in optical density. The pump pulses were detected by a photodiode, to determine whether the pump beam was open or blocked at the time of broadband detection. Further details regarding the detection system and the home-written LabVIEW programm used to controll the experiment can be found in the Thesis of K. Röttger.[11]

All transient absorption measurements were performed in toluene solution in home-made flow cells with 0.2 mm quartz windows and 1 mm optical pathlength. The cell was connected to a sample reservoir with Viton Fluran tubing and the solution was pumped through the cell with a perstaltic pump to provide fresh sample for every laser shot. Unless stated otherwise every measurement was repeated three times to verify reproducibility of the results. All other details regarding the measurements such as excitation wavelengths and energies can be found in the corresponding paragraphs of Chapters 4-6.

2.2 DATA PROCESSING

2.2.1 CALCULATION OF THE CHANGE IN OPTICAL DENSITY

The absorbance $A(\lambda, \Delta t)$ of a sample is the negative logarithm of intensity of the probe pulses I_{pr} divided by the intensity of the reference pulses I_{ref}:

$$A(\lambda, \Delta t) = -\log\left(\frac{I_{pr}}{I_{ref}}\right). \tag{2.1}$$

Thus, the change in optical density is calculated as the difference of absorption of excited and unexcited molecules A^* and A^0 respectively:

$$\Delta OD(\lambda, \Delta t) = A^*(\lambda, \Delta t) - A^0(\lambda). \tag{2.2}$$

A^* and A^0 are the absorbances of two consecutive laser pulses, allowing for calculation of $\Delta OD(\lambda, \Delta t)$ directly during the measurement as

$$\Delta OD(\lambda, \Delta t) = -\log\left(\frac{I_{pr}(\lambda, \Delta t) \cdot I^0_{ref}(\lambda, \Delta t)}{I^0_{pr}(\lambda, \Delta t) \cdot I_{ref}(\lambda, \Delta t)}\right) \tag{2.3}$$

with $I^0_{pr/ref}$ being the respective pulse intensities detected for unexcited sample molecules (pump blocked) and $I_{pr/ref}$ the respective pulse intensities for excited sample molecules (pump not blocked).

2.2.2 COHERENT ARTIFACTS

Coherent artifacts unrelated to the measured sample appear in liquid-phase transient absorption spectra around time-zero due to interaction between the intense pump pulse and the weaker probe pulse. The observed artifacts include cross-phase modulation (XPM), multi-photon or two-photon absorption (2PA or TPA), and stimulated Raman scattering (SRS) and can be very intense, thereby obscuring the sample signals at early delay times.

XPM occurs as a result of the refractive index modulation in cell windows and solvent induced by the intense pump pulse, which leads to a redistribution of the frequencies in the chirped broadband probe pulses. As the spectral redistribution only takes place in the probe pulses and not the reference pulses of the supercontinuum, a change in optical density is recorded during the interaction time of pump and probe, that is around time zero. The spectral and temporal forms of the XPM strongly depend on the chirp of the probe pulses, the temporal and spectral distribution of the pump pulse, the length of the sample cell, the thickness of the cell windows, and the volume in which pump and probe interact (through the angle between

beams and beam diameter).[13–15] 2PA takes place when the solvent or cell windows simultaneously absorb a pump and a probe photon. SRS occurs when the pump and probe pulses coherently interact in a medium with a vibrational resonance at the pump-probe difference frequency. SRS can be taken as the pump-probe cross-correlation function and therefore be used to determine the time resolution of the experiment.[14] A more detailed description of XPM and SRS can also be found in the Thesis of R. Siewertsen.[9]

All the abovementioned artifacts can provide information about the time resolution and chirp of the pump and probe pulses. However, reduction of the artifact intensity before measurement and correction of the spectra after measurement are of great importance to enable a reliable analysis of transient absorption measurements. In order to correct the sample spectra for the coherent artifacts, a measurement of the neat solvent under the same conditions as the sample measurements is necessary.

Additional to the coherent artifacts, scattered pump light is visible in the spectra when the excitiation wavelength lies within the wavelength range covered by the broadband probe pulses. Through careful optimization of the setup the intensity was minimized before measurement, afterwards it could be reduced further through background correction of the spectra. To these ends, the spectra before time-zero were used as a reference for the shape and intensity of the superimposed pump light signal, which could simply be subtracted from all subsequent spectra of the same measurement. However, in some cases when scattering was intensified by the AuNPs complete removal was not possible.

2.3 DATA ANALYSIS

Wavelength calibration of the measured two-dimensional transient absorption maps was done with a number of bandpass interference filters covering the spectral range of $\lambda = 330 - 650$ nm.[11] The experimental time-zero depends on the chirp of the broadband probe pulses and therefore is different for every probe wavelength. A time-zero-correction of the obtained two-dimensional transient absorption maps is therefore necessary before extraction of transient absorption spectra. Details of the correction procedure have been described elsewhere.[9] Wavelength calibration and time-zero correction as well as the correction for the coherent artifacts have been performed with a self-written MATHEMATICA[16] program.[9,11] In the same program non-linear least-squares fitting routines based on the Levenberg-Marquardt algorithm needed for description of the transient absorption time-profiles are implemented. For fitting of the transient absorption spectra with a temperature-dependent Mie theory model, another MATHEMATICA program was used.

2.3.1 FITTING OF TIME PROFILES

Measured absorption-time profiles were generally described with a sum of exponential decay functions of the form

$$A_\lambda(t) = \sum_i a_i \times \exp\left(-\frac{t}{\tau_i}\right) \tag{2.4}$$

with a_i as the amplitude, t as delay time and τ_i as the decay time. To take the temporal width of the pulses into account the sum of exponentials was convoluted with a Gaussian-shaped instrument response function (IRF) of the form

$$G(t, \sigma_{IRF}) = \frac{1}{\sigma_{IRF}\sqrt{2\pi}} \times \exp\left(-\frac{t - t_0}{2\sigma_{IRF}^2}\right). \tag{2.5}$$

Here, σ_{IRF} is the time resolution of the experiment and is correlated to the full width at half maximum of the IRF by

$$IRF_{FWHM} = \sqrt{8 \times \ln 2} \times \sigma_{IRF}. \tag{2.6}$$

The time resolution was usually of the order of $\Delta t \approx 100$ fs, depending on the excitation wavelength. Due to the use of toluene as a solvent and a relatively large absorption pathlength of 1 mm, this value is larger than in other reported measurements performed with the same experimental setup.[11,17]

The overall fitting routine used a function of the form

$$\Delta OD(\lambda, \Delta t) = A_\lambda(t) \otimes G(t, \sigma_{IRF}). \tag{2.7}$$

Correction functions for coherent artifacts at selected wavelengths were obtained by fitting the signal of the neat solvent at that wavelength with a sum of Gaussians and, if necessary, with additional exponentials. The correction functions were subsequently scaled with appropriate factors to account for the higher optical density of the sample solution and included in the fitting routine as described elsewhere.[11]

2.3.2 FITTING OF TRANSIENT SPECTRA

The transient absorption spectra were analyzed using the temperature-dependent Mie theory model proposed by Aruda et al.[18] The model is based on the works of Rosei et al.[19], Scaffardi et al.[20] and Inouye et al.[21] and decomposes the complex dielectric function of AuNPs $\epsilon(T_e)$ into contributions of free and bound electrons. The free electrons are responsible for intraband transitions in the conduction band of the AuNPs. Their dielectric function is described with the Drude model

$$\epsilon_{\text{free}}(\omega) = 1 - \frac{\omega_P^2}{\omega^2 + i\gamma_{\text{free}}\omega} \tag{2.8}$$

where ω_P is the plasma frequency of Au, ω is the frequency of the incident light and γ_{free} is the width parameter of the intraband transitions, which depends on NP size, surface chemistry and the electronic temperature.

The bound electrons are responsible for interband transitions from the valence band to the conduction band (*d-sp* transitions). The dielectric function is described depending on the Fermi-Dirac distribution $F(x, T_e)$ and a width parameter for the interband transitions, γ_{bound}:

$$\begin{aligned}\epsilon_{\text{bound}}(\omega, T_e) = Q_{\text{bulk}} \int_{\omega_g}^{\infty} & \frac{\sqrt{x - \omega_g}}{x}[1 - F(x, T_e)] \\ & \times \frac{(x^2 - \omega^2 + \gamma_{\text{bound}}^2 + i2\omega\gamma_{\text{bound}})}{(x^2 - \omega^2 + \gamma_{\text{bound}}^2)^2 + 4\omega^2\gamma_{\text{bound}}^2}\, dx\end{aligned} \tag{2.9}$$

Q_{bulk} is a constant determining the contribution of the bound electrons to the overall dielectric function, ω_g is the gap frequency (from the gap energy) of gold.

The overall dielectric function $\epsilon(T_e)$ is simply the sum of both contributions, which then enters into the absorption cross section of AuNPs:

$$Q_{\text{abs}}(T_e) = C\frac{a}{\lambda}\frac{\epsilon''(T_e)}{\epsilon''(T_e)^2 + (\epsilon'(T_e) + 2\epsilon_m)^2}. \tag{2.10}$$

ϵ_m is the dielectric constant of the medium, $\epsilon'(T_e)$ and $\epsilon''(T_e)$ are the real and imaginary parts of $\epsilon(T_e)$, respectively, a is the particle radius and C is a constant used to scale the spectra to the correct intensity. The fitting parameters obtained herein are the width parameters γ_{free} and γ_{bound} as well as the electronic temperature T_e.

In the fitting procedure, equation (2.10) is first used for fits to the static absorption spectrum in order to obtain parameters for the unexcited sample. Here, the electronic temperature was fixed to $T_e = 298$ K, the values of the constants used are given in Table 2.1.

All measurements were performed in toluene, which has a dielectric constant of 2.38.[22] However, fits using this value for the dielectric constant of the medium ϵ_m did not describe the experimental data well. The dielectric constant in the immediate vicinity of the AuNPs is likely to be changed upon ligand attachment.[23] Therefore, ϵ_m was adjusted manually to a value which gave good-quality fits to the measured static absorption data. Figure 2.3 shows a comparison of two fits to the absorption spectra of decanethiol-coated AuNPs using $\epsilon_m = 2.38$ and $\epsilon_m = 2.1$, respectively. The latter gives a greatly

Table 2.1: Parameters used in the temperature-dependent Mie theory model fit. Q_{bulk} is a constant determining the contribution of bound electrons to $\epsilon(T_e)$, ω_P is the plasma frequency, E_F is the Fermi energy, E_g is the gap energy of gold. The values were determined by Scaffardi et al.[20].

Parameter	value
Q_{bulk}	$1.3 \cdot 10^{24}$
ω_P	$13 \cdot 10^{15}$ Hz
E_F	2.5 eV
E_g	2.1 eV

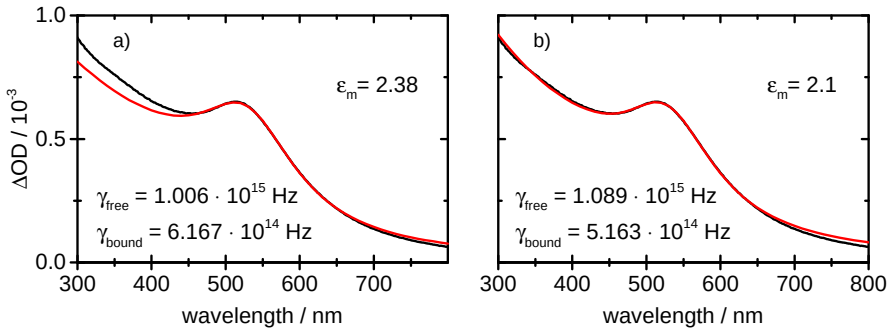

Figure 2.3: Fits to the measured static absorption spectrum of C10SAuNPs using a) $\epsilon_m = 2.38$ and b) $\epsilon_m = 2.1$. The experimental spectrum is shown in black, the fit in red. The respective fit parameters are given in the graphs.

improved fit to the experimental spectrum at shorter wavelengths. The fitting parameters γ_{free} and γ_{bound} for both ϵ_m values given in the graphs. They differ by approximately 10 %, which is considerably more than their 2σ uncertainties of <1 % obtained from the fits. Therefore, adjustment of ϵ_m is reasonable to accurately determine the AuNP ground state parameters.

Furthermore, the fitting routine includes a weighting matrix, which weights the data points around the LSPR ($\lambda = 430 - 650$ nm) higher than those at the edges of the spectrum. Differentiated weighting of the data points further improves the fit quality.

The transient spectra were fitted as the difference between the absorption spectrum at higher electronic temperatures $Q^*_{abs}(T_e)$ and the ground state spectrum at $T_e = 298$ K, $Q^0_{abs}(298\,K)$:

$$\Delta OD(T_e) = Q^*_{abs}(T_e) - Q^0_{abs}(298\,K) \tag{2.11}$$

The transient spectra were usually analyzed in the wavelength range of $440\,nm \leqslant \lambda \leqslant 650$ nm, which includes the LSPR bleach minimum and both maxima immediately left and right of the bleach. Outside this range the model is not able to describe the data with sufficient accuracy.[18] To achieve a better description of the data inside

the selected range a weighting matrix was used. Figure 2.4 shows three selected transient absorption spectra of C10SAuNPs with the higher weighted data points highlighted in each spectrum. Generally, the three data points at the bleach minimum and the one close to the point where the spectra cross the zero line ($\lambda \approx 585$ nm) were weighted 30 times higher than the unspecified data points. The two data points around $\lambda = 470$ nm were weighted 16 times higher and the remaining highlighted data points 10 times higher than the unspecified data points. In order to account for small shifts in the signal positions, the weighting matrix has to be adjusted for every new batch of AuNPs, that is every series of measurements. The same weighting matrix was then used for all transient spectra of the same sample as well as for all samples measured under the same conditions.

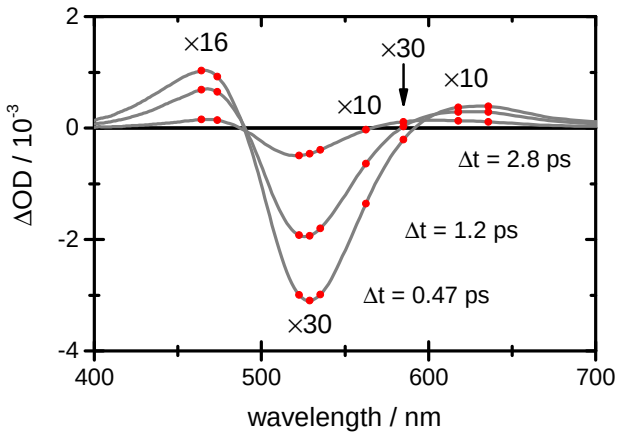

Figure 2.4: Transient absorption spectra of C10SAuNPs at three selected delay times of $\Delta t = 0.47, 1.2$ and 2.8 ps. The higher weighted data points are highlighted and their weight relative to the unspecified data points is given.

Usually the data were solvent corrected before fitting, but to avoid errors due to incomplete solvent subtraction the analysis started at $\Delta t \approx 0.5$ ps. For each sample approximately 15-20 transient spectra at delay times up to $\Delta t \approx 12$ ps were selected and fitted separately based on equation (2.11). The fit parameters γ_{free}, γ_{bound} and T_e obtained therein were then used as starting values for a simultaneous fit of all transient spectra of one sample. The constant factor C from the individual fits was replaced by a global scaling factor C′ common for all spectra in the simultaneous fit. The starting value for C′ is the mean of all C values from the individual fits.

The quality of the simultaneous fit was checked using the R^2 value provided by the nonlinear fitting routine in MATHEMATICA.[16] It was $R^2 \geqslant 0.99$ for all samples presented in this Thesis. The standard deviation of the obtained fit parameters was typically $\Delta\gamma_{free/bound} = 1 \cdot 10^{12}$ Hz, which corresponds to an error less than 1 %, and $\Delta T_e =$

120 − 10 K. Depending on the absolute temperature this corresponds to an error of $\Delta T_e \approx 10$ % in all cases.

In the last analysis step the electronic temperatures T_e were plotted against the delay time and the decaying part of the temperature-time profile was fitted with an exponential decay function of the form

$$T_e(t) = 298\,K + A_1 \cdot \exp\frac{-x}{\tau_1} + A_2 \cdot \exp\frac{-x}{\tau_2} \tag{2.12}$$

using ORIGIN 9.0 software. An example of a typical temperature-time profile with a biexponential fit and both individual components is shown in Figure 2.5.

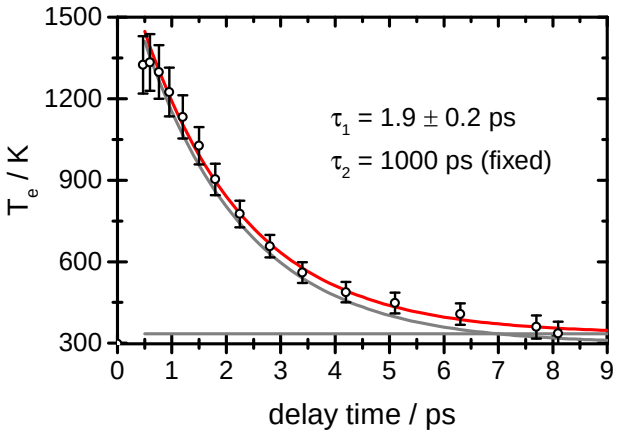

Figure 2.5: A temperature-time profile of C10SAuNPs (open circles) including error bars with the respective biexponential fit to the data (red). The individual components of the biexponential fit are shown in grey. The decay time of the second component is fixed and the amplitude is very small.

For all temperature-time profiles presented in this thesis, unless stated otherwise, a second exponential with a fixed decay time of $\tau_2 = 1000$ ps and a very small amplitude (< 3 %) was used to satisfactorily describe the data at longer delay times ($\Delta t \geqslant 6$ ps). The second exponential corresponds to the ph-ph coupling process in the AuNP, which usually occurs within 10 − 100 ps. It is present already at relatively early delay times due to an overlap of the e^--ph and ph-ph coupling time scales as described in Chapter 1.1.2. However, the process is not completed within the analyzed time frame and the timeconstant, $\tau_{ph\text{-}ph}$, can not be determined.

BIBLIOGRAPHY

[1] Boyd, R. W. *Nonlinear Optics*, 2nd ed.; Academic Press, San Diego, London, 2003.

[2] Abramczyk, H. *Introduction to Laser Spectroscopy*, 1st ed.; Elsevier, Amsterdam, 2005.

[3] Demtröder, W. *Laserspektroskopie: Grundlagen und Techniken*, 5th ed.; Springer, Berlin, Heidelberg, 2007.

[4] Meschede, D. *Optik, Licht und Laser*, 3rd ed.; Vieweg+Teubner, Wiesbaden, 2008.

[5] Pancur, T. Untersuchung der Isomerisierungsdynamik von Azobenzolen und der strahlungslosen Desaktivierung von Nukleobasen mit Hilfe der Femtosekunden-Fluoreszenzspektroskopie. PhD Thesis, CAU Kiel, 2004.

[6] Foca, M. Investigations of Ultrafast Photoisomerization of Photochromic Molecular Switches by fs-Time-Resolved Transient Absorption Spectroscopy. PhD Thesis, CAU Kiel, 2005.

[7] Studzinski, H. Ultrafast Radiationless Dynamics of Selected Electronically Excited Aromatic Molecules by Femtosecond Time-Resolved Mass Spectrometry and Photoelectron Imaging. PhD Thesis, CAU Kiel, 2007.

[8] Schwalb, N. Ultrafast Electronic Deactivation Dynamics in DNA Model Systems by Femtosecond UV Fluorescence Spectroscopy. PhD Thesis, CAU Kiel, 2009.

[9] Siewertsen, R. Ultrafast Photochromic Reactions of Structurally Modified Furylfulgides and a Bridged Azobenzene. PhD Thesis, CAU Kiel, 2011.

[10] Röttger, K.; Siewertsen, R.; Temps, F. *Chem. Phys. Lett.* **2012**, *536*, 140–146.

[11] Röttger, K. Ultrafast Deactivation Dynamics of Structurally Modified and Hydrogen-Bonded DNA and RNA Building Blocks. PhD Thesis, CAU Kiel, 2013.

[12] Studzinski, H. Aufbau und Charakterisierung eines nichtkollinearen optisch-parametrischen Verstärkers. Diploma Thesis, CAU Kiel, 2002.

[13] Ekvall, K.; van der Meulen, P.; Dhollande, C.; Berg, L.-E.; Pommeret, S.; Naskrecki, R.; Mialocq, J.-C. *J. Appl. Phys.* **2000**, *87*, 2340.

[14] Lorenc, M.; Ziolek, M.; Naskrecki, R.; Karolczak, J.; Kubicki, J.; Maciejewski, A. *Appl. Phys. B* **2002**, *74*, 19–27.

[15] Dobryakov, A. L.; Kovalenko, S. A.; Ernsting, N. P. *J. Chem. Phys.* **2005**, *123*, 044502.

[16] Wolfram Research, I. *Mathematica*, version 8.0 ed.; Wolfram Research, Inc., 2010.

[17] Bahrenburg, J. Ultrafast Photochemical Dynamics of Azobenzenes Affected by Intra- and Intermolecular Interactions and of a Proton Transfer Switch. PhD Thesis, CAU Kiel, 2014.

[18] Aruda, K. O.; Tagliazucchi, M.; Sweeney, C. M.; Hannah, D. C.; Schatz, G. C.; Weiss, E. A. *Proc. Nat. Acad. Sci. U.S.A.* **2013**, *110*, 4212–4217.

[19] Rosei, R.; Antonangeli, F.; Grassano, U. M. *Surf. Sci.* **1973**, *37*, 689–699.

[20] Scaffardi, L. B.; Tocho, J. O. *Nanotechnology* **2006**, *17*, 1309–1315.

[21] Inouye, H.; Tanaka, K.; Tanahashi, I.; Hirao, K. *Phys. Rev. B* **1998**, *57*, 11334–11340.

[22] Weast, R. C., Ed. *CRC Handbook of Chemistry and Physics*, 1st ed.; CRC Press, 1987; pp E44–E46.

[23] Goldmann, C.; Lazzari, R.; Paquez, X.; Boissière, C.; Ribot, F.; Sanchez, C.; Chanéac, C.; Portehault, D. *ACS Nano* **2015**, *9*, 7572–7582.

Part II

RESULTS

3

PHOTOISOMERIZATION AND LIGAND-CONTROLLED REVERSIBLE AGGREGATION OF AZOBENZENE-FUNCTIONALIZED GOLD NANOPARTICLES

Anja Köhntopp, Alexandra Dabrowski, Michal Malicki and Friedrich Temps*

Institut für Physikalische Chemie, Christian-Albrechts-Universität zu Kiel, Olshausenstr. 40, 24098 Kiel, Germany

A. Köhntopp, A. Dabrowski, M. Malicki and F. Temps *Chem. Commun.*, **2014**, *50*, 10105-10107.

OWN CONTRIBUTIONS TO THIS MANUSCRIPT:

- Synthesis of functionalized gold nanoparticles
- Static absorption spectroscopy
- Analysis of the aggregation dynamics and calculation of the NP composition
- Writing of the manuscript

* To whom correspondence should be addressed. E-mail: temps@phc.uni-kiel.de

ABSTRACT

The photochemical behaviour of functionalised gold nanoparticles (AuNPs) carrying azobenzenethiolate-alkylthiolate monolayers was investigated. Repeated *trans-cis* and *cis-trans* isomerisation cycles could be performed in all cases with high efficiency. Reversible photoinduced aggregation was observed when azothiolates with long alkyl spacers ($\geqslant C_7$) were combined with short (C_5) alkylthiolate coligands. The choice of a coligand thus offers control over the aggregation properties of the nanoparticles.

3.1 RESULTS AND DISCUSSION

Functionalised nanoparticles have gained tremendous importance in fundamental and applied sciences because of their unique, size-dependent optical, electronic, magnetic and chemical properties with potential application in medical diagnostics, drug delivery, cancer therapy, nanoelectronics and information storage, imaging and super resolution microscopy, sensors, solar energy conversion, (photo)catalysis, surface coatings or the development of smart materials.[1–3] Currently, particular interest exists in nanoparticles with surface-bound molecular switches that can be controlled by ultraviolet or visible light.[4] Unlike in solution, however, the photoswitching properties of molecules on surfaces are subject to several mechanisms affecting or hindering the outcome: first, dense packing of the surface-bound molecules may leave too little free space for the transformation to proceed, especially when a photoisomerisation is associated with a large-amplitude structural change.[4–7] Second, energy transfer either between the attached switches or between the switch and the nanoparticle substrate may lead to a rapid electronic deactivation of the photoexcited molecules and even prevent the reaction altogether.[7] A third major issue arises when a change in properties of NPs upon isomerisation of the switches in the ligand shell leads to aggregation of the NPs. This effect may impede further switching after only a few cycles.[5] In cases where aggregation is desired, it is of great importance to control the process and the structure of the aggregates.[8–10] Klajn and coworkers for example studied the behaviour of azobenzene (AB) functionalised AuNPs as a function of AB concentration and solvent polarity and found different types of aggregates under varying conditions.[11,12]

Here, we report on AB-functionalised AuNPs with high surface coverage in solution in toluene that can be repeatedly photoswitched back and forth between their *trans* and *cis* forms and additionally show virtually fully reversible aggregation when they are in the *cis* state. We evaluated the surface concentration of AB molecules on the AuNPs independently by UV/Vis spectroscopy and by NMR spec-

troscopy and determined the *cis/trans*-AB compositions in the photostationary states upon irradiation with UV and Vis light. We found that the aggregation potential of the functionalised AuNPs can be controlled through the choice of the alkylthiolate coligand. Evidently, the tendency for aggregation due to attractive dipole-dipole forces between the NP-bound *cis*-ABs depends strongly on the chain length of the coligand and besides the AB surface coverage.

For our investigation of the photoswitching properties of ABs on the gold surface, we functionalised AuNPs with AB-derivatised alkylthiols (azothiols) as ligands and normal alkylthiols as coligands in mixed monolayers (see Fig. 3.1A and B) by ligand exchange from amine-stabilised NPs in mixed solutions (molar fractions $x_{AB} = 0.3$, 0.5 or 0.7) of azothiol and alkylthiol as detailed in the ESI.† The alkyl (spacer) lengths of the thiols were systematically varied (Fig. 3.1B). The obtained NPs were characterised using transmission electron microscopy (TEM), NMR and UV/Vis spectroscopy. A typical TEM image is displayed in Fig. 3.1C. It shows that the synthesis yielded nearly spherical products with diameters typically of $\sim 4.0 \pm 0.8$ nm (single standard deviation). Considering the macroscopic density ($\rho_{Au} = 19.3\ g\,cm^{-3}$), the NPs should consist of ~ 2000 Au atoms. ^{1}H NMR spectra confirmed the purity of the functionalised NPs (see Fig. 3.1D). For organic molecules on AuNPs, the ^{1}H NMR signals are strongly broadened inhomogeneously and due to much faster spin-spin relaxation[13] so that surface-bound and free ligand molecules in the sample solution can be easily distinguished. The absence of sharp signals of free AB thiols in the measured NMR spectrum thus demonstrates that practically all AB molecules in the sample are bound to the AuNPs. An observed high-field shift (see Fig. 3.3, ESI†) of the aromatic proton signals with increasing AB surface concentration supports an irregular, statistical distribution of the azothiolate and alkylthiolate ligands in the mixed monolayer.

The UV/Vis spectra of the AB-functionalised NPs displayed in Fig. 3.2 show two pronounced absorptions, the broad local surface plasmon resonance (LSPR) band at around $\lambda = 515$ nm and the $\pi\pi^*$ band of the AB ligands in their *trans* form at $\lambda = 350$ nm. The weaker $n\pi^*$ AB band at around $\lambda = 455$ nm is only barely visible. Sizeable surface enhancement of the AB $\pi\pi^*$ absorption could be ruled out in our case by a combination of ^{1}H NMR and UV/Vis spectroscopy as detailed in the ESI.† Typical AB surface concentrations by both methods were found to be around ~ 100 molecules per NP. For photoswitching, the solutions were irradiated at either $\lambda = 365$ nm or at $\lambda = 455$ nm. The results obtained with the six different azothiolate-alkylthiolate combinations are given in Fig. 3.2. As can be seen, UV-induced *trans-cis* isomerisation leads to a drastic decrease of the intensity of the $\pi\pi^*$ band, which recovers upon back-isomerisation with visible light. The photostationary states PSS365 and PSS455 reached at the two wave-

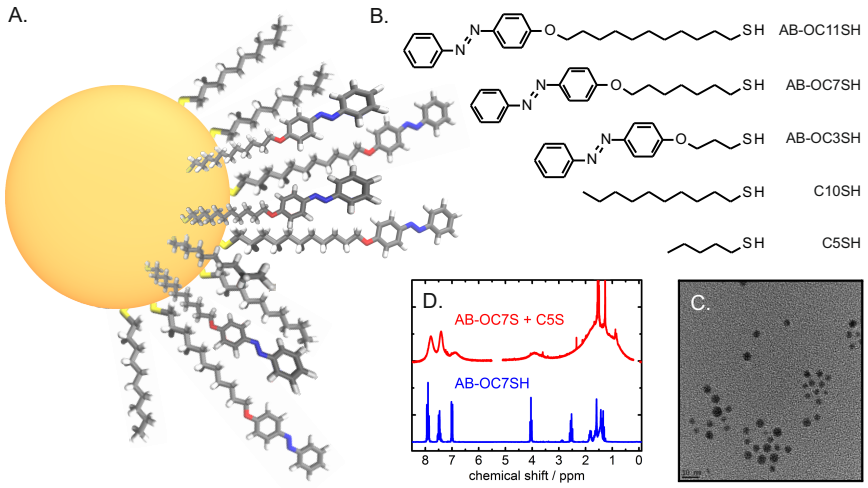

Figure 3.1: (A) Schematic representation of the functionalised AuNPs with azothiolate ligands and alkylthiolate coligands (NPs and ligands not drawn to scale). (B) Structural formulas and abbreviations of the different thiols used in this work. (C) Typical TEM image of the AB-functionalised AuNPs (scale bar: 10 nm). (D) Comparison of the ^{1}H NMR spectra of free AB-OC7SH in solution (blue) and AB-OC7S-/C5S-NPs (red). The lack of sharp ^{1}H signals of the AB-function in the NP spectrum confirms that the ligands are bound to the NPs (residual sharp lines in the NP spectrum belong to the solvent and a trace of H_2O).

lengths (for temporal evolutions see Section 3.2.3, ESI†) represent the switching of the ABs on the AuNPs to mostly the *cis* and mostly the *trans* forms, respectively. In contrast, with two exceptions (Fig. 3.2C and E, discussed below) little change was observed in the region of the LSPR bands. In all cases, between three and five switching cycles were performed without any noticeable signs of degradation or reduction in switching efficiencies of the samples, as evident by the near-perfect agreement between the measured spectra belonging to the respective photostationary states which are plotted on top of each other.

While this general behaviour is the same for all investigated samples, significant differences are revealed depending on the alkyl chain lengths of the ligands: in PSS365, the NPs with the shortest azoligand (AB-OC3S) still show significant residual 350 nm ($\pi\pi^*$) absorption by *trans*-AB, indicating that not all AB units were isomerised (see Fig. 3.2A and B). Assuming that the spectra of the ABs on the NPs are similar in shape to those in solution, we found switching efficiencies from the pure trans form at the start to 70% *cis*/30% *trans* in PSS365 and 10% *cis*/90% *trans* in PSS455 (for details see Section 3.2.3, ESI†). With longer azoligands, the *trans*-to-*cis* switching efficiency increased, while the *cis*-to-*trans* efficiency decreased. For the ligand-coligand combination with the longest alkyl spacer (AB-OC11S/C10S,

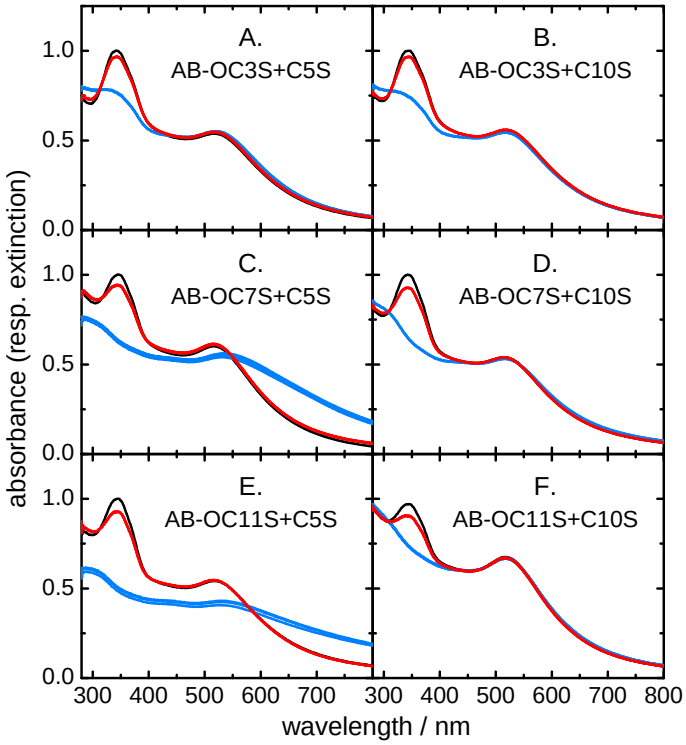

Figure 3.2: Measured UV/Vis spectra of the AB-functionalised AuNPs before irradiation (all-*trans*, black) and in PSS365 (blue) and PSS455 (red). All samples were prepared using equimolar azothiol-alkylthiol solutions and switched back and forth between the two photostationary states reproducibly at least 3 to 5 times, the individual spectra belonging to those switching cycles are plotted on top of each other. In panels A, B, D and F, only photoisomerisation of the AB moiety is observed. Panels C and E additionally show the reversible aggregation of the NPs in PSS365 demonstrated by the broadened LSPR bands; in this case the spectra show the overall extinction (sum of absorption plus possible light scattering).

Fig. 3.2F), we reached switching to 95% *cis*/5% *trans* in PSS365 and 25% *cis*/75% *trans* in PSS455.

Much more striking are the differences after irradiation in the shape of the LSPR bands when the longer azoligands are combined with short alkylthiolates (Fig. 3.2C and E), whereas little change is observed in all systems with decanethiolate coligands (Fig. 3.2B, D and F), a strong broadening and decrease in intensity of the LSPR band together with a sizeable red-shift are found after isomerisation of samples carrying ABs with long alkyl spacers (C7, C11) in combination with pentanethiolate coligands (Fig. 3.2C and E). This phenomenon indicates aggregation of the NPs after switching of the attached ABs to their *cis* form. As shown, it is completely reversible. Fig. 3.7 (ESI†) demonstrates that aggregation occurs whether the sample solutions are stirred or not.

The aggregation is attributed to the attractive dipole-dipole forces between the *cis*-ABs in the ligand shells around the NPs, when they come into close proximity by Brownian motion. The dipole moment of *cis*-AB (3.2 Debye) causes weaker solvent stabilisation of the NPs in nonpolar toluene such that they aggregate. Related mechanisms have been discussed for various NP systems in the literature.[12,14] In our case, longer alkylthiolate coligands appear to better shield the *cis*-ABs and to lead to better solvation, thereby preventing association. Fig. 3.8 (ESI†) shows that the aggregation tendency in a row of three AB-OC7S-/C5SAuNP samples increases with higher AB surface concentration. This effect is rationalised by the higher dipole density on the NPs. In addition, the coligand chain length seems to play a crucial role, as aggregation occurs only when it is shorter than the alkyl spacer length in the azoligand. Two arguments come to mind: first, the shorter chain length of the coligand allows for closer contact between the *cis*-switched NPs and thereby stronger interaction of the dipoles. Second, the *cis*-switched NPs with short alkylthiols are expected to be less well stabilised by the solvent so that their tendency for aggregation is raised compared to decanethiol-cofunctionalised NPs. The first hypothesis is supported by two facts: the AB-OC3S-functionalised NPs with a pentanethiolate coligand show practically no aggregation even after prolonged exposure to UV light, demonstrating that pentanethiol alone does not enable aggregation by lowering the solubility of the NPs. Further, the strength of aggregation seems to depend mainly on the surface concentration of AB on the NPs rather than on the absolute length difference between the ligands and coligands. This suggests that - at least in the present case - the solubility of the NPs is not the main driving force for the aggregation, whereas the dipole-dipole forces are. When the *cis*-ABs are isomerised back to *trans*, the aggregates are no longer favoured and disaggregate.

In conclusion, we studied AuNPs with mixed azothiolate-alkylthiolate monolayers. The samples could be photoswitched back and forth reproducibly between two photostationary states (mostly *cis* and mostly *trans*) without visible photodegradation after several cycles. Observed differences in switching efficiency indicate steric or electronic hindrance of the isomerisation when the alkyl spacer in the azoligand becomes too short. Furthermore, we observed a fully reversible aggregation of NPs switched to the *cis* state when a long azoligand was combined with a coligand possessing a shorter alkyl chain. Together with the finding that the tendency for aggregation depends on the *cis*-AB surface concentration, our results lead to the conclusion that dipole-dipole attraction is the main driving force for the observed aggregation. Another critical factor appears to be solubility, as we found that azothiolate-AuNPs without alkylthiolates were practically insoluble. Our approach using mixed monolayers offers control of the photoaggregation potential of functionalised AuNPs by opti-

mising the chain length of the coligand and the surface concentration of the azoligand. The photoswitching dynamics of our functionalised AuNPs are now under investigation using femtosecond time-resolved spectroscopy.

We gratefully acknowledge the support of this work by the Collaborative Research Centre 677 “Function by Switching”.

BIBLIOGRAPHY

[1] Thomas, K. G.; Kamat, P. V. *Acc. Chem. Res.* **2003**, *36*, 888–898.

[2] Link, S.; El-Sayed, M. A. *Annu. Rev. Phys. Chem.* **2003**, *54*, 331–366.

[3] Louis, C.; Pluchery, O. *Gold Nanoparticles for Physics, Chemistry and Biology*; Imperial College Press, London, 2012.

[4] Klajn, R.; Stoddart, J. F.; Grzybowski, B. A. *Chem. Soc. Rev.* **2010**, *39*, 2203–2237.

[5] Evans, S. D.; Johnson, S. R.; Ringsdorf, H.; Williams, L. M.; Wolf, H. *Langmuir* **1998**, *14*, 6436–6440.

[6] Wang, R.; Iyoda, T.; Jiang, L.; Tryk, D. A.; Hashimoto, K.; Fujishima, A. *J. Electroanal. Chem.* **1997**, *438*, 213–219.

[7] Zhang, J.; Whitesell, J. K.; Fox, M. A. *Chem. Mater.* **2001**, *13*, 2323–2331.

[8] Das, S.; Ranjan, P.; Maiti, P. S.; Singh, G.; Leitus, G.; Klajn, R. *Adv. Mater.* **2013**, *25*, 422–426.

[9] Wei, Y.; Han, S.; Kim, J.; Soh, S.; Grzybowski, B. A. *J. Am. Chem. Soc.* **2010**, *132*, 11018–11020.

[10] Lin, J.-Q.; Zhang, H.-W.; Chen, Z.; Zheng, Y.-G.; Zhang, Z.-Q.; Ye, H.-F. *J. Phys. Chem. C* **2011**, *115*, 18991–18998.

[11] Klajn, R.; Wesson, P. J.; Bishop, K. J. M.; Grzybowski, B. A. *Angew. Chem. Int. Ed.* **2009**, *48*, 7035 –7039.

[12] Klajn, R.; Bishop, K. J. M.; Grzybowski, B. A. *Proc. Nat. Acad. Sci. U. S. A.* **2007**, *104*, 10305–10309.

[13] Hostetler, M. J.; Wingate, J. E.; Zhong, C.-J.; Harris, J. E.; Vachet, R. W.; Clark, M. R.; Londono, J. D.; Green, S. J.; Stokes, J. J.; Wignall, G. D.; Glish, G. L.; Porter, M. D.; Evans, N. D.; Murray, R. W. *Langmuir* **1998**, *14*, 17–30.

[14] Bishop, K. J. M.; Wilmer, C. E.; Soh, S.; Grzybowski, B. A. *Small* **2009**, *5*, 1600–1630.

3.2.1 SYNTHESES

The functionalised gold nanoparticles (AuNPs) were synthesised in a two-step process starting from oleylamine-stabilised AuNPs followed by ligand exchange with the selected azothiol and respective alkylthiol. The oleylamine-stabilised AuNPs were obtained following a variant of the protocol described in Ref. 3.S1. The azoligands 4-(11-mercaptoundecanoxy)-azobenzene (AB-OC11SH), 4-(7-mercaptoheptanoxy)-azobenzene (AB-OC7SH) and 4-(3-mercaptopropanoxy)-azobenzene (AB-OC3SH) were synthesised via a slightly modified three-step procedure adopted from Klajn et al.[3.S2] The synthesis of AB-OC11SH is described as example below, the other azothiols were obtained accordingly.

The integrity and purity of all intermediate and final products was carefully checked by NMR spectroscopy. Contrary to occasional other reports, we did not observe reduction of the azobenzene groups in the presence of the thiol groups during our syntheses, but oxidation of the thiols to disulfides may occur. However, as disulfides also bind to Au surfaces (with dissociation of the disulfide bond), the presence of disulfides poses no serious problem for our syntheses. According to our NMR measurements, the oxidation is slow at room temperature and played no significant role within the time frame of our synthesis.

4-(Undec-10-enyloxy)-azobenzene

4-Hydroxyazobenzene (2.11 g, 10.7 mmol) and potassium *tert*-butoxide (1.25 g, 11.1 mmol) were placed in a three-neck round bottom flask equipped with a reflux condenser. The setup was purged with argon for 10 min, followed by the addition of 25 mL of dry DMF. The mixture was stirred at room temperature until the solid reactants had dissolved. Next, 11-bromo-1-undecene (2.50 mL, 11.1 mmol) was added and the mixture was heated to reflux for 25 min, during which the colour of the solution changed to bright red and a colourless precipitate formed. The reaction was monitored by TLC (silica gel, hexane/ethyl acetate (20:1)). After cooling down to room temperature the reaction mixture was poured into 100 mL of deionized water and the aqueous solution was extracted with *n*-hexane (4×50 mL). The combined hexane fractions were washed with water (4×50 mL) and dried over magnesium sulfate. The solvent was evaporated under reduced pressure to yield an orange solid, which was recrystallized from ethanol. The product was obtained as an orange crystalline solid (2.42 g, 65 %).

^{1}H-NMR (200 MHz, $CDCl_3$): δ = 7.95-7.83 (m, 4H, Ar-H), 7.54-7.40 (m, 3H, Ar-H), 7.04-6.96 (m, 2H, Ar-H), 5.82 (ddt, ^3J = 16.9 Hz,^3J = 10.1

Hz, $^3J = 6.6$ Hz, 1H, C*H*=CH_2), 5.05-4.89 (m, 2H, =CH_2), 4.04 (t, ^3J = 6.5 Hz, 2H, -O-CH_2), 2.05 (m, 2H, 1.82 (m, 2H), 1.55-1.27 (m, 12H) ppm.

4-(11-Thioacetoxyundecanoxy)-azobenzene

4-(Undec-10-enyloxy)-azobenzene (1.01 g, 2.87 mmol) and azobisisobutyronitrile (141 mg, 0.86 mmol) were placed in a three-neck round bottom flask equipped with a reflux condenser. The flask was purged with argon for 25 min followed by the addition of 20 mL of dry toluene and thioacetic acid (810 µL, 11.44 mmol) while stirring. The reaction mixture was refluxed for 2 h, after which the reaction mixture was cooled down to room temperature. The mixture was then poured into a separatory funnel containing 100 mL of saturated sodium hydrogen carbonate solution and 50 mL of toluene. The organic phase was separated and washed with 50 mL saturated sodium hydrogen carbonate solution, followed by washing with deionized water (5 × 50 mL). The solution was dried over magnesium sulfate and the solvent was evaporated under reduced pressure. The obtained orange solid was recrystallized from methanol. The product was obtained as an orange crystalline solid (974 mg, 80 %).

^{1}H-NMR (200 MHz, $CDCl_3$): δ = 7.95-7.83 (m, 4H, Ar-H), 7.54-7.39 (m, 3H, Ar-H), 7.04-6.96 (m, 2H, Ar-H), 4.04 (t, $^3J = 6.5$ Hz, 2H, -O-CH_2), 2.92-2.79 (m, 2H), 2.32 (s, 3H, CH_3), 1.90-1.74 (m, 2H), 1.65-1.25 (m, 16H) ppm.

4-(11-Mercaptoundecanoxy)-azobenzene (AB-OC11SH)

4-(11-Thioacetoxyundecanoxy)-azobenzene (950 mg, 2.30 mmol) was placed in a three-neck round bottom flask, which was purged with argon for 20 min. Then 20 mL of degassed methanol and 5 mL of a 1M solution of HCl in methanol were added. The reaction mixture was heated to reflux for 6 h after which the reaction mixture was cooled to room temperature. The precipitate which had formed during the reaction was filtered off, washed with a small amount of cold methanol and dried in vacuo. The procedure yielded a yellow powdery solid (805 mg, 94 %).

^{1}H-NMR (500 MHz, $CDCl_3$): δ = 7.93-7.86 (m, 4H, Ar-H), 7.52-7.41 (m, 3H, Ar-H), 7.02-6.98 (m, 2H, Ar-H), 4.04 (t, $^3J = 6.6$ Hz, 2H, -O-CH_2), 2.52 (dd, $^3J = 14.7$ Hz, $^3J = 7.4$ Hz, 2H, -CH_2-SH), 1.86-1.78 (m, 2H, -O-CH_2-CH_2), 1.61 (dt, $^3J = 14.8$ Hz, $^3J = 7.3$ Hz, 2H, -CH_2 -CH_2-SH), 1.52-1.44 (m, 2H), 1.42-1.25 (m, 12H), 1.33 (t, $^3J = 7.5$ Hz, 1H, -SH) ppm.

Oleylamine-stabilised AuNPs

Hydrogen tetrachloroaurate trihydrate (200 mg, 0.51 mmol) was dissolved in a mixture of 2.00 mL of toluene and 2.00 mL of freshly distilled oleylamine. This solution was poured into a mixture of 15.0 mL of toluene and 4.00 mL of oleylamine in a 100 mL round bottom flask. 2.00 mL of methanol were added to the solution. Next, sodium borohydride (41.0 mg, 1.08 mmol) was added to the mixture at once while stirring. Immediately after addition of sodium borohydride the reaction mixture turned dark. It was stirred vigorously at room temperature for 2 - 2.5 h. Next the reaction mixture was poured into 35 mL of acetonitrile resulting in a dark precipitate. The precipitate was washed first with acetonitrile (3×20 mL), and then with methanol (3×20 mL). The particles were then redissolved and used without further characterization for the ligand exchange reaction. The above procedure usually yielded $\approx$ 100 mg of oleylamine-coated AuNPs.

Ligand exchange

To exchange the oleylamine against thiol ligands a known amount of oleylamine-coated AuNPs was dissolved in toluene yielding a solution with concentration of approximately 2.5 mg/mL. The solution was then degassed with Ar for 20 min. Next, a two-fold excess of a mixture of the azothiol ligand and the alkylthiol coligand dissolved in degassed toluene was added at once. The required amounts of thiol for the ligand exchange were estimated before the reaction from the NP diameter determined by the TEM measurements and the resulting surface area assuming a value for the thiol surface footprint on the NPs of $F_{\text{thiol}} = 22$ Å^2/molecule.[3,S3] The azothiol mole fractions in the ligand exchange mixtures were between $x_{AB} = 0.3 - 0.7$ (mostly mixtures with $x_{AB} = 0.5$ were used). The total amount of toluene was chosen such that the final AuNP concentration was $\approx$ 2 mg/mL. The reaction mixture was kept under Ar atmosphere and was stirred at room temperature in the dark for $\approx$ 20 h. The NPs were then precipitated by addition of methanol and washed five times with a mixture of methanol and toluene (4:1). For the shorter chain lengths (AB-OC7SH and AB-OC3SH), the reaction mixtures were concentrated under vacuum before precipitation to reduce the necessary amount of methanol. The cleaned NPs were then dissolved in toluene.

Materials

Oleylamine (Aldrich) was distilled under reduced pressure and stored under Ar atmosphere before use. $HAuCl_4 \cdot 3\ H_2O$ (Aldrich), $NaBH_4$ (Fluka), pentanethiol (Aldrich) and decanethiol (Aldrich) were used as purchased. All solvents were distilled under reduced pressure before use.

Methods

For TEM imaging, performed at the Institute of Materials Science of Christian-Albrechts-University Kiel, toluene solutions of the AuNPs were drop-casted onto holey carbon grids and images were recorded at several acceleration voltages between 75 and 390 kV.

NMR spectra of the free azothiols and the AB-functionalised AuNPs were recorded on a Bruker DRX 500 or a Bruker AV 600 FT spectrometer in deuterated solvents.

UV/Vis absorption spectra were recorded on a Shimadzu UV-2401 PC desktop spectrometer in fused silica cuvettes with 1 mm optical path length. Each spectrum was referenced to that of the pure solvent.

NMR spectra at different AB surface coverages

The measured NMR spectra of AB-OC11S-/C10S-functionalised AuNPs prepared with different azothiol mole fractions are shown in Fig. 3.3. The spectrum of the free azoligand in solution serves as reference. The strong broadening of the ^{1}H resonances on the AuNPs is immediately evident. The observed high-field shift of the aromatic proton signals with increasing AB surface concentration supports an irregular, statistical distribution of the azothiolate and alkylthiolate ligands in the monolayer.

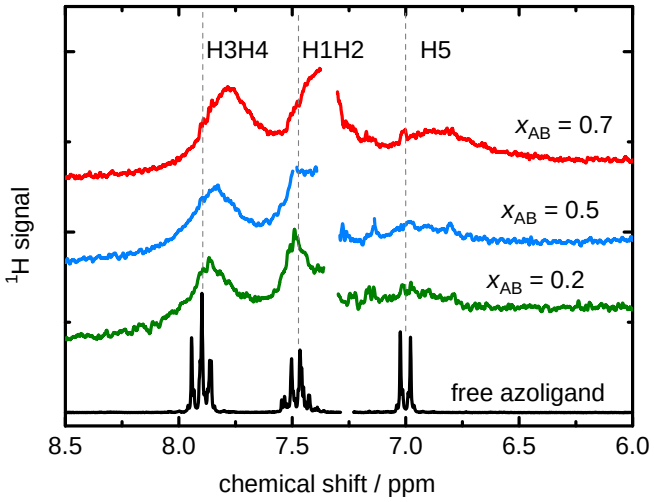

Figure 3.3: ^{1}H NMR spectra in CD_2Cl_2 of AB-OC11S-/C10S-functionalised AuNPs prepared with different azothiol mole fractions. The spectrum at the bottom shows the positions of the aromatic ^{1}H signals of free AB-OC11SH in solution (see Section 3.2.1 for precise chemical shift values and assignments). The gap in the spectra around 7.3 ppm is due to a trace of chloroform which was cut out.

Estimation of the AB surface coverage of the NPs from the UV/Vis spectra

The concentration (in mol/L) of the NPs in solution was estimated from the measured absorbance at the center of the LSPR band taking the empirical value for the decadic molar absorption coefficient of the AuNPs of

$$\epsilon_{NP} = 4.2 \times 10^4 \times d^{3.4} \text{ L mol}^{-1} \text{ cm}^{-1}$$

with the particle diameter d in nm.[3.S4-3.S7] The number of Au atoms per NP is simply given by

$$N = \frac{\pi}{6} \frac{\rho_{Au} N_A}{M_{Au}} d^3$$

where $\rho_{Au} = 19.3$ g/mol is the macroscopic density of gold, $M_{Au} = 197$ g/mol is the molar weight, N_A is Avogadro's number, and d the nanoparticle diameter. For the AuNPs with d~ 4 nm ($N \sim 2000$) studied in the present work, the molar absorption coefficient thus becomes

$$\epsilon_{NP} = 4.58 \times 10^6 \text{ L mol}^{-1} \text{ cm}^{-1}$$

which corresponds to a value of $\epsilon_{1Au} = 2.29 \times 10^3$ L mol^{-1} cm^{-1} per Au atom. Considering the very small size of the investigated well-defined AuNPs of interest here, light scattering can be neglected compared to absorption under the applied experimental conditions as long as there is no aggregation, but scattering may contribute to the extinction (sum of absorption plus scattering) in the case of photo-induced aggregation below.

The concentration of attached azothiolate ligands on the AuNPs was derived after subtraction of the absorbance by the AuNPs themselves from the measured absorbance in the $\pi\pi^*$ band at $\lambda = 345$ nm using the independently determined value for the molar absorption coefficient of the free AB ligands in solution of $\epsilon_{AB} = 26200$ L mol^{-1} cm^{-1}. Note that we assume here that the AB absorption coefficient on the AuNPs is not substantially altered by surface enhancement effects (as confirmed below, cf. Section 3.2.2).

A set of UV/Vis spectra illustrating the procedure is given in Fig. 3.4. Taking the experimental absorbance values for the example shown and the given absorption coefficients, we find an azothiolate surface coverage of ~ 125 molecules/AuNP. With the AuNP surface area of ~ 5000 Å^2/NP and the assumption of similar sticking probabilities for AB-OC7S- and C10S-ligands ($x_{AB} = 0.5$), this result corresponds to a surface footprint of ~ 20 Å^2/molecule in satisfactory agreement with accepted values.[3.S3]

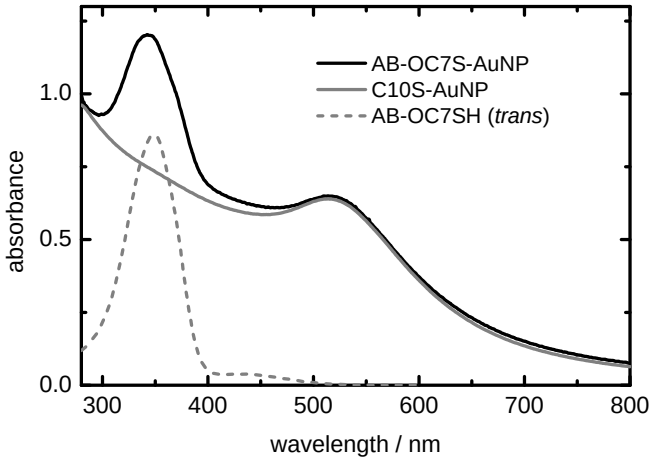

Figure 3.4: UV/Vis absorption spectra of AB-OC7S-/C10S-functionalised AuNPs (solid black line) prepared using an equimolar solution (i.e. $x_{AB} = 0.5$) of AB-OC7SH and C10SH for the ligand exchange and C10S-functionalised AuNPs (solid grey line) in toluene at 1 mm optical pathlength. For comparison, the dashed grey line shows the absorption spectrum of free AB-OC11SH ($c = 3.2 \times 10^{-4}$ mol L^{-1}) in toluene. Light scattering can be neglected for the measured AuNPs here due to their small size.

Estimation of the AB surface coverage on the NPs from NMR spectra

As surface enhancement effects may lead to an overestimation of the concentration of attached ligands from the UV/Vis absorption spectra, we used ^{1}H NMR spectroscopy as an independent alternative method to determine the AB concentration (Fig. 3.5). For these measurements, ethylene glycol (EG) was added to the sample as a standard of known concentration. Comparison of the integral of the EG signal at 3.66 ppm with the integral of the aromatic AB proton signals yielded the AB concentration in the sample. For identical concentrations of EG and AB ligand in the sample solution, the ratio of both integrals should be 9H/4H. As the measured integral corresponds to 16 protons, we find the concentration of AuNP-attached ABs to be 1.78 times the EG concentration of $c_{EG} = 0.89 \times 10^{-3}$ mol L^{-1}, which gives $c_{AB}(NMR) = 1.58 \times 10^{-3}$ mol L^{-1}.

From the UV/Vis absorption spectrum of the same sample solution, an AB concentration of $c_{AB}(UV/Vis) = 1.38 \times 10^{-3}$ mol/L was calculated. Within the estimated error limits of 25 % on both values, the AB concentrations obtained via ^{1}H NMR and via UV/Vis spectroscopy are thus seen to match well, indicating that - at least in the present case - there is no large change of the $\pi\pi^*$ band absorption strength of the AB ligands by surface enhancement effects on attachment of the ligands to the AuNPs.

Taking the AuNP concentration of $c_{NP} = 1.62 \times 10^{-5}$ mol L^{-1} in the same solution derived by UV/Vis spectroscopy (cf. Section 3.2.2), we calculate an azothiolate surface coverage of ~ 97 molecules/ AuNP

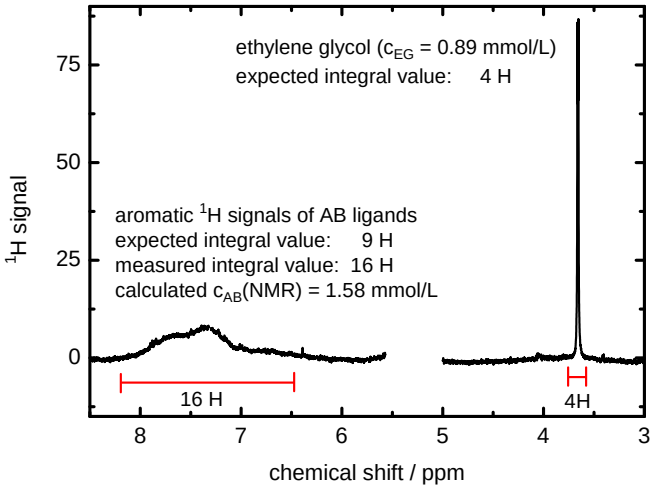

Figure 3.5: ^{1}H NMR spectrum (baseline corrected) of AB-OC7S/C10S-AuNPs with ethylene glycol at $c_{EG} = 0.89$ mmol/L added as concentration standard. As the integral of the AB signal is $16/9 = 1.78$ times larger than expected for equal concentrations of AB and ethylene glycol, the AB concentration is estimated to be c_{AB}(NMR) = 1.58 mmol/L.

from the NMR data compared to ~ 85 molecules/AuNP from the UV/Vis data. The latter value is a bit lower than the one for AB-OC11S-ligands determined in Section 3.2.2 above, reflecting unavoidable variations in the synthesis yields and a possible weak dependence on alkyl spacer chain lengths.

3.2.3 PHOTOSWITCHING

For the photoswitching experiments, the AB-functionalized AuNPs in solution in toluene were irradiated using two light emitting diodes with emission maxima at $\lambda = 365$ nm (NCSU033A, 400 mW) and $\lambda = 455$ nm (NS4C107E, 400 mW), respectively. All measurements were performed at room temperature.

Photoswitching behaviour of non-aggregating AB-AuNPs

Photoswitching experiments were carried out with light at $\lambda = 365$ nm and $\lambda = 455$ nm to drive the AB-functionalised NPs from the *trans* to the *cis* and from the *cis* to the *trans* states, respectively. The measured behaviour of a typical sample of AB-OC7S-/C10S-functionalised AuNPs is illustrated in Fig. 3.6. The UV/Vis spectra after selected times of UV or Vis irradiation and in the respective photostationary states (PSS365 and PSS455) are displayed in panels A and B, while panels C and D show plots of the absorbance values at $\lambda = 345$ nm in the $\pi\pi^*$ absorption band against irradiation time. As can be seen, the PSS365 (*trans-cis* isomerisation) is approached quite rapidly, similar

to the case for the *trans-cis* photoisomerisation of the free azothiols in solution. The PSS455 (*cis-trans* isomerisation) takes longer to reach due to the much weaker absorption at the latter wavelength in the $n\pi^*$ band. The photo-induced isomerisation at 455 nm also appears to be slower because most of the incident light is absorbed by the AuNPs themselves rather than by the AB ligands. The observed half-times for approach to the photostationary states are ~ 20 s (PSS365) and ~ 60 s (PSS455). To ensure that the photostationary states were really reached within experimental errors, and to rule out slower secondary photo-induced processes, however, the experiments were usually continued for longer times (up to 20 - 30 min) until the measured absorbances remained constant. Control measurements with 60 min irradiation times revealed no further change.

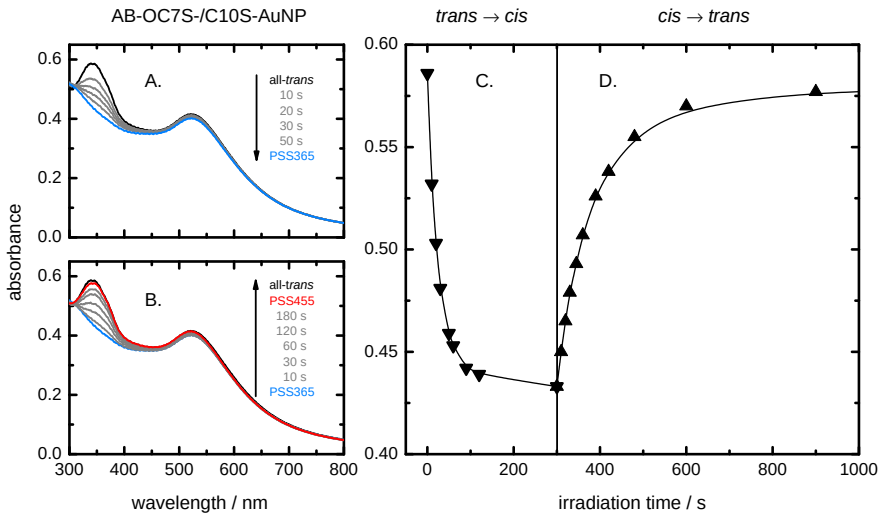

Figure 3.6: Photoswitching behaviour of AB-OC7S-/C10S-functionalised AuNPs. A: UV/Vis spectra during irradiation at 365 nm (*trans-cis* isomerisation). B: UV/Vis spectra during irradiation at 455 nm (*cis-trans* isomerisation). C and D: Absorbance values at the maximum of the $\pi\pi^*$ absorption band plotted against irradiation time.

Photoswitching behaviour of aggregating AB-AuNPs

As revealed by Fig. 3.2 in the main paper, AB-functionalised AuNPs with short alkylthiolate coligands exhibit photoreversible aggregation when the AB is switched to the *cis* state. In this case, the measured UV/Vis spectra show the overall extinction resulting from absorption and a possible contribution from light scattering. The behaviour of a typical aggregating sample is shown in Figs. 3.7 A and B for unstirred and in Figs. 3.7 C and D for stirred conditions. It is apparent that aggregation occurs and is fully photoreversible in both cases. However, the aggregation process seems to be slower in the stirred than in the unstirred case. At a given concentration, stirring should

rather facilitate aggregation than prevent it. In the present case, however, the measurement under stirred condition has been performed at ten-fold lower concentration in a cuvette with 10 mm pathlength than the measurement under unstirred conditions. Thus, the slower aggregation in the stirred case is fully expected on the grounds of the lower concentration.

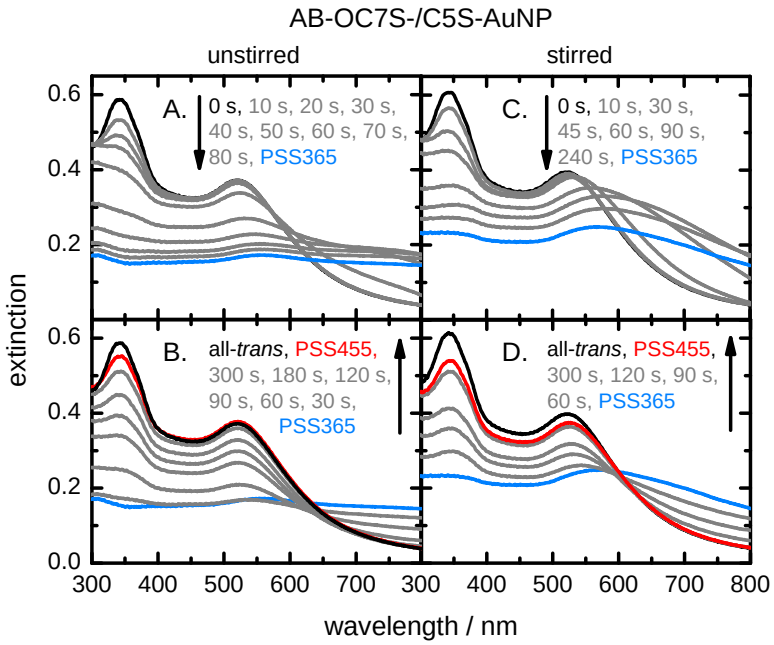

Figure 3.7: Photoswitching behaviour of AB-OC7S-/C5S-functionalised AuNPs under unstirred conditions (A, B) and stirred conditions (C, D). A and C: extinction spectra during irradiation at 365 nm (*trans-cis* isomerisation); B and D: extinction spectra during irradiation at 455 nm (*cis-trans* isomerisation). The stirred measurements were performed at a ten-fold lower concentration in a 10 mm cuvette compared to the unstirred measurements performed in a 1 mm cuvette.

Increasing aggregation potential with higher AB surface coverage

Measured UV/Vis extinction spectra (absorption plus possible small contribution from scattering) of AB-OC7S/C5S-functionalised AuNPs with increasing number of attached azothiols (N_{AB}) from different syntheses are given in Fig. 3.8. An increasing strong broadening of the LSPR absorption feature indicating stronger aggregation with higher azothiol surface concentration from left to right is immediately recognisable.

Estimation of the trans/cis compositions in the photostationary states

In order to determine the *trans/cis* compositions in the photostationary states PSS365 and PSS455, the measured UV/Vis spectra of the

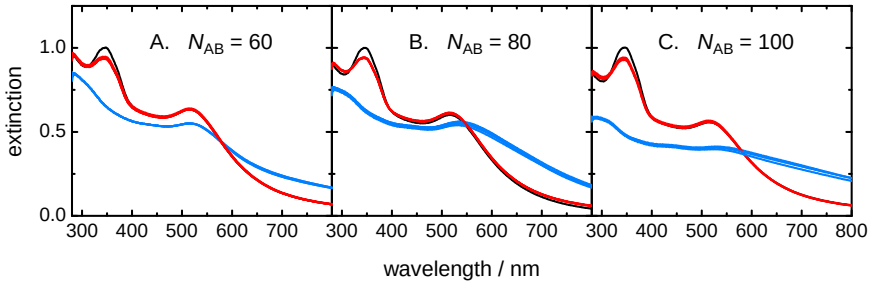

Figure 3.8: UV/Vis extinction spectra of AB-OC7S/C5S-functionalised Au-NPs with increasing number of attached azothiols (N_{AB}) from different syntheses. Spectra before irradiation (all-*trans*): black; in PSS365 (ABs mostly in *cis* form): blue; in PSS455 (ABs mostly back in *trans* form): red. Each panel shows the recorded spectra taken during 3 - 5 photoisomerisation cycles plotted on top of each other to point out that the samples can be switched back and forth between the two photostationary states reversibly and highly reproducibly.

respective AB-AuNPs were modeled by the sum of the spectra of the alkylthiolate NPs and the spectra of *trans*-AB and *cis*-AB NPs according to

$$A_{\text{AB-AuNP}} = A_{\text{alkylS-AuNP}} + x_{trans} \times A_{trans} + (1 - x_{trans}) \times A_{cis}$$

using the molar fraction x_{trans} as adjustable fit parameter. The required spectrum of the free *cis*-AB thiol was derived from the spectrum in the PSS365 (mostly *cis*-AB) and the spectrum of the free *trans*-AB taking a value for the *trans/cis* ratio in the PSS365 derived by ^{1}H NMR spectroscopy.

The evaluation of the *trans/cis* ratios in the photostationary states is illustrated by Fig. 3.9. For the example shown, the results are

$$x_{trans} = 0.05 \pm 0.02,\ x_{cis} = 0.95 \pm 0.02 \text{ in PSS365}$$

and

$$x_{trans} = 0.80 \pm 0.05,\ x_{cis} = 0.20 \pm 0.05 \text{ in PSS455.}$$

3.2.4 THERMAL LIFETIMES FOR CIS-AB LIGANDS ON AUNPS

The thermal lifetimes of the *cis*-azothiols in solution and the *cis*-azothiolate ligands on the AuNPs at room temperature are compiled in Table 3.1. As shown, the lifetimes of *cis*-ABs are not significantly altered on the AuNPs compared to AB in solution in case of the two longer ligand chains. For the shortest linker chain (AB-OC3SH) the *cis*-lifetime is reduced to half its value upon attachment to the AuNP.

	$\tau_{\text{free AB}}$ / h	$\tau_{\text{AB-AuNP}}$ / h
AB-OC3SH	28	14
AB-OC7SH	19	17
AB-OC11SH	35	43

Table 3.1: Thermal lifetimes of the investigated *cis*-AB ligands in solution and on the AuNP surface.

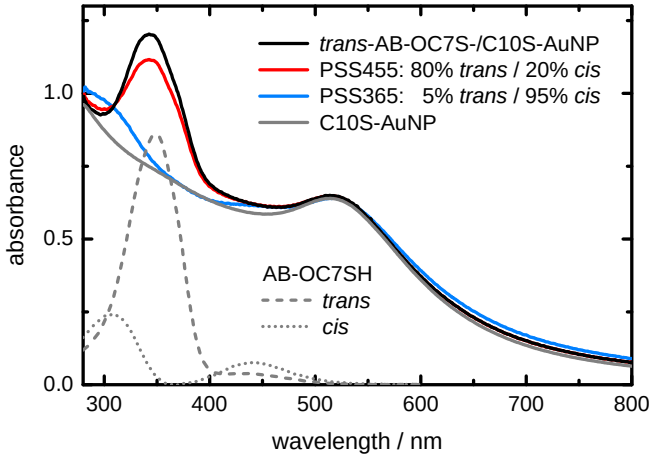

Figure 3.9: UV/Vis spectra of AB-OC7S/C10S-functionalised AuNPs before irradiation (solid black line), in the PSS365 (solid blue line), in the PSS455 (solid red line) and UV/Vis spectra of decanethiolate-functionalised NPs (C10S-AuNPs, solid grey line). The dashed and dotted grey lines (bottom left) show the spectra of free *trans*-AB-OC7SH and *cis*-AB-OC7SH in solution, respectively.

REFERENCES

3.S1. Malicki, M.; Hales, J. M.; Rumi, M.; Barlow, S. R.; McClary, L.; Marder, S. R.; Perry, J. W. *Phys. Chem. Chem. Phys.* **2010**, *12*, 6267.

3.S2. Klajn, R.; Wesson, P. J.; Bishop, K. J. M.; Grzybowski, B. A. *Angew. Chem. Int. Ed.* **2009**, *48*, 7035.

3.S3. Schreiber, F. *Prog. Surf. Sci.* **2000**, *65*, 151.

3.S4. Link, S.; El-Sayed, M. A. *J. Phys. Chem. B* **1999**, *103*, 8410.

3.S5. Jain, P. K.; Lee, K. S.; El-Sayed, I. H.; El-Sayed, M. A. *J. Phys. Chem. B* **2006**, *110*, 7238.

3.S6. Liu, X.; Atwater, M.; Wang, J.; Huo, Q. *Colloid. Surface. B* **2007**, *58*, 3.

3.S7. Rance, G. A.; Marsh, D. H.; Khlobystov, A. N. *Chem. Phys. Lett.* **2008**, *460*, 230.

4

FEMTOSECOND TIME-RESOLVED DYNAMICS OF *TRANS*-AZOBENZENE ON GOLD NANOPARTICLES

Anja Köhntopp, Mark Dittner and Friedrich Temps*

Institut für Physikalische Chemie, Christian-Albrechts-Universität zu Kiel, Olshausenstr. 40, 24098 Kiel, Germany

to be submitted to J. Phys. Chem. Lett.

OWN CONTRIBUTIONS TO THIS MANUSCRIPT:

- Synthesis and characterization of functionalized gold nanoparticles
- Time-resolved absorption spectroscopy
- Analysis of the data
- Writing of the manuscript

* To whom correspondence should be addressed. E-mail: temps@phc.uni-kiel.de

ABSTRACT

We report a direct femtosecond time-resolved transient absorption study of the photo-induced ultrafast dynamics of *trans*-azobenzene (AB) on gold nanoparticles (AuNPs) functionalized with a mixed self-assembled monolayer (mSAM) of an AB-alkylthiol and *n*-decanethiol. The observed spectro-temporal maps of the change in optical density following excitation at $\lambda = 357$ nm were analyzed by using temperature-dependent Mie theory and by Lorentzian band fitting to disentangle the ultrafast relaxation of the local surface plasmon resonance (LSPR) excitation of the Au core and the electronic deactivation and isomerization of the attached AB ligands. The results reveal a virtual absence of strong coupling between the AB chromophore and Au core. Very similar cooling dynamics of the LSPR excitation were observed in the AB-functionalized AuNPs compared to plain decanethiol-functionalized AuNPs. The excited-state dynamics associated with the AB chromophore were substantially slower than the LSPR relaxation. Separate fits to the transient AB signal yielded lifetime constants of $\tau_1 = 1.2 \pm 0.2$ ps and $\tau_2 = 4.7 \pm 1.1$ ps. Both results indicate surprisingly little differences in the electronic deactivation and isomerization dynamics of the AB ligand on the Au surface vs. in solution, despite the near resonance in energy between the $n\pi^*$ excited state of the AB and the AuNP LSPR band, and highlight the extraordinarily efficient electronic decoupling of the azo chromophore and Au core by the alkyl linker chain in the functionalized NPs.

4.1 RESULTS AND DISCUSSION

Materials with light-responsive surfaces consisting of thin layers of photochromic molecular switches which can be reversibly interconverted by irradiation at different wavelengths between two isomeric states with distinct chemical, optical, electrical or magnetical properties attract huge interest in fundamental and applied sciences alike. Potential applications range from smart interfaces, sensor technology, nanoelectronics and information storage via photocatalysis and solar energy conversion to medical diagnostics and therapy.[1,2] Azobenzenes (ABs) arguably constitute the most commonly used photoswitches which are employed to such ends.[3–5] For ABs directly adsorbed on a metal surface, however, the photoisomerization is strongly reduced by substrate-induced quenching. Surface-specific changes of electronic structure, energy or charge transfer processes between chromophore and metal, as well as steric hindrance are frequently discussed as major negative factors.[6–10] Strategies to overcome those obstacles have therefore moved to the forefront of active research. Photoswitching can be partially restored, for example, by modification of the AB with bulky tetra-*tert*-butyl substituents.[6,7] A flexible alter-

native approach to surface functionalization employs self-assembled monolayers (SAMs), in which the AB units are spatially separated and electronially decoupled from the metal by alkyl chains as linkers between chromophore and substrate. Photoswitchable SAMs of ω-AB-alkylthiols on Au(111) have been successfully studied by several means.[11–15] In densely packed layers on planar surfaces, large-amplitude structural isomerization is sterically hindered,[13,16] and excitonic coupling among neighboring AB chromophores in the surface layer may modify the optical properties and adversely affect the isomerization yields as well.[8,17,18] To avoid those effects, it has been found advantageous to ``dilute'' the AB switches in mixed azoalkylthiolate/alkylthiolate SAMs (mSAMs),[13,18] or to mount them on platforms to decouple the photochromes from the substrate.[16] Efficient switching has been achieved using both options, but a quantitative perception of the distinct isomerization rates and yields on metal surfaces is still far away. The difficulty of real-time measurements of ultrafast photoreactions on metals poses a major challenge in this context.

With the aim to develop a better understanding of the different factors influencing the photoswitching of azobenzenes on functionalized metal surfaces, this Letter reports first results of a direct time-resolved investigation of the photo-induced dynamics of *trans*-AB in azoalkylthiolate/alkylthiolate mSAMs on gold nanoparticles (Au-NPs) by femtosecond transient absorption spectroscopy. Helped by the fact that the surface curvature creates distance between the chromophore units, these AB-AuNPs show excellent photoswitching yields.[18–23] Moreover, they offer the huge advantage that their dynamics can be interrogated in a straightforward manner by a high sensitivity femtosecond pump–probe spectrometer in colloidal solution in a conventional liquid flow cell.[24,25] The evaluation of the obtained experimental data builds on the available extensive body of experimental and theory work on the dynamics of free AB in solution.[26–30] Parallel to the photo-induced dynamics associated with the AB chromophore, we account for the ultrafast relaxation of the local surface plasmon resonance (LSPR) excitation of the AuNPs[31–34] using the temperature-dependent Mie theory model as forwarded by Aruda et al.[35] The excited-state absorption (ESA) signals of the AB ligands on our AuNPs encoded in the recorded spectro-temporal maps of the change (difference) in optical density after UV photoexcitation are disentangled from the excited LSPR signals in the transient spectra by Lorentzian band fitting. Together, the results underline the efficient decoupling of the AB chromophore and Au core by the alkyl linker in the investigated AB-AuNPs as essential factor for the photoswitching process.

To produce the desired thiolated AuNPs we used amine-stablized AuNPs synthesized through reduction of $HAuCl_4 \cdot 3H_2O$ with $NaBH_4$

in the presence of oleylamine in a ligand exchange procedure with either pure decanethiol ($C_{10}H_{21}SH$) or a 1 : 1 mixture of decanethiol with the selected azoalkylthiol (AB-$OC_{11}H_{22}SH$). The two samples are referred to in the following as C10S-AuNPs and AB-OC11S-AuNPs (or AB-AuNPs for short), respectively. The associated static UV/Vis absorption spectra are given in Fig. 4.1A. With core diameters of $d \sim 4.0 \pm 0.8$ nm, our AB-AuNPs consist of the order of ~ 2000 Au atoms and carry $\sim 85 - 90$ azoalkylthiol and a similar number of alkylthiol molecules as ligands. A detailed description of the syntheses, the employed spectroscopic characterization procedures and the general photoswitching behavior can be found in an earlier publication.[23] Results of a separate time-resolved measurement demonstrating the ultrafast electronic deactivation and isomerization of the free azoligand molecules in solution after 357 nm excitation are given in Fig. 4.5 in the Supporting Information (SI) for reference.

Our setup for femtosecond time-resolved transient absorption measurements has also been described previously.[24] All samples were measured in solution in toluene in a flow cell with 1 mm optical pathlength. The applied $\lambda = 357$ nm excitation pulses were provided by a home-built non-collinear optical parametric amplifier equipped with a prism pulse compressor and a frequency doubling crystal. White-light pulses for broadband detection were generated in a CaF_2 plate, split into probe and reference beam, sent through a prism spectrograph and detected using fast frame-transfer CCD cameras. Both AuNP samples used in back-to-back experiments had similar concentrations (cf. Fig. 4.1A) and came from the same batch of aminated AuNPs to ensure the same particle size distribution.

The measured transient difference absorption spectra of the decanethiolate-functionalized AuNPs and the AB-OC11SH/C10SH-functionalized AuNPs after photoexcitation at $\lambda = 357$ nm are depicted in Fig. 4.1 B and C. At the employed pump wavelength, both the AuNP core and the $\pi\pi^*$ band of the AB ligands are excited at a ratio of roughly ~ 68 to 32 % (see Fig. 4.1A), respectively, if coupling between the core and ligands can be neglected.[23] As can be seen, the transient difference spectra of both AuNP samples show three prominent features: A strong transient bleach observed at the center wavelength of the LSPR band is accompanied by two positive transients to the blue and red. This characteristic spectral shape with negative center and positive wings in the transient difference spectra is well understood in principle as a consequence of the strong broadening of the AuNP LSPR absorption band upon photoexcitation,[36] whereby the intensity is redistributed by the sudden jump of the Au electron temperature from the band center into the wings. The explanation of the observed transient AuNP difference spectra thus differs from the normal case of ground-state bleach (GSB) and excited-state absorption

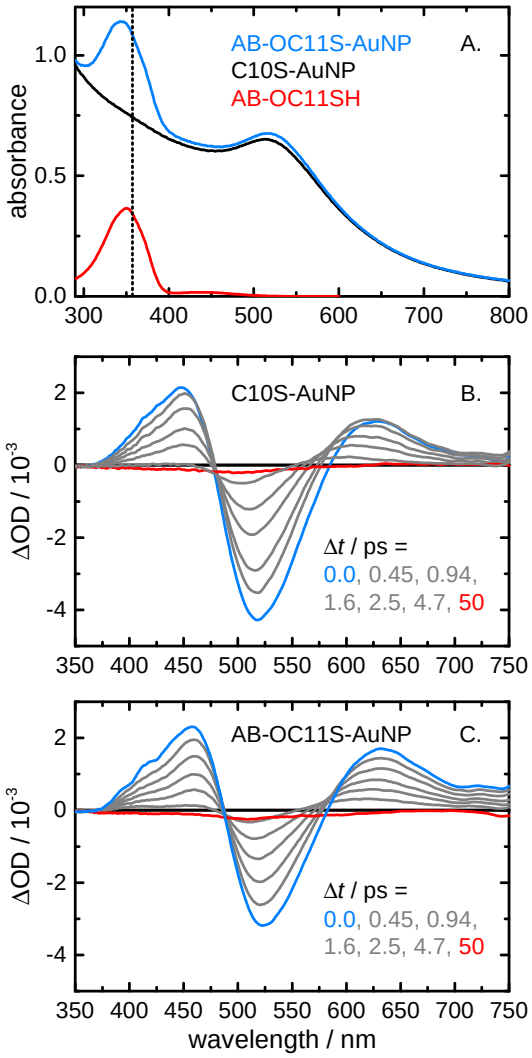

Figure 4.1: A: Static UV/Vis absorption spectra of the investigated C10S-AuNPs (black), AB-OC11S-AuNPs (blue) and free AB-OC11SH (red) in solution in toluene at 1 mm optical pathlength. The 357 nm excitation wavelength used in the femtosecond time-resolved experiments is marked by the dotted black line. The free AB-OC11SH spectrum has been scaled to match the difference between the AB-OC11S-AuNP and C10S-AuNP spectra. B and C: Measured transient difference absorption spectra of the investigated C10S-AuNP and AB-OC11S-AuNP samples, respectively, at selected pump-probe delay times after excitation at $\lambda = 357$ nm.

(ESA) features of photoexcited azobenzene or other molecular chromophores.

On comparison, the spectra for the two AuNP samples in Fig. 4.1 B and C display small, but important differences. First, the AB-AuNPs exhibit a weaker central LSPR bleach, whereas the absorptions to the blue and red are of similar intensity for both samples. Second, although direct ESA signatures by the azoligands are barely visible at

first glance, the closer analysis in the following clearly uncovers their contributions.

The transient spectral features associated with the LSPR excitations in Figs. 4.1B and 4.1C were first evaluated using the temperature-dependent Mie theory fitting model of Aruda et al.[35] The essentials of the model and its application are described in the SI (Section 4.2.2). The fits to our transient difference spectra are displayed in panels A and B of Fig. 4.2. As can be seen, the center bleach signals are well described, but the positive wings cannot be modeled as accurately.[35] The electron temperatures T_e provided by the fits are plotted as function of time after excitation for both AuNP systems in Figs. 4.2C and D. The observed decay curves thus visualize the ensuing ultrafast electron cooling dynamics, which we assume to proceed by electron-phonon (e–ph) scattering:[31,34,35]

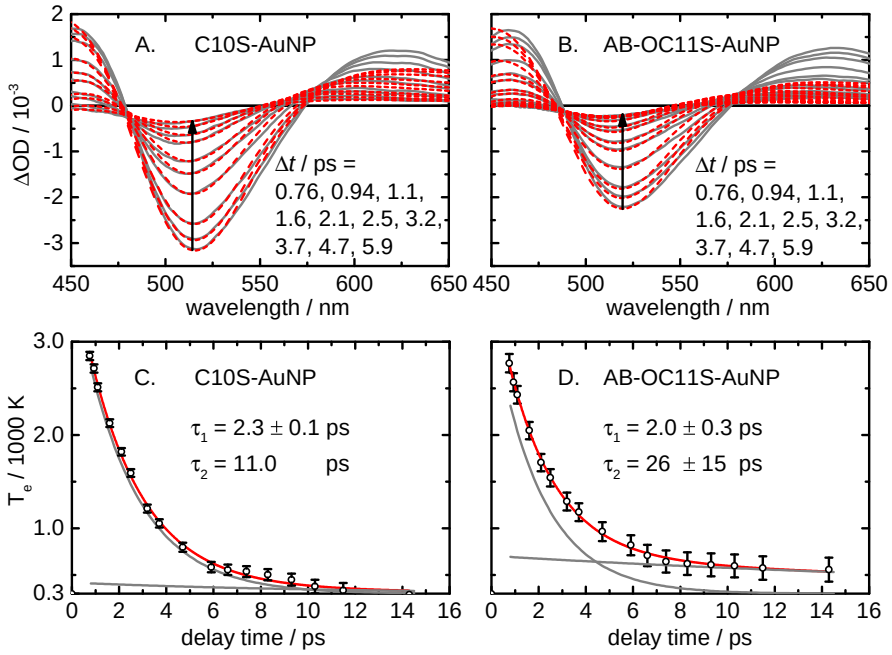

Figure 4.2: A and B: Transient spectra of the investigated AuNP samples (gray lines) overlaid with the respective temperature-dependent Mie theory fits (dashed red lines) at selected delay times. C and D: Electronic temperatures of the samples determined by the Mie theory fits as function of time (open circles) and fitted exponential cooling curves (solid red curves). Data at < 0.76 ps were omitted to avoid distortion of the fits due to incomplete subtraction of the toluene solvent signal.

Possessing a very high temperature of ~ 2800 K at the first pump–probe delay time ($\Delta t = 0.76$ ps), the plain alkylthiolated AuNPs are seen to cool down rapidly (in < 10 ps) following an exponential rate law within experimental errors with a lifetime constant of

$$\tau_{\text{e-ph}}(\text{AuNP}) = 2.3 \pm 0.1 \text{ ps}$$

to reach a (transient) electron-phonon equilibrium temperature within the NP system. A very minor secondary component with fixed decay constant of $\tau = 11$ ps was added to improve the quality of the fit at longer delay times, where the much slower phonon-solvent equilibration comes into play.

The temperature-time profile for our AB-AuNPs starts with nearly the same initial temperature and is described by a fast initial decay time constant of

$$\tau_{\text{e-ph}}(\text{AB-AuNP}) = 2.0 \pm 0.3 \text{ ps},$$

indicating very similar electron cooling dynamics in both AuNP systems. The larger error limit of the AB-AuNP value only results because of the larger uncertainties of the electron temperature data points. Additionally, as evident, a secondary time constant of $\tau = 26 \pm 15$ ps is needed for an adequate description of the time profile. As discussed below, however, this value and the apparent 500 K ``final'' temperature in Fig. 4.2D at $\Delta t = 15$ ps, where our analysis ended, have to be considered with considerable caution.

Based on the reference measurement for the free azothiol in solution (cf. Fig. S1), an excited-state absorption band associated with the AB photochromes in the ligand shell of our AB-AuNPs should show up in the transient spectra at probe wavelengths between ~ 375 to 450 nm. The relatively weak AB ESA is partially obscured by the intense LSPR features at short pump–probe delay times, but is unambiguously identified as a characteristic absorption band at longer times as illustrated in Fig. 4.3. Shown in the Figure are larger plots of our transient spectra from Fig. 4.1C at four selected delay times after excitation which clearly display the weak AB ESA band with only a slight peak shift to $\lambda = 415$ nm on the AuNPs. Moreover, the spectra indicate that the excited-state lifetime of the AB photochrome on the AuNPs is significantly longer than the lifetime of the LSPR excitation. The AB band is visible in the transient spectra from the beginning (Fig. 4.3A), becomes more prominent at later delay times (Figs. 4.3B, C), and is still visible, when the blue LSPR wing has virtually disappeared (Fig. 4.3D).

The associated dynamics were analyzed in the following by Lorentzian peak fitting. For enhanced flexibility, we used three Lorentzians to describe the LSPR features plus an additional fourth Lorentzian to model the AB ESA band. The excellent spectral fits are displayed for our AB-AuNPs at the chosen delay times in Fig. 4.3 (and with the individual Lorentzians in Fig. 4.7). Similar fits for the plain alkylthiolated AuNPs can be found in Fig. 4.8. The resulting temporal dynamics of the excitations of the Au core and the AB ligands are revealed by the plots of the respective amplitudes vs. time in Fig. 4.4. Accordingly, the three Lorentzian bands describing the Au core excitation decay with a common time constant within experimental

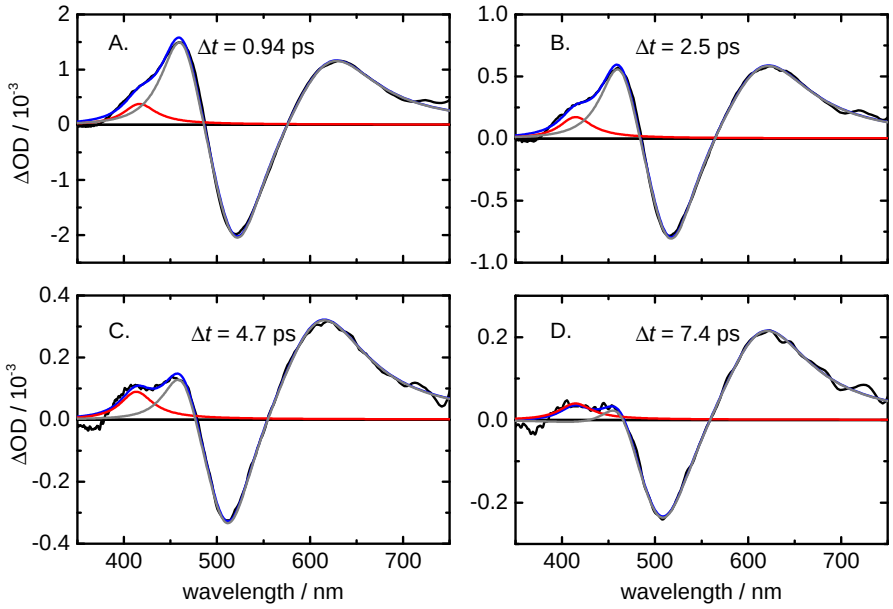

Figure 4.3: Transient spectra of the measured AB-AuNPs together with the fitted spectra at selected delay times (A: $\Delta t = 0.94$ ps, B: 2.5 ps, C: 4.7 ps, D: 7.4 ps). The measured spectra are shown in black, the fitted bands describing the LSPR dynamics in gray, the fitted band describing the AB ESA dynamics in red, and the overall fits (sum of LSPR and AB fits) are given by the blue lines. For clarity, the gray line gives only the sum of the three LSPR Lorentzians, a plot with the individual Lorentzians is given in Fig. 4.9.

errors of $\tau_{LSPR}(\text{AB-AuNP}) = 1.5 \pm 0.2$ ps (cf. Fig. 4.9). In contrast, the excited-state absorption assigned to the AB ligands decays in a bi-exponential fashion, with time constants of

$$\tau_1(\text{AB-AuNP}) = 1.2 \pm 0.2 \text{ ps},$$
$$\tau_2(\text{AB-AuNP}) = 4.7 \pm 1.1 \text{ ps},$$

close to those for the free azothiol in solution ($\tau_1(\text{AB}) = 2.0 \pm 0.1$ ps, $\tau_2(\text{AB}) = 5.1 \pm 0.4$ ps; see Fig. S1).

The above results showcase the ensuing dynamics of the investigated alkylthiolate- and azoalkylthiolate-functionalized gold nanoparticles in the first ~ 0.7 to 10 ps after excitation at $\lambda = 357$ nm. The UV light at this wavelength induces inter-band transitions in the Au metallic core, by which bound electrons from the *d* (conduction) band are projected into the *sp* (valence) band above the Fermi level.[34,37] At the same time, azobenzenes in the ligand shell around the functionalized NPs are promoted to their $\pi\pi^*$ (S_2) excited electronic state. A rough estimate based on the AuNP concentration and size and the employed excitation laser pulse power gives a number of on average ~ 5 absorbed photons per NP. For the AB-AuNPs, judged from the UV spectrum (Fig. 4.1A), and neglecting possible coupling, this

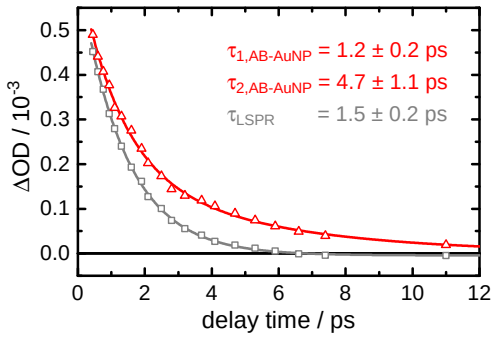

Figure 4.4: Decay profiles of the AB ESA (red) and the LSPR excitation (gray) at $\lambda_{probe} = 415$ nm extracted from the Lorentzian fits.

amounts to ~ 1.6 excited azobenzenes per NP (and corresponding ~ 3.4 photons absorbed by the Au core).

The excitation of the Au core results in a sudden jump of the electron temperature. Ultrafast dephasing ($\lesssim$ 10 fs) and electron–electron (e–e) scattering in roughly ~ 100 fs give a hot electron distribution with temperature T_e well above 3000 K, depending on the number of absorbed photons.[34] Aruda et al.[35] hinted at an e–e scattering relaxation time of 300 fs for alkylthiolated AuNPs very similar to ours. Based on those results, we assume e–e scattering to be completed before the beginning of our data analysis at $\Delta t = 0.76$ ps. Our transient spectra after 357 nm photoexcitation thus reflect the relaxation of the excited hot electron distribution of the AuNPs in the subsequent ~ 10 ps by electron–phonon (e–ph) scattering. On a comparable timescale, we also encounter the electronic deactivation and isomerization dynamics of the azobenzene ligands. Much slower relaxation processes on the ~ $10 - 100$ ps timescale, where the Au lattice and ligand vibrations equilibrate with the bulk solvent by phonon–phonon (ph–ph) scattering and heat transfer are left aside in this Letter.

Considering the alkylthiolated AuNPs, the temperature-dependent Mie theory fits in Fig. 4.2 indicate a hot electron temperature of T_e ~ 2800 K at the shortest ($\Delta t = 0.76$ ps) pump-probe delay time. Extrapolating the observed cooling curve, we estimate an initial electron temperature of T_e ~ 3900 K at $t = 0$. For the AB-AuNPs, we expect a significantly lower initial electron temperature due to the smaller number of absorbed UV photons (~ 3.4 vs. 5 photons on average) by the Au core. The weaker central LSPR bleach signal in the respective transient difference spectra (Fig. 4.2) is consistent with this assumption, but the intense positive wings to the red and blue are not. The respective Mie theory band fits indeed give almost the same electron temperature at the first data point and suggest an only marginally lower initial electron temperature after the pump pulse of T_e ~ 3600 K. This observation is taken as a hint for an energy transfer process from the $\pi\pi^*$ excited AB ligands to the Au core during the

excitation laser pulse. Several factors discussed in the literature[38,39] come to mind, although the details are not yet entirely clear. First, the absorption can be significantly enhanced by a locally increased electric field around the plasmonic system, leading to an increase in absorption cross section. Second, the $\pi\pi^*$ (resp. $n\pi^*$) excited AB molecules in the ligand shell may suffer energy transfer into the *sp* (valence) band of the Au core. Last but not least, the electronic structure of the ligand chromophores may by modified by fast core-to-ligand charge transfer within the duration of the pump pulse. The respective contributions depend on the applied exitation wavelength.[40] All three effects must be small in our AB-AuNP system in view of the observed efficient and reversible *trans–cis* photoisomerization observed in our static photoswitching experiments,[23] but not necessarily negligible. In an independent study of similar AuNPs functionalized with the *push–pull* azobenzene Disperse Red 1 (DR-1), we found evidence for very sizable core-to-ligand energy and charge transfer during the excitation pulse (see Chapter 5).

It has often been discussed whether ligands can influence the relaxation of the metal core of nanoparticles. If their electronic states participate in the cooling, the electronic heat capacity of the system becomes dependent on the density of electronic states near the Fermi level.[32,41] The ligands then act as a reservoir that slowly releases its temporarily stored energy to the Au core. The build-up of the hot electron distribution via e–e scattering is retarded, and the overall cooling via e–ph scattering gets slowed down as well. Such a view has recently been confirmed by Aruda et al., who detected substantial differences in the dynamics between aminated and thiolated AuNPs of similar size as ours.[35] We emphasize here that the Mie theory fit results for our alkylthiolated and azoalkylthiolated AuNPs are virtually identical with those of Aruda et al.[35] within experimental errors. A comparison between our AB-AuNPs and similar AuNPs carrying a naphthol or phenanthrol instead of the azobenzene showed little difference, however, which strongly indicates that only the sulfur atoms directly on the Au surface are of importance, whereas the distant large aromatic groups play little role because they are sufficiently insulated electronically by the alkyl spacer (see Chapter 6). In any case, the cooling dynamics by e–ph scattering of the hot electron distributions of both our AuNP systems are very similar to each other. The respective hot electron lifetimes of $\tau_{\text{e-ph}}(\text{AuNP}) = 2.3 \pm 0.1$ ps and $\tau_{\text{e-ph}}(\text{AB-AuNP}) = 2.0 \pm 0.3$ ps support the conclusion that the electronic states of the AB moiety do not strongly affect the dynamics in the Au core.

A quick estimate of the lattice temperature after completion of the e–ph relaxation gives a value of $\Delta T \sim 35$ K above room temperature. This value appears to be approached within experimental errors in the case of our alkylthiolated AuNPs, but the temperature-time pro-

file for the AB-AuNPs indicates a significantly higher ``final'' temperature. However, this has only been observed with azobenzene ligands, not with the large naphthol or phenanthrol ligands (see Chapter 6). Thus, the effect is considered as an artifact that results perhaps from a ``contamination'' of the transient spectra in the LSPR range by the weak $n\pi^*$ absorption band of *cis*-azobenzene photoproducts. The associated (very uncertain) $\tau = 26 \pm 15$ ps value goes beyond the timescale of interest in this work anyway. As mentioned, the slow eventual equilibration with the bath (solvent) by ph–ph scattering and heat transfer on the $10 - 100$ ps timescale[34] is not investigated here.

The ultrafast dynamics of plain AB after $\pi\pi^*$ excitation in solution are well known.[26,42] The initially excited S_2 state rapidly decays to the S_1 ($n\pi^*$) state via a conical intersection (CoIn) within $\tau_1 \sim 100$ fs. The isomerization and radiationless deactivation to the S_0 state take place from the S_1 state. For plain AB, time constants of $\tau_2 \sim 500$ fs and $\tau_3 \sim 3$ ps have been found, which are generally attributed to the departure of the excited wavepacket from the Franck-Condon (FC) region and the transition through the CoIn, respectively.[26] Slower vibrational cooling of the ``hot'' ground-state molecules follows with $\tau_4 \sim 10 - 20$ ps depending on the solvent. Quite similar dynamics have been identified in several substituted ABs, e.g. 4-butyl-4'-methoxyazobenzene,[43] 4-aminoazobenzene,[44] or the *push–pull* derivative DR-1.[45] The present measurements of the free AB-OC11SH azoligand in toluene after $\pi\pi^*$ excitation at 357 nm gave slightly longer excited-state lifetimes ($\tau_1(\mathrm{AB}) = 2.0 \pm 0.1$ ps, $\tau_2(\mathrm{AB}) = 5.1 \pm 0.4$ ps; see SI), but can be interpreted in a similar way. The ultrafast $S_2 \rightarrow S_1$ relaxation was not resolved, but presumably remains as the first step.

The identification of the weak excited-state absorption signature associated with the azobenzene in the ligand shell of the AuNPs required an extraordinarily careful examination of the measured transient difference spectra after photoexcitation. The characteristic ESA band near ~ 400 nm was uncovered only by the performed Lorentzian band fitting analysis, but clearly established without ambiguity. Following the spectral fits, the lifetime of the electronically excited AB photochromes in the AuNP ligand shell was obtained from the amplitude-time profile of the ESA band. The obtained lifetimes, $\tau_1(\text{AB-AuNP}) = 1.2 \pm 0.2$ ps and $\tau_2(\text{AB-AuNP}) = 4.7 \pm 1.1$ ps, resemble the ones for the free azoligand in solution (2.0 ± 0.1 resp. 5.1 ± 0.4 ps). The apparent shortening of τ_1 on the AuNPs by 40 % may hint at a decay contribution by an additional decay mechanism such as energy transfer to the AuNP LSPR, but this process cannot play a strong role. Time constant τ_1 is usually attributed to the motion of the wavepacket away from the Franck-Condon region, and this motion may be modified by the more rigid environment on the NPs. The amplitude-weighted mean lifetimes of $\langle\tau_{\mathrm{AB,AuNP}}\rangle = 2.3 \pm 0.5$ ps for

the AB-AuNP system vs. $\langle \tau_{AB,tol.} \rangle = 2.7 \pm 0.2$ ps in toluene solution are the same within the accuracy of our experiments. The lifetime belonging to the LSPR excitation determined from the Lorentzian band analysis (τ_{LSPR}(AB-AuNP) $= 1.5 \pm 0.2$ ps) appears somewhat smaller than the value indicated by the Mie theory fit, but this probably reflects the limited accuracy of the Mie theory model and the purely phenomenological nature of the Lorentzian peak fits alike. In any case, our results clearly indicate an efficient electronic decoupling of the AB photochrome and the Au metal core by the long (C11) alkyl linker chain used in this study at least after the first ~ 500 fs after the excitation laser pulse.

A major question that has to be left unanswered at present is that for the *trans*-to-*cis* isomerization quantum yield of the AB ligands on the AuNPs. The measured transient difference spectra for our sample show only a very weak and noisy negative feature at probe wavelengths around 370 nm, where a permanent bleach of the absorption by the *trans* isomer due to the isomerization is expected (cf. Figs. 4.3 and 4.5). As those features are too faint to be analyzed, we have no quantitative time-resolved confirmation of *trans*-to-*cis* isomerization after excitation at this time. However, our static measurements described earlier[23] do show efficient product formation after irradiation of AB-AuNPs in toluene at $\lambda = 365$ nm. The discrepancy between both experiments is explained by the much longer irradiation times and therefore higher turnover in the static compared to the present time-resolved measurements. Experimentally observed lower efficiencies of AB photoisomerization in mSAMs on AuNPs are likely explained mostly by the competing absorptions by the photochrome and the AuNP core at the employed wavelengths. The photoswitching yield is adversely affected by increasing the AuNP size through the less favorable surface-to-volume ratio and through the increasing absorption cross section of the LPSR band. Experiments using optimized, smaller AB-AuNP samples are presently underway in our laboratory to detect the formation of *cis*-AB photoproducts with full time-resolution.

In conclusion, we have investigated the photo-induced excited-state dynamics of *trans*-azobenzene (AB) on gold nanoparticles (AuNPs) functionalized with a mixed self-assembled monolayer (mSAM) of an ω-azobenzene-alkylthiol and decanethiol using femtosecond time-resolved transient absorption spectroscopy. The dynamics of the AB ligands were extracted from the measured transient spectra by Lorentzian band fitting. The results reveal almost unchanged behavior compared to the free azobenzene in solution. To the best of our knowledge, these results represent the first direct observation of the ultrafast dynamics of a molecular switch on AuNPs. Further, the transient absorption spectra were fitted with a temperature-dependent Mie theory model to examine the influence of the ligands on the local sur-

face plasmon resonance (LSPR) relaxation dynamics. The data indicate that the hot electron cooling dynamics by electron–phonon scattering in the AB-functionalized and in the plain decanethiol-functionalized AuNPs are practically the same. All results together show quantitatively that – at least after the first ~ 500 fs after the excitation laser pulse – the alkyl linker chain efficiently decouples the photochrome and the metallic Au core electronically, while the surface curvature of the NPs prevents possible steric hindrance during the isomerization. Both effects are decisive for the excellent photoswitching properties of these AB-AuNPs.

ACKNOWLEDGMENTS

The authors gratefully acknowledge the support of this work by the Deutsche Forschungsgemeinschaft through the Collaborative Research Centre 677 ``Function by Switching´´ and thank Prof. Dr. G. Friedrichs for valuable discussions.

BIBLIOGRAPHY

[1] Balzani, V.; Credi, A.; Venturi, M. *Molecular Devices and Machines: Concepts and Perspectives for the Nanoworld*; Wiley-VCH: Weinheim, 2008.

[2] Feringa, B. L.; Browne, W. R. *Molecular Switches*; Wiley-WCH, Weinheim, 2011; Vol. 1 & 2.

[3] Katsonis, N.; Lubomska, M.; Pollard, M. M.; Feringa, B. L.; Rudolf, P. *Progr. Surf. Sci.* **2007**, *82*, 407–434.

[4] Klajn, R. *Pure Appl. Chem.* **2010**, *82*, 2247–2279.

[5] Bandara, H. M. D.; Burdette, S. C. *Chem. Soc. Rev.* **2012**, *41*, 1809–1825.

[6] Comstock, M. J.; Levy, N.; Kirakosian, A.; Cho, J.; Lauterwasser, F.; Harvey, J. H.; Strubbe, D. A.; Fréchet, J. M. J.; Trauner, D.; Louie, S. G.; Crommie, M. F. *Phys. Rev. Lett.* **2007**, *99*, 038301.

[7] Wolf, M.; Tegeder, P. *Surf. Sci.* **2009**, *603*, 1506–1517.

[8] Schmidt, R.; Hagen, S.; Brete, D.; Carley, R.; Gahl, C.; Dokić, J.; Saalfrank, P.; Hecht, S.; Tegeder, P.; Weinelt, M. *Phys. Chem. Chem. Phys.* **2010**, *12*, 4488–4497.

[9] Tegeder, P. *J. Phys. Condens. Matter* **2012**, *24*, 394001.

[10] Benassi, E.; Granucci, G.; Persico, M.; Corni, S. *J. Phys. Chem. C* **2015**, *119*, 5962–5974.

[11] Evans, S. D.; Johnson, S. R.; Ringsdorf, H.; Williams, L. M.; Wolf, H. *Langmuir* **1998**, *14*, 6436–6440.

[12] Kumar, A. S.; Ye, T.; Takami, T.; Yu, B.-C.; Flatt, A. K.; Tour, J. M.; Weiss, P. S. *Nano Lett.* **2008**, *8*, 1644–1648.

[13] Jung, U.; Filinova, O.; Kuhn, S.; Zargarani, D.; Bornholdt, C.; Herges, R.; Magnussen, O. *Langmuir* **2010**, *26*, 13913–13923.

[14] Heinemann, N.; Grunau, J.; Leißner, T.; Andreyev, O.; Kuhn, S.; Jung, U.; Zargarani, D.; Herges, R.; Magnussen, O.; Bauer, M. *Chem. Phys.* **2012**, *402*, 22–28.

[15] Valley, D. T.; Onstott, M.; Malyk, S.; Benderskii, A. V. *Langmuir* **2013**, *29*, 11623–11631.

[16] Jung, U.; Schütt, C.; Filinova, O.; Kubitschke, J.; Herges, R.; Magnussen, O. *J. Phys. Chem. C* **2012**, *116*, 25943–25948.

[17] Gahl, C.; Schmidt, R.; Brete, D.; McNellis, E. R.; Freyer, W.; Carley, R.; Reuter, K.; Weinelt, M. *J. Am. Chem. Soc.* **2010**, *132*, 1831–1838.

[18] Moldt, T.; Brete, D.; Przyrembel, D.; Das, S.; Goldman, J. R.; Kundu, P. K.; Gahl, C.; Klajn, R.; Weinelt, M. *Langmuir* **2015**, *31*, 1048–1057.

[19] Klajn, R.; Bishop, K. J. M.; Grzybowski, B. A. *Proc. Nat. Acad. Sci. U. S. A.* **2007**, *104*, 10305–10309.

[20] Klajn, R.; Wesson, P. J.; Bishop, K. J. M.; Grzybowski, B. A. *Angew. Chem. Int. Ed.* **2009**, *48*, 7035 –7039.

[21] Klajn, R.; Stoddart, J. F.; Grzybowski, B. A. *Chem. Soc. Rev.* **2010**, *39*, 2203–2237.

[22] Shin, K.; Shin, E. J. *Bull. Korean Chem. Soc.* **2008**, *29*.

[23] Köhntopp, A.; Dabrowski, A.; Malicki, M.; Temps, F. *Chem. Commun.* **2014**, *50*, 10105–10107.

[24] Röttger, K.; Siewertsen, R.; Temps, F. *Chem. Phys. Lett.* **2012**, *536*, 140–146.

[25] Röttger, K.; Wang, S.; Renth, F.; Bahrenburg, J.; Temps, F. *Appl. Phys. B* **2015**, *118*, 185–193.

[26] Satzger, H.; Root, C.; Braun, M. *J. Phys. Chem. A* **2004**, *108*, 6265–6271.

[27] Satzger, H.; Spörlein, S.; Root, C.; Wachtveitl, J.; Zinth, W.; Gilch, P. *Chem. Phys. Lett.* **2003**, *372*, 216–223.

[28] Ciminelli, C.; Granucci, G.; Persico, M. *Chem. Eur. J.* **2004**, *10*, 2327–2341.

[29] Diau, E. W.-G. *J. Phys. Chem. A* **2004**, *108*, 950–956.

[30] Quick, M.; Dobryakov, A. L.; Gerecke, M.; Richter, C.; Berndt, F.; Ioffe, I. N.; Granovsky, A. A.; Mahrwald, R.; Ernsting, N. P.; Kovalenko, S. A. *J. Phys. Chem. B* **2014**, *118*, 8756–8771.

[31] Link, S.; El-Sayed, M. A. *Int. Rev. Phys. Chem.* **2000**, *19*, 409–453.

[32] Westcott, S. L.; Averitt, R. D.; Wolfgang, J. A.; Nordlander, P.; Halas, N. J. *J. Phys. Chem. B* **2001**, *105*, 9913–9917.

[33] Bauer, C.; Abid, J.-P.; Girault, H. H. *C R Chimie* **2006**, *9*, 261–267.

[34] Hartland, G. V. *Chem. Rev.* **2011**, *111*, 3858–3887.

[35] Aruda, K. O.; Tagliazucchi, M.; Sweeney, C. M.; Hannah, D. C.; Schatz, G. C.; Weiss, E. A. *Proc. Nat. Acad. Sci. U.S.A.* **2013**, *110*, 4212–4217.

[36] Link, S.; El-Sayed, M. A. *J. Phys. Chem. B* **1999**, *103*, 8410–8426.

[37] Voisin, C.; Fatti, N. D.; Christofilos, D.; Vallée, F. *J. Phys. Chem. B* **2001**, *105*, 2264–2280.

[38] Geddes, C. D.; Lakowicz, J. R. *J. Fluoresc.* **2002**, *12*, 121–129.

[39] Lakowicz, J. R. *Principles of Fluorescence Spectroscopy*; Springer: New York, 2006.

[40] Lee, J.; Lee, S.; Jen, M.; Pang, Y. *J. Phys. Chem. C* **2015**, *119*, 23285–23291.

[41] Bauer, C.; Abid, J.-P.; Girault, H. H. *J. Phys. Chem. B* **2006**, *110*, 4519–4523.

[42] Fujino, T.; Arzhantsev , S. Y.; ; Tahara, T. *J. Phys. Chem. A* **2001**, *105*, 8123–8129.

[43] Azuma, J.; Tamai, N.; Shishido, A.; Ikeda, T. *Chem. Phys. Lett.* **1998**, *288*, 77–82.

[44] Hirose, Y.; Yui, H.; Sawada, T. *J. Phys. Chem. A* **2002**, *106*, 3067–3071.

[45] Bahrenburg, J.; Röttger, K.; Siewertsen, R.; Renth, F.; Temps, F. *Photochem. Photobiol. Sci.* **2012**, *11*, 1210–1219.

4.2.1 TRANSIENT ABSORPTION DATA FOR AB-OC11SH IN TOLUENE SOLUTION

Figure 4.5 A shows the measured transient spectra of the free *trans*-azobenzene ligand AB-OC11SH in toluene solution. The most intense ESA band peaks at $\lambda_{probe} = 405$ nm. Only weak bands can be seen in the red part of the spectrum. The negative feature at $\lambda_{probe} \approx 370$ nm is attributed to the formation of the *cis*-AB photoproduct, which exhibits a much weaker absorption at this wavelength than the *trans*-AB isomer. The corresponding decay curve of the 405 nm ESA band as function of time is given in Fig. 4.5B. As can be seen, the experimental data are well described by a sum of two exponentials with time constants

$$\tau_1(\text{AB-OC11SH}) = 2.0 \pm 0.1 \text{ ps}$$

and

$$\tau_2(\text{AB-OC11SH}) = 5.1 \pm 0.4 \text{ ps}.$$

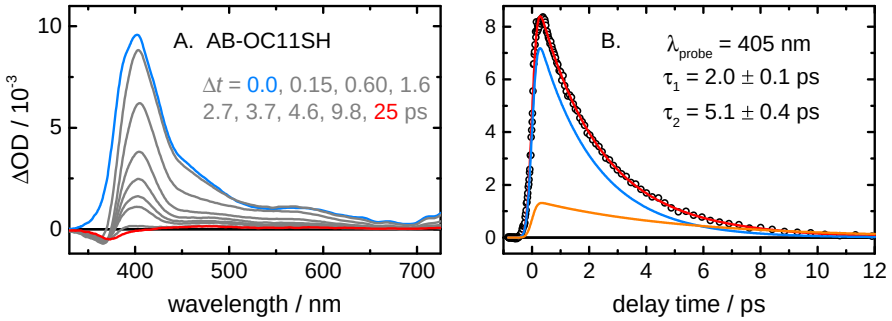

Figure 4.5: A) Measured transient absorption spectra of AB-OC11SH in toluene solution at different delay times after excitation at $\lambda = 357$ nm. The intense ESA band in the near-UV peaks at $\lambda = 405$ nm, all other contributions to the transient spectra are much weaker. B) Experimental time profile at $\lambda = 405$ nm (open circles) together with the associated least-squares fit curves and the obtained decay time constants.

The measured transient spectra of the functionalized AuNPs in the window between 450 and 650 nm around the LSPR band were analyzed using the temperature-dependent Mie theory model according to Aruda et al.[4.S1]

Mie Theory Fit Model

In short, the complex dielectric function of the AuNPs is composed of contributions from the free electrons (intra-band transitions) and the bound electrons (inter-band transitions). The dielectric function of the free electrons is given by the Drude model,

$$\epsilon_{\text{free}}(\omega, T_e) = 1 - \frac{\omega_P^2}{\omega^2 + i\gamma_{\text{free}}\omega}$$

with ω_P being the plasma frequency of gold. The dielectric function of the bound electrons is described by

$$\begin{aligned}\epsilon_{\text{bound}}(\omega, T_e) = Q_{\text{bulk}} \int_{\omega_g}^{\infty} \frac{\sqrt{x - \omega_g}}{x} [1 - F(x, T_e)] \\ \times \frac{(x^2 - \omega^2 + \gamma_{\text{bound}}^2 + i2\omega\gamma_{\text{bound}})}{(x^2 - \omega^2 + \gamma_{\text{bound}}^2)^2 + 4\omega^2\gamma_{\text{bound}}^2} \, dx\end{aligned}$$

with $F(x, T_e)$ being the Fermi distribution, ω_g the gap energy of gold and Q_{bulk} a constant determining the contribution of the bound electrons to the overall dielectric function. The values used in the fitting procedure are given in Table 4.1 and were determined by Scaffardi et al.[4.S2]

Table 4.1: Parameters used in the temperature-dependent Mie theory model fit. Q_{bulk} is a constant determining the contribution of bound electrons to $\epsilon(T_e)$, ω_P is the plasma frequency, E_F is the Fermi energy, E_g is the gap energy of gold.

Parameter	value
Q_{bulk}	$1.3 \cdot 10^{24}$
ω_P	$13 \cdot 10^{15}$ Hz
E_F	2.5 eV
E_g	2.1 eV

The sum of both contributions then enters into the absorption cross section of the AuNPs,

$$Q_{\text{abs}} = C\frac{a}{\lambda}\frac{\epsilon''(T_e)}{\epsilon''(T_e)^2 + (\epsilon'(T_e) + 2\epsilon_m)^2},$$

where $\epsilon'(T_e)$ and $\epsilon''(T_e)$ are the real and imaginary parts of $\epsilon(T_e)$, respectively, ϵ_m is the dielectric constant of the medium, a is the radius of the NPs, and C is a constant. The fit parameters obtained are the width parameters of the intra-band and inter-band transitions, γ_{free} and γ_{bound}, and the electronic temperature T_e.

Fit Results

Figures 4.6 A and B display the static UV/Vis absorption spectra of both AuNP samples measured at room temperature together with fits to the experimental spectra by the Mie theory model. The spectral shape of the LSPR band is very nicely reproduced by the fits in both cases. To obtain this level of agreement, the dielectric constant of the medium was set to $\epsilon_m = 2.1$ instead of the standard literature value of 2.38 for toluene.[4.S3] The small adjustment is justified by the different local environment of the AuNP core carrying an alkylthiol or AB-alkylthiol shell on the surface compared to ``naked'' AuNPs in toluene solvent. Fits to the spectra with a value of $\epsilon_m = 2.38$ significantly underestimated the absorption cross section in the UV, and slightly overestimated the absorption cross section in the red.

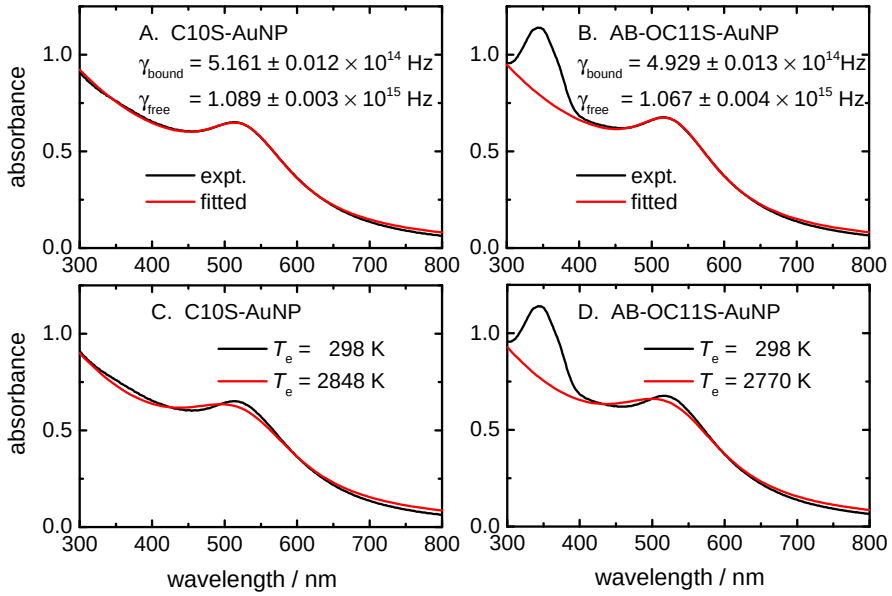

Figure 4.6: A and B: Experimental absorption spectra of the C10S-AuNP and AB-OC11S-AuNP samples (black) and the respective fitted spectra determined by the Mie theory model for $T_e = 298$ K (red lines). C and D: Comparison of the spectra at $\Delta t = 0.76$ ps after exitation (red), obtained by the temperature-dependent Mie theory fits to the experimental transient difference spectra at $\Delta t = 0.76$ ps, with fitted electron temperatures of $T_e = 2846$ K resp. 2770 K, to the static ($T_e = 298$ K) UV/Vis spectra (black) for both AuNP samples.

The values for the width parameters γ_{bound} and γ_{free} determined from the fits to the 298 K static spectra were then used in the following

for the fitting analysis of the transient absorption spectra (see main paper). Both γ_{bound} and γ_{free} could be determined with very high numerical precision for each sample, but the physical meaning of the small difference between the results for the two samples is restricted by the accuracy of the model. The average values of

$$\gamma_{bound} \approx 5.05 \times 10^{14} \text{ Hz}$$

and

$$\gamma_{free} \approx 1.08 \times 10^{15} \text{ Hz}$$

however agree well with the results of Aruda et al.[4.S1] for alkylthiolated AuNPs (who also reported a substantially different γ_{free} for aminated AuNPs) and reflect the femtosecond time scale of the associated e-e damping processes.

The applied 357 nm femtosecond laser excitation pulses heat the electrons in the conduction band of the AuNPs to temperatures in the T_e = 3600 to 3900 K range. Under these conditions, the LSPR bands are strongly broadened compared to the unexcited (298 K) NPs. The large effect of the high electron temperatures is illustrated in Figs. 4.6 C and D, which depict the simulated absorption spectra (red) of our two AuNP samples for T_e = 2848 K and 2766 K, respectively, compared to the spectra of the unexcited NPs (298 K, black).[2] Thus, since simple subtraction of the 298 K spectra from the simulated high T_e spectra then yields the transient difference spectra, as are experimentally observed by the femtosecond difference measurements, the electron temperatures of the ``hot'' AuNPs as function of time after excitation were determined by least-squares fitting of the simulated difference spectra to the experimental difference spectra (see main paper).

2 Note that the two T_e values are the ones determined by the temperature dependent Mie theory fits to the transient difference spectra at the earliest experimental delay time ($\Delta t = 0.76$ ps).

The transient absorption spectra of AB-AuNP and C10S-AuNP were analyzed by Lorentzian peak fitting as shown in Figs. 4.7 and 4.8, respectively. Three bands were used for both AuNP samples to describe the dynamics of the Au core. An additional Lorentzian was needed for fitting the AB ESA band of the AB-AuNP sample.

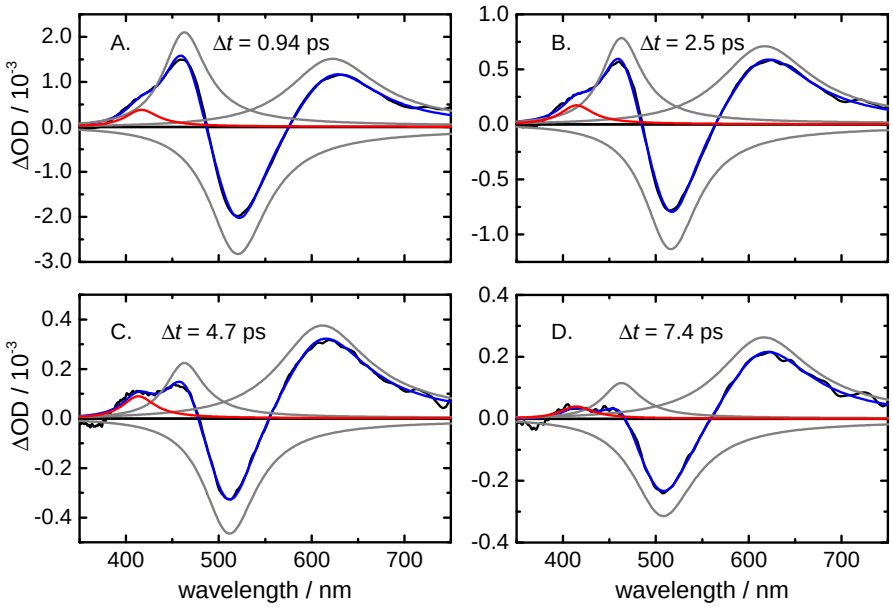

Figure 4.7: Transient absorption spectra of AB-AuNPs with the respective Lorentzian fits at different pump–probe delay times (A: Δt = 0.94 ps, B: 2.5 ps, C: 4.7 ps, D: 7.4 ps). The measured transient spectra are shown in black, the fits describing the LSPR contributions in gray, the Lorentzian describing the AB ESA contribution in red, and the overall fit in blue.

The time profiles for the three Au core bands with their fitted exponential decay curves and time constants are shown in Fig. 4.9. All three bands decay with nearly the same time constant in ~ 1.5 ps. The slower decay of the AB ESA can clearly be separated from the Au core contributions.

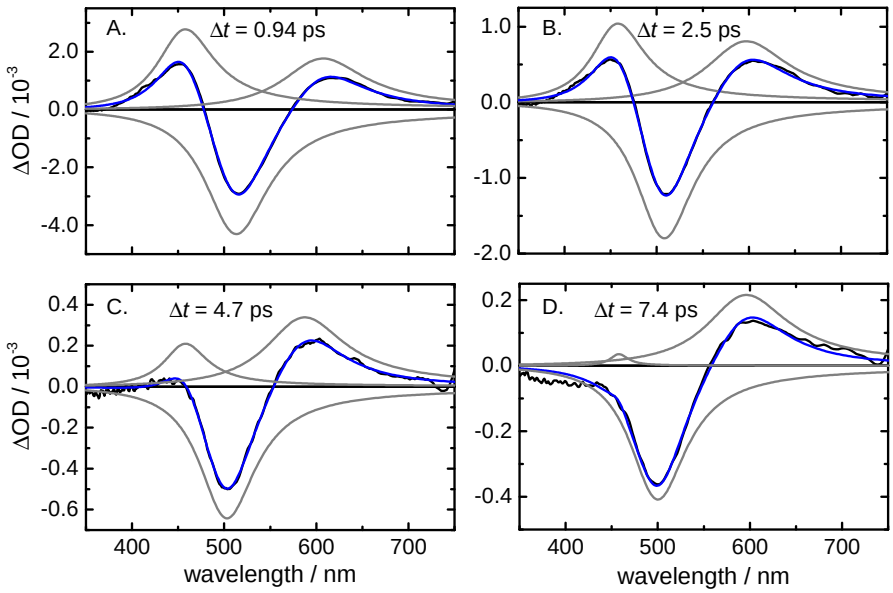

Figure 4.8: Transient absorption spectra of C10S-AuNPs with the respective Lorentzian fits at different pump–probe delay times (A: $\Delta t = 0.94$ ps, B: 2.5 ps, C: 4.7 ps, D: 7.4 ps). The measured transient spectra are shown in black, the fits describing the LSPR contributions in gray and the overall fit in blue.

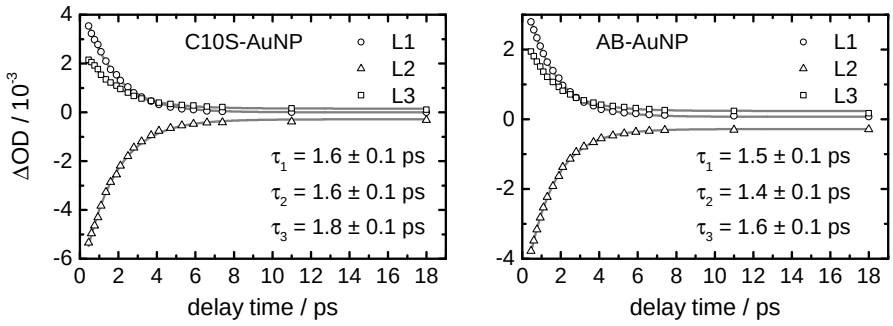

Figure 4.9: Time profiles of the three Lorentzians used to fit the transient absorption bands of the Au core in C10S-AuNP (left) and AB-AuNP spectra (right). L1 describes the band centered at 460 nm, L2 the negative band at 510 nm and L3 the band in the visible centered around 600 nm. All three bands decay with nearly the same time constant in ~ 1.5 ps.

4.S1. Aruda, K. O.; Tagliazucchi, M.; Sweeney, C. M.; Hannah, D. C.; Schatz, G. C.; Weiss, E. A. *Proc. Nat. Acad. Sci. U.S.A.* **2013**, *110*, 4212.

4.S2. Scaffardi, L. B.; Tocho, J. O. *Nanotechnology* **2006**, *17*, 1309.

4.S3. Weast, R. C. *CRC Handbook of Chemistry and Physics*, 1st Edition, CRC Press **1987**.

5

FEMTOSECOND TRANSIENT ABSORPTION SPECTROSCOPY ON DISPERSE RED 1-FUNCTIONALIZED GOLD NANOPARTICLES

5.1 INTRODUCTION

Functionalized gold nanoparticles (AuNPs) have become important for applications in a large number of fields ranging from optics and data storage over imaging techniques,[1–5] sensors,[4,6–8] and material science[1,9–11] to medical diagnostics and drug delivery.[1,3,4,12–14] A combination of the unique optical, chemical, physical and magnetic properties of AuNPs with photoresponsive molecular switches offers new ways toward the development of light-controlled smart materials.

Coupling between AuNP and ligands is widely discussed in the literature and known to influence the optical properties of these hybrid systems. The attachment of ligands changes the absorption cross section of AuNPs and can enhance or dampen the localized surface plasmon resonance (LSPR) as well as shift its position.[1,15–20] The LSPR is not only very sensitive to changes in the electronic structure of the AuNP, it can also couple resonantly with close-lying absorption bands of ligands that are attached to the AuNP.[21–24] Electronic coupling between organic molecules and metals is known to change the radiative decay rates and the excited state lifetimes of the chromophore significantly.[25–27] In most cases, the metal quenches the excited state of the chromophore *via* energy or charge transfer (CT) from the ligand to the AuNP, which can often be observed through reduced fluorescence intensities or complete quenching of the emission.[25,28–30] Under optimized conditions, however, enhancement of the fluorescence has been observed as well.[31,32] The type of interaction that is found in the chromophore-NP hybrid system depends on a number of different facotrs, e.g. the NP size, the chromophore-NP distance, the orientation of the chromophore relative to the surface and the packing of the chromophores on the NP.

Azobenzene-functionalized AuNPs are widely used as model systems for photoswitchable AuNPs and to investigate the photophysical behaviour of molecular switches in self-assembled monolayers (SAMs) and the induced changes in AuNP properties.[33–40] While the ultrafast dynamics of azobenzene (AB) and its derivatives have been investigated in solution[41–44] and more restricted environments such as polymer colloids,[45] thin polymer films,[46,47] and on flat quartz

surfaces,[47] no literature on the dynamics in proximity to AuNPs is available at the moment.

To shed some light on the photo-induced dynamics of photoresponsive chromophore-functionalized AuNPs, we functionalized small AuNPs (~ 4 nm) with SAMs of decanethiol (C10SH) and mixed self-assembled monolayers (mSAMs) of decanethiol and a Disperse Red 1 derivative (DR1-C3SH) shown in Figure 5.1 and investigated the ultrafast dynamics using femtosecond time-resolved transient absorption spectroscopy.

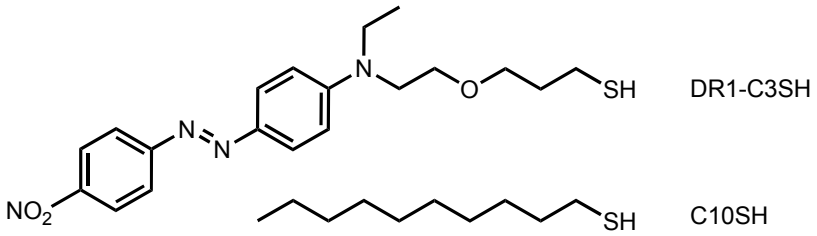

Figure 5.1: The chemical structures of thiol-functionalized Disperse Red 1 (DR1-C3SH) and decanethiol (C10SH).

The *push-pull* substituted AB Disperse Red 1 (DR-1) possesses a large absorption cross section, making simultaneous excitation of ligand and AuNP possible even at low dye concentrations. Furthermore, the enormous transient absorption signals of DR-1 should allow for identification of ligand related signals in the presence of the strong LSPR signals.[43] The recorded transient spectra reveal large changes in signal intensity when plain decanethiol-functionalized AuNPs (C10SAuNPs) are compared with DR-1-functionalized AuNPs (DR1-C3SAuNPs). A possible explanation for the effect could be a charge transfer from the AuNP core to the excited DR-1 ligand.

5.2 EXPERIMENTAL SECTION

MATERIALS

The thiol-functionalized Disperse Red 1 was synthesized by Grace Suana in the Institute of Organic Chemistry (University of Kiel) in the research group of Prof. Herges. Decanethiol was purchased from Aldrich and used without further purification. Oleylamine-stabilized gold nanoparticles (AuNPs) with a diameter of ~ 4 nm were synthesized through reduction of $HAuCl_4 \cdot 3\ H_2O$ with $NaBH_4$ in the presence of oleylamine and methanol in toluene solution. The obtained AuNPs were then used in a ligand exchange procedure to produce AuNPs functionalized with SAMs of C10SH resp. a mSAM of C10SH and DR1-C3SAuNPs. The purity of the AuNP samples was checked by UV/Vis and ^1H NMR spectroscopy. A detailed description of the synthesis and characterization of the AuNPs can be found in an ear-

lier publication.[39] To ensure the same particle size distribution, all samples came from the same batch of aminated AuNPs.

FEMTOSECOND TRANSIENT ABSORPTION MEASUREMENTS

For femtosecond transient absorption measurements an excitation wavelength of $\lambda = 467$ nm (focus size: 600 µm, 250 nJ) was used. The complete experimental setup has been described in the literature.[48,49] In short, a Ti:Sa laser delivered 150 fs pulses with a center wavelength of $\lambda = 775$ nm at a repetition rate of 1 kHz. The laser fundamental was split into pump and probe, the excitation pulses were generated in a NOPA and compressed to a temporal width of $\approx$ 45 fs in a prism compressor. The probe beam was focused into a CaF_2 plate to generate whitelight pulses for broadband detection. They were split into probe and reference and focused into the sample cell, where the probe pulses were overlapped with the pump pulses. Probe and reference pulses were detected after passing a prism spectrograph with two FFT-CCD cameras. The samples were measured in solution in toluene at optical densities between 0.5 and 0.8 in a flow cell of 1 mm pathlength. All samples have been measured directly one after another under the same conditions to ensure comparability of all data. The obtained spectro-temporal maps were corrected for solvent signals. Spectroscopically pure toluene was used for all measurements.

5.3 RESULTS

STATIC ABSORPTION MEASUREMENTS

The static absorption spectra of C10SAuNPs, free DR-1, and DR1-C3SAuNPs are depicted in Figure 5.2. The time-resolved measurements after excitation at $\lambda = 467$ nm were performed at the optical densities shown in Figure 5.2a, the excitation wavelength is indicated by the vertical dashed line.

From the static absorption spectra the number of DR-1 molecules per NP can be calculated. In Figure 5.2b the spectrum of C10SAuNP (dashed black) has been scaled to match the absorbance of the DR1-C3SAuNP sample (red) at $\lambda = 355$ nm. The difference of both spectra then represents the pure DR-1 absorbance in the DR1-C3SAuNP sample. The DR-1 absorption spectrum (dark grey) calculated in this way has a maximum absorbance of $\Delta A_{DR1} = 0.184$. With the DR-1 extinction coefficient of $\epsilon_{DR1} = 3.6 \cdot 10^5\,L \cdot mol^{-1} \cdot cm^{-1}$ and the extinction coefficient of 4 nm AuNPs, $\epsilon_{AuNPs} = 4.58 \cdot 10^6\,L \cdot mol^{-1} \cdot cm^{-1}$, the pure DR-1 absorbance corresponds to $\sim$ 45 DR-1 ligands per AuNP. Figure 5.2b also shows a direct comparison of the calculated DR-1 absorbance on the AuNPs (dark gray) and the measured DR-1 ab-

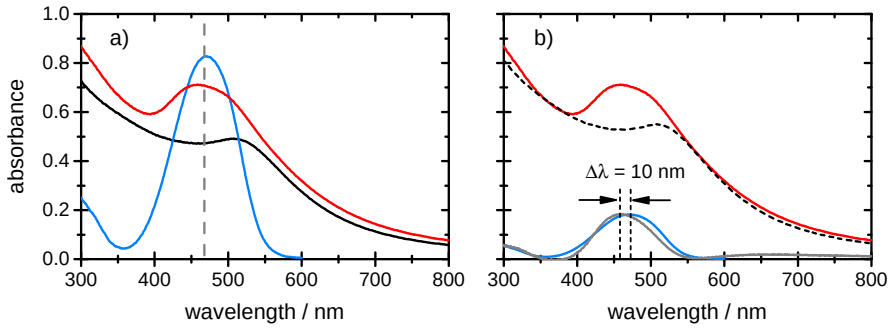

Figure 5.2: a) The static absorption spectra of DR1-C3SAuNPs (red), C10SAuNPs (black), and DR-1 (blue) as measured directly after the time-resolved measurements. The vertical dashed line shows the excitation wavelength $\lambda_{ex} = 467$ nm. b) The static absorption spectrum of C10SAuNPs (dashed black) was multiplied by a factor of 1.12 to match the absorbance of DR1-C3SAuNPs (red) at $\lambda = 355$ nm. The difference of both spectra (dark gray) corresponds to the pure DR-1 absorption on the DR1-C3SAuNPs. Compared to DR-1 in solution (blue), the absorbance on the AuNPs is blue-shifted by 10 nm.

sorbance in solution (blue). Both spectra have similar shapes. However, the DR-1 absorbance on the AuNPs is blue-shifted by ~ 10 nm.

FEMTOSECOND TRANSIENT ABSORPTION MEASUREMENTS

The transient absorption spectra of C10SAuNPs, DR1-C3SAuNPs, and DR-1 at different delay times after excitation at $\lambda_{ex} = 467$ nm are shown in Figure 5.3a-c. Due to residual scattered light the grey shaded spectral range around the excitation wavelength cannot be analyzed. The transient spectra are shown in the wavelength range of $\lambda = 350 - 750$ nm. The signal maximum is reached at a delay time of $\Delta t = 0.37$ ps, shown in blue for all three samples. The temporal evolution thereafter can be observed with the help of spectra at selected later delay times, which are shown in grey here. The same delay times are given for all three samples. The spectra at the latest given time ($\Delta t = 96$ ps for the AuNP spectra respectively $\Delta t = 1425$ ps for DR-1) are shown in red.

The transient spectra of C10SAuNPs (Figure 5.3a) show a strong bleach at the position of the LSPR ($\lambda = 480 - 600$ nm), a positive band at shorter wavelengths ($\lambda = 380 - 450$ nm), and two overlapping positive bands at longer wavelengths ($\lambda = 600 - 750$). The spectral shape with these three distinct spectral regions is typical for spherical AuNPs and has frequently been reported in the literature.[50–52] It arises from the broadening and damping of the LSPR at higher electronic temperatures after the AuNPs have been excited. For the C10SAuNPs, all signals decay quickly within ~ 10 ps, very little change is observed afterwards.

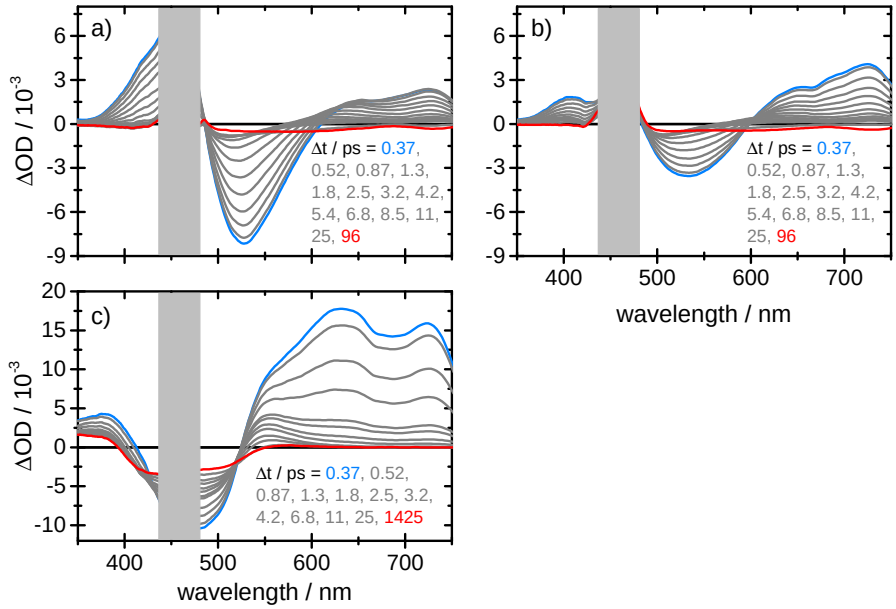

Figure 5.3: Measured transient absorption spectra of a) C10SAuNPs, b) DR1-C3SAuNPs, and c) DR-1. The grey areas cover the spectral range of scattered pump light.

The spectra of DR1-C3SAuNPs in Figure 5.3b also show a bleach at $\lambda = 480 - 600$ nm, a positive signal at shorter wavelengths ($\lambda = 380 - 450$ nm) and two overlapping positive signals at longer wavelengths ($\lambda = 600 - 750$ nm). The signals decay almost completely within the first 10 ps, only very little change occurs at later times.

The transient data of free DR-1 in solution in Figure 5.3c show very large signals over the whole wavelength range. Strong excited state absorption (ESA) and hot ground state absorption (HGSA) is visible between $\lambda = 530 - 750$ nm. The two ESA bands with their maxima at $\lambda = 640$ nm and $\lambda = 716$ nm decay very fast, the excited state dynamics are finished within 3 ps. The HGSA band at $\lambda = 550$ nm shows a delayed rise and is still visible after 25 ps. A ground state bleach (GSB) can be seen at $\lambda = 430 - 530$ nm, a permanent product absorption appears below $\lambda = 400$ nm. Both signals do not decay until the end of the measurement (1.4 ns). The ultrafast dynamics of free DR-1 in solution have been examined extensively and are described in detail in the literature, therefore only this short overview shall be given here.[43]

In the following the transient spectra of the two AuNP samples (Figure 5.3a and b) are compared. The shapes of both sets of spectra look very similar, while the intensities are very different. The bleaching signal in the DR1-C3SAuNP sample at the identical delay time ($\Delta t = 0.37$ ps) is smaller by a factor of 2.3 and has a width of FWHM = 79 nm compared to FWHM = 69 nm in the C10SAuNP sample. The positive signals in the long wavelength range on the other hand are a factor of ~ 1.6 more intense than in the C10SAuNP spectra. As all

samples were measured on the same day directly after one another under the same conditions within experimental errors, the intensity changes are real effects and do not arise from different measurement conditions. Scaling the transient spectra to the same AuNP concentration, as previously shown for the static absorption spectra (see Figure 5.2b for comparison), does not compensate for the intensity differences excluding a concentration effect.

In the DR1-C3SAuNPs spectra (Figure 5.3b), no signals which can unambiguously be attributed to DR-1 on the AuNPs are easily identified. The GSB, which is prominent in the pure DR-1 data at $\lambda = 430 - 530$ nm, is obscured by scattered pump light and no long-lived product absorption of isomerized DR-1 below 400 nm is visible. The absorption band with an apparent maximum at $\lambda = 410$ nm could be due to an overlap of the positive absorption of the AuNPs with the intense negative GSB of DR-1, such that only the blue wing of the positive signal is visible here. However, a complete description of the signal shape is not possible at this point due to the scattered pump light covering a critical spectral range in these measurements.

Under the assumption that the measured DR1-C3SAuNP spectra are simply a superposition of the C10SAuNP and the DR-1 signals, calculation of the transient spectra was attempted. We tried to achieve a match between measured and calculated spectra by forming either the sum of C10SAuNPs and DR-1 or the difference between DR1-C3SAuNPs and DR-1 or DR1-C3SAuNPs and C10SAuNPs using different scaling factors for the individual contributions to account for the different optical densities in the three measurements. However, no method successfully reproduced the measured transient spectra, showing that in the DR1-C3SAuNP data the spectral shape of the transient signals is changed compared to the measurements of the single components. The results hint at substantial coupling between DR-1 and AuNP.

Figure 5.4 compares the absorption time profiles of C10SAuNPs, DR1-C3SAuNPs and free DR-1 at three selected wavelengths. Here, only the first 15 ps are given, as this is the time frame in which the DR-1 dynamics are finished and all excitation energy is transferred from the Au core into vibrations of the lattice and the ligand shell. Only the time profile at $\lambda = 415$ nm is shown at short delay times and up to 200 ps.

Figures 5.4 a and c show the normalized absorption time profiles of C10SAuNPs and DR1-C3SAuNPs at $\lambda = 415$ nm and $\lambda = 520$ nm, respectively. At both wavelengths both samples initially decay with very similar time constants of $\approx 1.5 - 2$ ps, showing no influence of the DR-1 ligand on the dynamics. At $\lambda = 415$ nm, the DR1-C3SAuNP signal is still positive after 15 ps, while the C10SAuNP signal has clearly become negative. In this spectral range free DR-1 shows permanent product absorption (PA), therefore this may be interpreted as

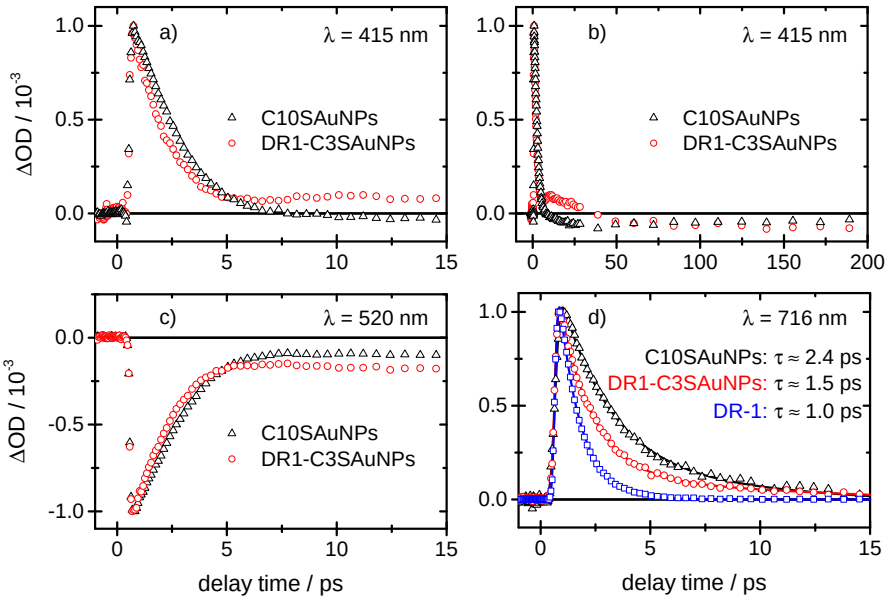

Figure 5.4: Normalized transient absorption-time profiles of C10SAuNPs (black triangles), DR1-C3SAuNPs (red circles) and DR-1 (blue squares) at three representative probe wavelengths. The timeprofiles at $\lambda = 415$ nm are shown at short delay times (a) and up to 200 ps (b). For the timeprofile at $\lambda = 716$ nm (d) nonlinear least squares fits to the data and the resulting time constants are given.

product formation on the AuNPs. However, the DR1-C3SAuNP signal becomes negative after ~ 50 ps (Figure 5.4b) and thereafter follows the C10SAuNP dynamics, which makes this interpretation questionable. The formation of a short-lived product is however possible and cannot completely be ruled out at this point. At $\lambda = 716$ nm (Figure 5.4d), where the ESA of free DR-1 is particularly strong, a different behaviour is observed: the lifetime of DR1-C3SAuNPs, $\tau \approx 1.5$ ps, lies between the lifetimes of C10SAuNPs, $\tau \approx 2.4$ ps, and free DR-1, $\tau \approx 1.0$ ps. Here, the DR1-C3SAuNP time profile seems to contain contributions from both, DR-1 and the C10SAuNPs, so that the value of the time constant obtained from a simple fit lies between the other two time constants. A more detailed analysis is complicated by the very similar time scales of both contributions.

5.4 DISCUSSION

The transient absorption signals of DR1-C3SAuNPs show very different intensities compared to C10SAuNPs, especially the intensity of the bleach signal is reduced dramatically. Additionally, there are no signals which can be unambiguously attributed to the DR-1 ligand itself. The transient spectra of the DR1-C3SAuNP sample cannot be constructed as a superposition of the C10SAuNP and DR-1 spectra,

which indicates an electronic interaction between DR-1 ligand and AuNP that changes the shape of the DR-1 absorption signals.

The pronounced changes in the shape of the transient spectra can be explained by a number of different factors, that have been discussed in the literature.[26,27] First, the locally increased electric field around the plasmonic AuNP can lead to an enhanced absorption cross section of the DR-1 chromophore. Second, an energy transfer from the ligands into the *sp* band of the Au core may quench the excited state of DR-1. Third, fast core-to-ligand charge transfer occurring within the duration of the pump pulse may modify the electronic structure of the ligands. We assume a CT from the electronically excited AuNP into the DR-1 molecule as shown schematically in Figure 5.5 to be the major reason for the observed differences in the transient spectra of DR1-C3SAuNPs and C10SAuNPs.

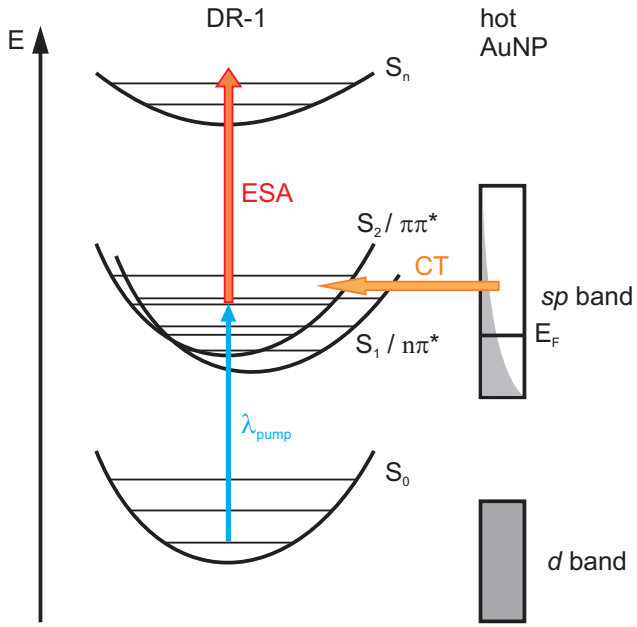

Figure 5.5: Schematic of the charge transfer between DR-1 ligand (left) and AuNP (right). The pump pulse brings the DR-1 to the S_2 ($\pi\pi^*$) state from where it relaxes in $\approx$ 100 fs to the S_1 ($n\pi^*$) state. The same pulse excites electrons in the AuNP core from the *d* band to the *sp* band above Fermi level, where a hot electron distribution is formed rapidly within a few hundred femtoseconds. A charge transfer occurs from the *sp* band of the hot AuNP to the DR-1 ligand, probably changing the electronic structure of the DR-1 and subsequently its transient absorption spectra.

An electron is transferred from the *sp* band of the hot AuNPs to the ligand and thereby the electronic structure of DR-1 should be changed dramatically. The electron may be transferred into one of the excited states as implied in Figure 5.5 or into the ground state of DR-1. A changed electronic structure subsequently should lead to different excited-state dynamics of the DR-1 molecule and therefore different

transient absorption spectra as compared to DR-1 in solution. The process is most likely caused by coupling of the energetically close-lying $\pi\pi^*$ absorption band of DR-1 and the LSPR of the AuNP core in the intense light field of the excitation pulse. Energy and charge transfer processes between metals and organic chromophores are well known to lead to a number of effects, e.g. the quenching or enhancement of fluorescence, changes in fluorescence quantum yields and altered excited-state lifetimes.[27,28,30,53] Recently, Lee et al. reported on the metal-enhanced fluorescence of a stilbene-derivative in the vicinity of silver nanoparticles (AgNPs). They attributed the effect to an ultrafast charge transfer from the excited plasmon of the AgNPs into the emitting intramolecular charge-transfer (ICT) state of the chromophore, which resulted in a significantly increased fluorescence lifetime.[32]

A similar process is conceivable in our case. However, a detailed analysis to disentangle the dynamics of DR-1 and the AuNP core is difficult because both components relax on very similar time scales. Comparison of the time profiles reveals practically unchanged dynamics below 550 nm. Furthermore, long-lived DR-1 product signals are absent. The reasons for the hindered product formation are not entirely clear at the moment, but two possible explanations come to mind: (i) *cis* product is formed and rapidly isomerizes back to the *trans* form or (ii) the core-to-ligand charge transfer prevents the product formation altogether. Upon $\pi\pi^*$ (resp. $n\pi^*$) excitation of DR-1, the central N=N double bond is weakened, allowing for the isomerization to proceed via a rotational motion around this bond. When an additional electron is transferred into the excited DR-1 unit this rotation may well be hampered, which could prevent the *trans-cis* isomerization altogether.

To gain more detailed insight into the nature of the ligand-AuNP interaction and to explain the observed dramatic changes in the transient absorption spectra more precisely, further investigations are necessary. Reduction of the scattered pump light is essential for these experiments, reduction of the AuNP size and thus the LSPR signal would facilitate the separation of AuNP and ligand signals. Furthermore, fluorescence studies could shed light on the details of the possible core-to-ligand charge transfer.

5.5 CONCLUSION

The femtosecond transient absorption spectra of gold nanoparticles (AuNPs) functionalized with pure decanethiol and with a mixed self-assembled monolayer of decanethiol and a Disperse Red 1-derivative as well as of pure Disperse Red 1 have been measured in solution after excitation with $\lambda = 467$ nm. The time-resolved data show considerable differences in signal intensity between the two AuNP samples.

The observations suggest a change in the spectral shape of the transient DR-1 signals, which could be due to an ultrafast core-to-ligand charge transfer that takes place within the duration of the excitation pulse. Further evidence for an electronic interaction between chromophore and AuNP is provided through the absence of permanent product formation. The near resonance in energy between the $\pi\pi^*$ absorption band of DR-1 and the LSPR of the AuNP core should play an essential role for the observed effect.

BIBLIOGRAPHY

[1] Thomas, K. G.; Kamat, P. V. *Acc. Chem. Res.* **2003**, *36*, 888–898.

[2] Chang, H.-C.; Liu, C.-L.; Chen, W.-C. *Adv. Funct. Mater.* **2013**, *23*, 4960–4968.

[3] Boisselier, E.; Astruc, D. *Chem. Soc. Rev.* **2009**, *38*, 1759–1782.

[4] Wilson, R. *Chem. Soc. Rev.* **2008**, *37*, 2028–2045.

[5] Sun, Y.; Wang, D.; Xu, L.; Zhao, T.; Wang, C.; Sun, H.; Lin, Q. *RSC Adv.* **2015**, *5*, 52088–52094.

[6] Mayer, K. M.; Hafner, J. H. *Chem. Rev.* **2011**, *111*, 3828–3857.

[7] Anker, J. N.; Hall, W. P.; Lyandres, O.; Shah, N. C.; Zhao, J.; van Duyne, R. P. *Nat. Mater.* **2008**, *7*, 442–453.

[8] Lee, J.-S.; Han, M. S.; Mirkin, C. A. *Angew. Chem. Int. Ed.* **2007**, *46*, 4093–4096.

[9] Klajn, R.; Wesson, P. J.; Bishop, K. J. M.; Grzybowski, B. A. *Angew. Chem. Int. Ed.* **2009**, *48*, 7035 –7039.

[10] van der Molen, S. J.; Liao, J.; Kudernac, T.; Agustsson, J. S.; Bernard, L.; Calame, M.; van Wees, B. J.; Feringa, B. L.; Schönenberger, C. *Nano Lett.* **2009**, *9*, 76–80.

[11] Ikeda, M.; Tanifuji, N.; Yamaguchi, H.; Irie, M.; Matsuda, K. *Chem. Commun.* **2007**, 1355–1357.

[12] Rosi, N. L.; Giljohann, D. A.; Thaxton, C. S.; Lytton-Jean, A. K. R.; Han, M. S.; Mirkin, C. A. *Science* **2006**, *312*, 1027–1030.

[13] Louis, C.; Pluchery, O. *Gold Nanoparticles for Physics, Chemistry and Biology*; Imperial College Press, London, 2012.

[14] Giljohann, D. A.; Seferos, D. S.; Daniel, W. L.; Massich, M. D.; Patel, P. C.; Mirkin, C. A. *Angew. Chem. Int. Ed.* **2010**, *49*, 3280–3294.

[15] Liu, X.; Atwater, M.; Wang, J.; Huo, Q. *Colloids Surf., B* **2007**, *58*, 3–7.

[16] Aruda, K. O.; Tagliazucchi, M.; Sweeney, C. M.; Hannah, D. C.; Schatz, G. C.; Weiss, E. A. *Proc. Nat. Acad. Sci. U.S.A.* **2013**, *110*, 4212–4217.

[17] Henglein, A. *J. Phys. Chem.* **1993**, *97*, 5457–5471.

[18] Linnert, T.; Mulvaney, P.; Henglein, A. *J. Phys. Chem.* **1993**, *97*, 679–682.

[19] Persson, B. *Surf. Sci.* **1993**, *281*, 153–162.

[20] Mulvaney, P. *Langmuir* **1996**, *12*, 788–800.

[21] Haes, A. J.; Zou, S.; Zhao, J.; Schatz, G. C.; Van Duyne, R. P. *J. Am. Chem. Soc.* **2006**, *128*, 10905–10914.

[22] Zhao, J.; Jensen, L.; Sung, J.; Zou, S.; Schatz, G. C.; Van Duyne, R. P. *J. Am. Chem. Soc.* **2007**, *129*, 7647–7656.

[23] Wurtz, G. A.; Evans, P. R.; Hendren, W.; Atkinson, R.; Dickson, W.; Pollard, R. J.; Zayats, A. V.; Harrison, W.; Bower, C. *Nano Lett.* **2007**, *7*, 1297–1303.

[24] Debnath, T.; Dana, J.; Maity, P.; Lobo, H.; Shankarling, G. S.; Ghosh, H. N. *Chem. Eur. J.* **2015**, *21*, 5704–5708.

[25] Dulkeith, E.; Morteani, A. C.; Niedereichholz, T.; Klar, T. A.; Feldmann, J.; Levi, S. A.; van Veggel, F. C. J.; Reinhoudt, D. N.; Möller, M.; Gittins, D. *Phys. Rev. Lett.* **2002**, *89*, 203002–1.

[26] Geddes, C. D.; Lakowicz, J. R. *J. Fluoresc.* **2002**, *12*, 121–129.

[27] Lakowicz, J. R. *Principles of Fluorescence Spectroscopy*; Springer: New York, 2006.

[28] Barazzouk, S.; Kamat, P. V.; Hotchandani, S. *J. Phys Chem. B* **2005**, *109*, 716–723.

[29] Kotiaho, A.; Lahtinen, R.; Efimov, A.; Metsberg, H.-K.; Sariola, E.; Lehtivuori, H.; Tkachenko, N. V.; Lemmetyinen, H. *J. Phys. Chem. C* **2010**, *114*, 162–168.

[30] Dana, J.; Debnath, T.; Maity, P.; Ghosh, H. N. *J. Phys. Chem. C* **2015**, *119*, 2046–2052.

[31] Aslan, K.; Malyn, S. N.; Geddes, C. D. *J. Fluoresc.* **2007**, *17*, 7–13.

[32] Lee, J.; Lee, S.; Jen, M.; Pang, Y. *J. Phys. Chem. C* **2015**, *119*, 23285–23291.

[33] Klajn, R.; Stoddart, J. F.; Grzybowski, B. A. *Chem. Soc. Rev.* **2010**, *39*, 2203–2237.

[34] Evans, S. D.; Johnson, S. R.; Ringsdorf, H.; Williams, L. M.; Wolf, H. *Langmuir* **1998**, *14*, 6436–6440.

[35] Zhang, J.; Whitesell, J. K.; Fox, M. A. *Chem. Mater.* **2001**, *13*, 2323–2331.

[36] Manna, A.; Chen, P.-L.; Akiyama, H.; Wei, T.-X.; Tamada, K.; Knoll, W. *Chem. Mater.* **2003**, *15*, 20–28.

[37] Yoon, J. H.; Yoon, S. *Phys. Chem. Chem. Phys.* **2011**, *13*, 12900–12905.

[38] Zep, A.; Wojcik, M. M.; Lewandowski, W.; Sitkowska, K.; Prominski, A.; Mieczkowski, J.; Pociecha, D.; Gorecka, E. *Angew. Chem. Int. Ed.* **2014**, *53*, 13725–13728.

[39] Köhntopp, A.; Dabrowski, A.; Malicki, M.; Temps, F. *Chem. Commun.* **2014**, *50*, 10105–10107.

[40] Moldt, T.; Brete, D.; Przyrembel, D.; Das, S.; Goldman, J. R.; Kundu, P. K.; Gahl, C.; Klajn, R.; Weinelt, M. *Langmuir* **2015**, *31*, 1048–1057.

[41] Quick, M.; Dobryakov, A. L.; Gerecke, M.; Richter, C.; Berndt, F.; Ioffe, I. N.; Granovsky, A. A.; Mahrwald, R.; Ernsting, N. P.; Kovalenko, S. A. *J. Phys. Chem. B* **2014**, *118*, 8756–8771.

[42] Satzger, H.; Spörlein, S.; Root, C.; Wachtveitl, J.; Zinth, W.; Gilch, P. *Chem. Phys. Lett.* **2003**, *372*, 216–223.

[43] Bahrenburg, J.; Röttger, K.; Siewertsen, R.; Renth, F.; Temps, F. *Photochem. Photobiol. Sci.* **2012**, *11*, 1210–1219.

[44] Poprawa-Smoluch, M.; Baggerman, J.; Zhang, H.; Maas, H. P. A.; De Cola, L.; Brouwer, A. M. *J. Phys. Chem. A* **2006**, *110*, 11926–11937.

[45] Bahrenburg, J.; Renth, F.; Temps, F.; Plamper, F.; Richtering, W. *Phys. Chem. Chem. Phys.* **2014**, *16*, 11549–11554.

[46] Röttger, K.; Wang, S.; Renth, F.; Bahrenburg, J.; Temps, F. *Appl. Phys. B* **2015**, *118*, 185–193.

[47] Bank, D. Untersuchung der ultraschnellen Dynamik von Dispersrot 1 in Polymethylmethacrylat-Filmen und als Farbstoffmonolage auf Quarzglas. Masters Thesis, CAU Kiel, 2015.

[48] Röttger, K.; Siewertsen, R.; Temps, F. *Chem. Phys. Lett.* **2012**, *536*, 140–146.

[49] Röttger, K. Ultrafast Deactivation Dynamics of Structurally Modified and Hydrogen-Bonded DNA and RNA Building Blocks. PhD Thesis, CAU Kiel, 2013.

[50] Ahmadi, T. S.; Logunov, S. L.; El-Sayed, M. A. *J. Phys. Chem.* **1996**, *100*, 8053–8056.

[51] Logunov, S. L.; Ahmadi, T. S.; El-Sayed, M. A.; Khoury, J. T.; Whetten, R. L. *J. Phys. Chem. B* **1997**, *101*, 3713–3719.

[52] Hodak, J. H.; Martini, I.; Hartland, G. V. *J. Phys. Chem. B* **1998**, *102*, 6958–6967.

[53] Chen, Y.; Yang, T.; Pan, H.; Yuan, Y.; Chen, L.; Liu, M.; Zhang, K.; Zhang, S.; Wu, P.; Xu, J. *J. Am. Chem. Soc.* **2014**, *136*, 1686–1689.

6

ULTRAFAST COOLING DYNAMICS GOLD NANOPARTICLES FUNCTIONALIZED WITH AROMATIC LIGANDS

6.1 INTRODUCTION

The dynamics of gold nanoparticles (AuNPs) after photoexcitation have previously been investigated with respect to the deactivation and the influence of the NP environment on the process.[1–7] In general, excited AuNPs relax in a stepwise manner: First, the coherently excited electrons dephase within a few fs to form a non-thermal electron distribution, which then further relaxes via e^--e^- scattering between electrons in the metal lattice or the interfacial orbitals.[1,2] Within a few hundred fs, this forms a hot electron distribution in which the electrons at the Fermi level are equilibrated and possess a collective temperature.[8–10] In the next relaxation step, the hot electrons distribute their energy into vibrational modes via inelastic scattering with phonons or vibrational modes, heating up the lattice and potentially also the ligands. The timescale of the electron-phonon (e^--ph) scattering process typically lies within 1-5 ps and is often referred to as ``hot electron lifetime''.[10,11] In the last phase, the vibrationally excited AuNP system dissipates its energy to the surrounding medium (solvent or solid matrix) within ten up to several hundred picoseconds.

Especially the latter two processes strongly depend on the properties of the investigated system and the surrounding medium. Therefore, the quoted time scales are not exact, but can change in different systems and overlap with each other.[1–3] The hot electron lifetime is strongly modulated by organic ligands adsorbed on the Au surface through the change of i) the electronic heat capacity and ii) electron-phonon coupling magnitude.[4] The electronic heat capacity not only determines the initial electronic temperature after excitation, but also depends on the density of electronic states near the Fermi level. The magnitude of e-ph coupling in the system influences the rate of energy transfer between electrons and phonons and depends on the density of electronic states and also the number and energetic distribution of vibrational modes near the Fermi level. As the density of electronic states is changed upon ligand attachment due to mixing of ligand and lattice states,[12] it is easy to understand that different ligands / surface chemistries influence the hot electron lifetime.

Aruda et al. investigated the difference between aminated and thiolated AuNPs of 4 nm size using femtosecond time-resolved tran-

sient absorption spectroscopy and found considerable differences between the two surface chemistries (anchoring groups), which they attributed mainly to a higher density of states in the thiolated AuNPs compared to aminated particles.[6] Investigation of the hot electron cooling times by transient absorption spectroscopy requires fitting of the transient spectra with a temperature-dependent Mie theory model as proposed by Aruda et al., and based on the works of Rosei et al.,[13] Scaffardi et al.,[14] and Inouye et al.[15] This is necessary to account for the not necessarily linear relationship between the differential absorption ΔA in the region of the plasmon resonance and the electronic temperature T_e after photoexcitation.

In this Chapter, results of the spectroscopic investigation of thiolated AuNPs bearing different head groups are presented. In order to investigate the influence of the heat capacity and the number of vibrational modes of the ligand, we functionalized small AuNPs ($d \approx 4$ nm) with mixed self-assembled monolayers (mSAMs) of decanethiol (C10SH) and alkylthiols with different aromatic head groups. For this purpose, we chose naphthol- and phenanthrol-derivatives, two simple aromatic hydrocarbon systems of different size. The chemical structures of the ligands are depicted in Figure 6.1.

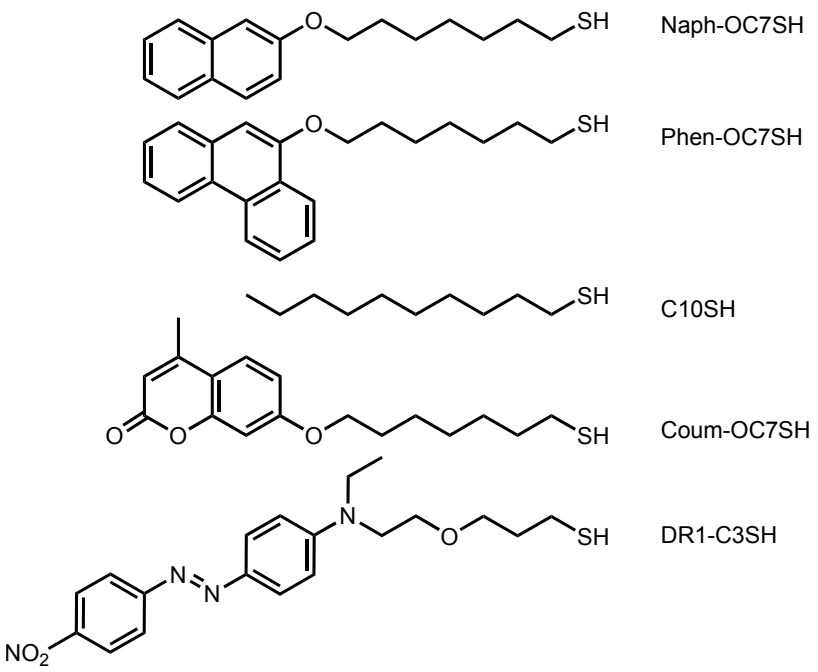

Figure 6.1: Ligands used to functionalize the AuNPs.

Additionally, the possiblity of resonant coupling between the ligand absorption and the Localized Surface Plasmon Resonance (LSPR) band of the AuNP has been investigated. Therefore, the AuNPs were functionalized with Disperse Red 1 (DR-1) and a coumarin-derivative, which possess absorption bands in the near UV and the visible, respectively. To our surprise, fitting the measured femtosecond time-

resolved transient absorption spectra and comparison of the resulting hot electron lifetimes revealed no significant differences for all investigated head groups. These results lead to the conclusion that the influence of the ligand on hot electron lifetimes does not come from the head group, but rather only from the interfacial part of the ligand molecule, i.e. the anchoring thiol group. Coupling between ligand and LSPR has only been observed in the case of the DR-1-functionalized AuNPs, the coumarin absorption band seems to be too far away from the LSPR.

6.2 EXPERIMENTAL SECTION

MATERIALS

The thiolated naphthol- (Naph-OC7SH), phenanthrol- (Phen-OC7SH), and coumarin-derivatives (Coum-OC7SH) were synthesized in a three-step procedure similar to previously described syntheses.[16] The thiol-functionalized Disperse Red 1 (DR1-C3SH) was synthesized by Grace Suana in the Institute of Organic Chemistry of CAU Kiel in the research group of Prof. Herges. Oleylamine-stabilized gold nanoparticles (AuNPs) with a diameter of $\sim$ 4 nm were synthesized through reduction of $HAuCl_4 \cdot 3\ H_2O$ with $NaBH_4$ in the presence of oleylamine and methanol in toluene solution. The obtained AuNPs were then used in a ligand exchange procedure to produce the investigated AuNPs functionalized with mSAMs of plain alkylthiols and aromatically functionalized thiols. A detailed description of the synthesis and characterization of the AuNPs can be found in an earlier publication.[16] To ensure similar particle size distributions, all samples measured under the same conditions came from the same batch of aminated AuNPs. One batch of aminated AuNPs was used to produce decanethiol- (C10AuNPs), naphthol- (Naph-OC7SAuNPs), and phenanthrol-functionalized AuNPs (Phen-OC7SAuNPs). From a second batch, C10SAuNPs, coumarin- (Coum-OC7SAuNPs), and Disperse Red 1-functionalized AuNPs (DR1-C3SAuNPs) were synthesized. Naph-OC7SAuNP and Phen-OC7SAuNPs were synthesized using a ratio of 75 : 25 (aromatic ligand : C10SH), the same ratio is assumed to be present on the AuNP surface. The ratio could not be determined experimentally because the absorption of the ligands lies below $\lambda = 300$ nm, where toluene absorption is strong. Coum-OC7SAuNPs and DR1-C3SAuNPs were synthesized using a ratio of 30 : 70 (aromatic ligand : C10SH). Due to the low solubility of AuNPs bearing higher concentrations of DR1-C3SH, the DR-1 coverage can not be assumed to correspond to the mixing ratio in the ligand exchange procedure. It can only be estimated from the static absorption spectra to be $\sim$ 5% (see Section 6.3.2 for details).

For femtosecond time-resolved transient absorption measurements an excitation wavelength of $\lambda_{pump} = 350$ nm (focus size: 500 µm, 180 nJ) was used. The samples were measured in solution in toluene at optical densities of approximately 0.5 in a flow cell of 1 mm pathlength (see Figures 6.2 and 6.6). The ground state and transient absorption spectra of Naph-OC7SAuNPs, Phen-OC7SAuNPs and the corresponding C10SAuNP sample were fitted with a dielectric constant of the medium of $\epsilon_m = 2.1$, while the spectra of Coum-OC7S-AuNPs, DR1-C3SAuNPs and the corresponding C10SAuNP sample were fitted with $\epsilon_m = 2.25$. Using the dielectric constant of pure toluene ($\epsilon_m = 2.38$) did not give correct fits to the measured absorption spectra, probably because the ligand shell changes the dielectric constant in the immediate vicinity of the Au core.

6.3 RESULTS

6.3.1 NAPHTHOL- AND PHENANTHROL-FUNCTIONALIZED GOLD NANOPARTICLES

The measured static absorption spectra of the C10SAuNP, Naph-OC7S-AuNP and Phen-OC7SAuNP samples are depicted in Figure 6.2.

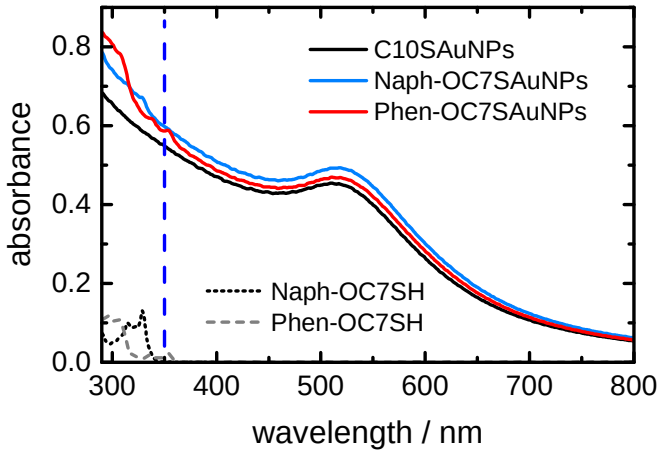

Figure 6.2: Static absorption spectra of AuNPs functionalized with pure C10SH (black), a mSAM of C10SH and Naph-OC7SH (blue), and a mSAM of C10SH and Phen-OC7SH (red). The free ligands Naph-OC7SH (dotted light gray) and Phen-OC7SH (dashed gray) present show no significant absorption at $\lambda_{pump} = 350$ nm (dashed blue).

Additionally, to illustrate the fact that the ligands show no significant absorption at $\lambda_{pump} = 350$ nm (dashed blue line), the absorption spectra of the free ligands Naph-OC7SH and Phen-OC7SH are shown

at low concentrations similar to those present on the AuNPs. It can be safely assumed that in the time-resolved measurements only the AuNP core is excited and the ligands are initially left undisturbed by the excitation pulse.

The measured transient absorption spectra of the C10SAuNPs, Naph-OC7SAuNPs, and Phen-OC7SAuNPs after excitation at $\lambda_{pump} = 350$ nm are shown in the left column of Figure 6.3.

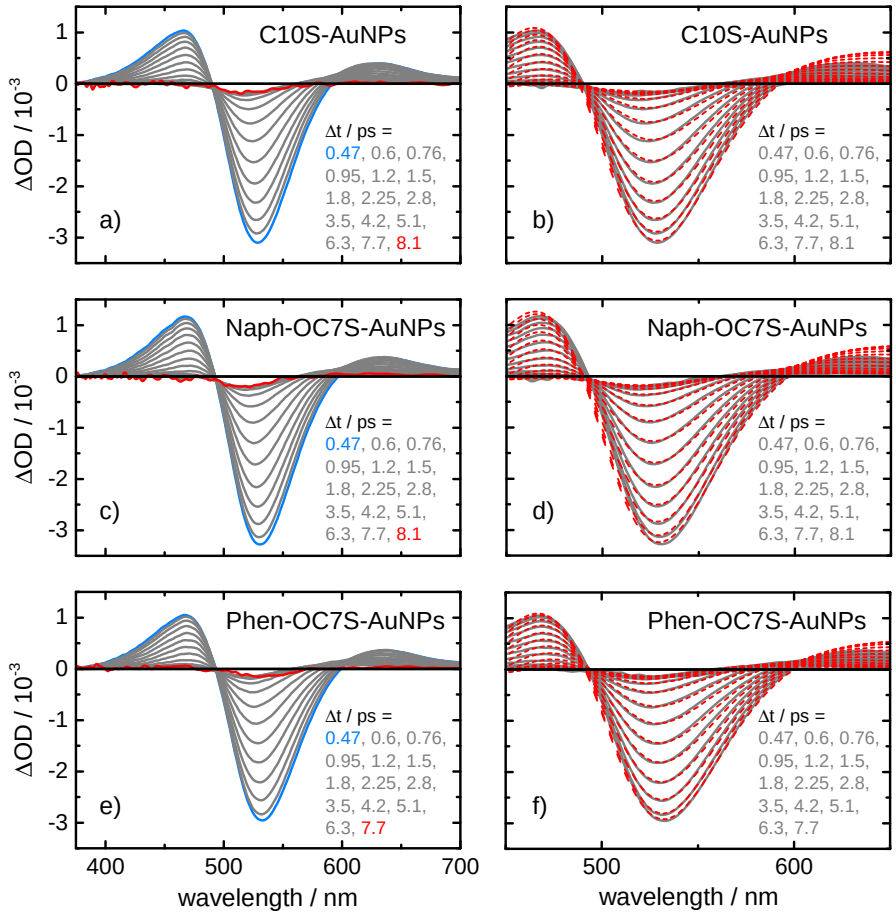

Figure 6.3: Transient absorption spectra of C10SAuNPs (a), Naph-OC7SAuNPs (c), and Phen-OC7SAuNPs (e) and the same respective spectra fitted using temperature-dependent Mie theory, (b), (d), and (f). In the right column measured transient spectra are shown in gray, fits to the spectra in red.

All transient spectra show three absorption bands: A strong bleach at the position of the Localized Surface Plasmon Resonance (LSPR) and positive signals to both sides of the bleach. After excitation, the AuNPs heat up, causing a broadening of the LSPR, which leads to the observed three absorption bands in the transient spectra. No transient signals of the ligands are observed, as these were not excited by the pump pulses. Therefore, the transient spectra of all three samples appear very similar in shape as well as in signal intensity.

To extract the elecronic temperature in the Au core after excitation, the transient spectra were fitted with the temperature-dependent Mie theory model as proposed by Aruda et al.[6] The transient spectra and the respective fits are given in the right column of Figure 6.3, showing good agreement with each other. The electronic temperature in the excited Au core was extracted from these fits and plotted against time after excitation in Figure 6.4. Exponential fits to the temperature-time profiles give the hot electron lifetimes. The resulting relaxation time constants describing the cooling of the hot electrons are:

$$\begin{aligned} \tau_{\text{C10SAuNPs}} &= 2.0 \pm 0.2 \text{ ps} \\ \tau_{\text{Naph-OC7SAuNPs}} &= 1.8 \pm 0.2 \text{ ps} \\ \tau_{\text{Phen-OC7SAuNPs}} &= 2.2 \pm 0.4 \text{ ps} \end{aligned}$$

The given error limits are the 2σ statistical uncertainties of the exponential fit. Earlier delay times (before 0.47 ps) were not fitted to avoid distortion of the results due to incomplete subtraction of solvent signals. Also, the maximum temperature is reached at $\Delta t = 0.6 - 0.7$ ps, which makes fits at earlier delay times unnecessary for the extraction of the hot electron lifetimes.

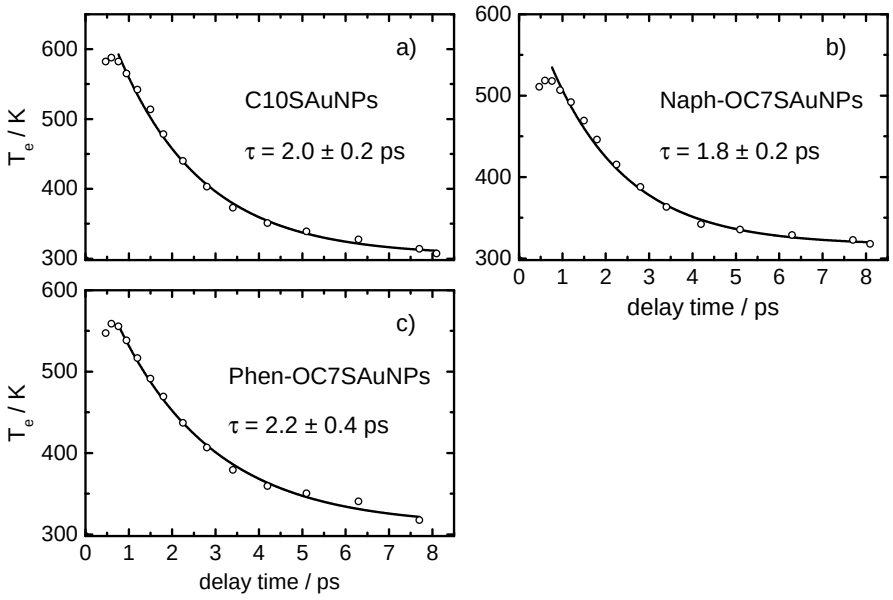

Figure 6.4: Temperature-time profiles of C10SAuNPs (a), Naph-OC7SAuNPs (b), and Phen-OC7SAuNPs (c) with the respective monoexponential fits (solid lines) and the relaxation time constants.

Due to a strong correlation of the electronic temperature and the global scaling factor used in the nonlinear fitting procedure to scale the fitted spectra to the correct intensity, the absolute temperature values in the temperature-time profiles are questionable. With increasing number of fit iterations, this correlation leads to an increasing global

scaling factor and decreasing electronic temperatures without any improvement of the fits to the transient spectra. This behaviour is illustrated in Figure 6.5, where fits to the transient spectra of C10SAuNP and the respective temperature-time profiles are shown for 20, 40 and 60 performed iterations. The quality of the fits is not improved over time and the extracted cooling dynamics are the same for all three fitting results. As the computing time for 60 iterations was very long the procedure was stopped after 40 iterations for Naph-OC7SAuNPs and Phen-OC7SAuNPs to reduce the fitting times. All results shown in Figures 6.3 and 6.4 in this Section are for 40 iterations.

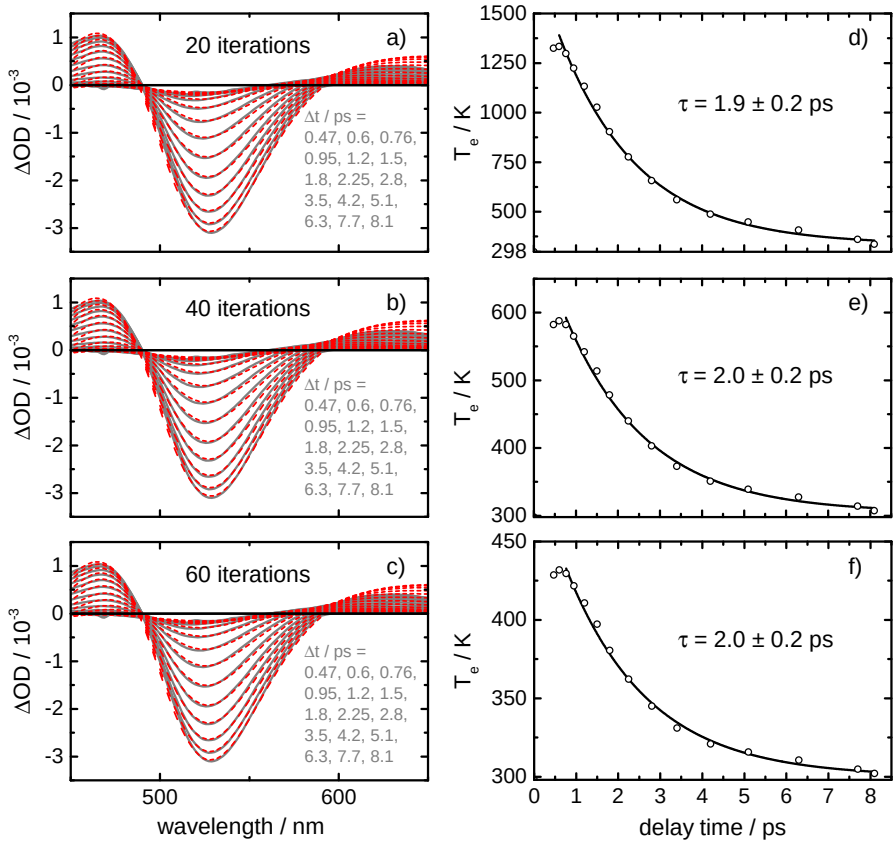

Figure 6.5: Transient spectra (gray) and temperature-dependent Mie theory fits (red) for C10SAuNPs and the respective temperature-time profiles using 20 iterations, (a) and (d), 40 iterations, (b) and (e), and 60 iterations, (c) and (f). The quality of the fits and the extracted hot electron lifetimes do not change with increasing number of iterations.

6.3.2 COUMARIN- AND DISPERSE RED 1-FUNCTIONALIZED GOLD NANOPARTICLES

The static absorption spectra of C10SAuNPs, coumarin- (Coum-OC7S-AuNPs), and Disperse Red 1-functionalized AuNPs (DR1-C3SAuNPs) are depicted in Figure 6.6a. The optical density at the excitation wavelength $\lambda_{pump} = 350$ nm is approximately the same for all three samples. The absorption spectra of the free ligands Coum-OC7SH and DR1-C3SH are shown to illustrate that the ligands are not or only to a very small part excited by the pump pulse. The $\pi\pi^*$ absorption band of DR1-C3SH is located at $\lambda_{max} = 470$ nm, very close to the LSPR of AuNPs at $\lambda_{LSPR} = 518$ nm, which leads to a change of the apparent width of the LSPR in DR1-C3SAuNPs. To estimate the AuNP concentration in the DR1-C3SAuNP sample the C10SAuNP spectrum was scaled to fit the red side of the absorption spectrum, as shown in Figure 6.6b. The inset shows the difference between the measured and the calculated spectrum which corresponds to the pure DR-1 absorbance in the DR1-C3SAuNP sample. The absolute number of ~ 11 DR-1 molecules per AuNP was calculated using the extinction coefficient of DR-1, $\epsilon_{DR1}(470\,nm) = 3.6 \cdot 10^5\,L \cdot mol^{-1} \cdot cm^{-1}$, and the extinction coefficient of AuNPs with d $\approx$ 4 nm, $\epsilon_{AuNPs} = 4.58 \cdot 10^6\,L \cdot mol^{-1} \cdot cm^{-1}$. Assuming a thiol footprint of ~ 22 Å^2,[17] the surface area of one AuNP (5000 Å^2) provides space for 225 molecules. The calculated number of 11 DR-1 ligands per AuNP thus corresponds to an estimated DR-1 coverage of ~ 5 %.

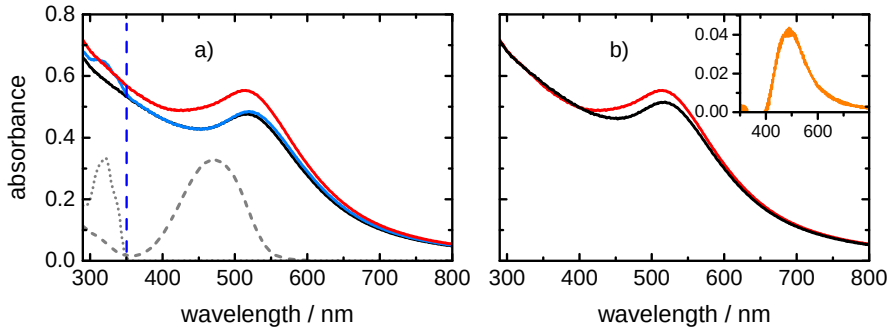

Figure 6.6: (a) Static absorption spectra AuNPs functionalized with pure C10SH (solid black), a mSAM of C10SH and Coum-OC7SH (solid blue), and a mSAM of C10SH and DR1-C3SH (solid red). The free ligands Coum-OC7SH (dotted gray) and DR1-OC3SH (dashed gray) show no or only very small absorption at $\lambda_{pump} = 350$ nm (dashed blue). (b) Measured absorption spectrum of DR1-C3SAuNPs (red) and absorption spectrum of C10SAuNPs (black) scaled to match the absorbance in the red part of the spectrum ($\lambda \leqslant 650$ nm). The inset shows the difference between both spectra and resembles the pure DR-1 absorbance in the DR1-C3SAuNP sample.

Figure 6.7 shows the measured transient absorption spectra of C10S-AuNPs, Coum-OC7SAuNPs and DR1-C3SAuNPs after excitation at $\lambda_{pump} = 350$ nm and the respective temperature-dependent Mie theory fits to the transient spectra.

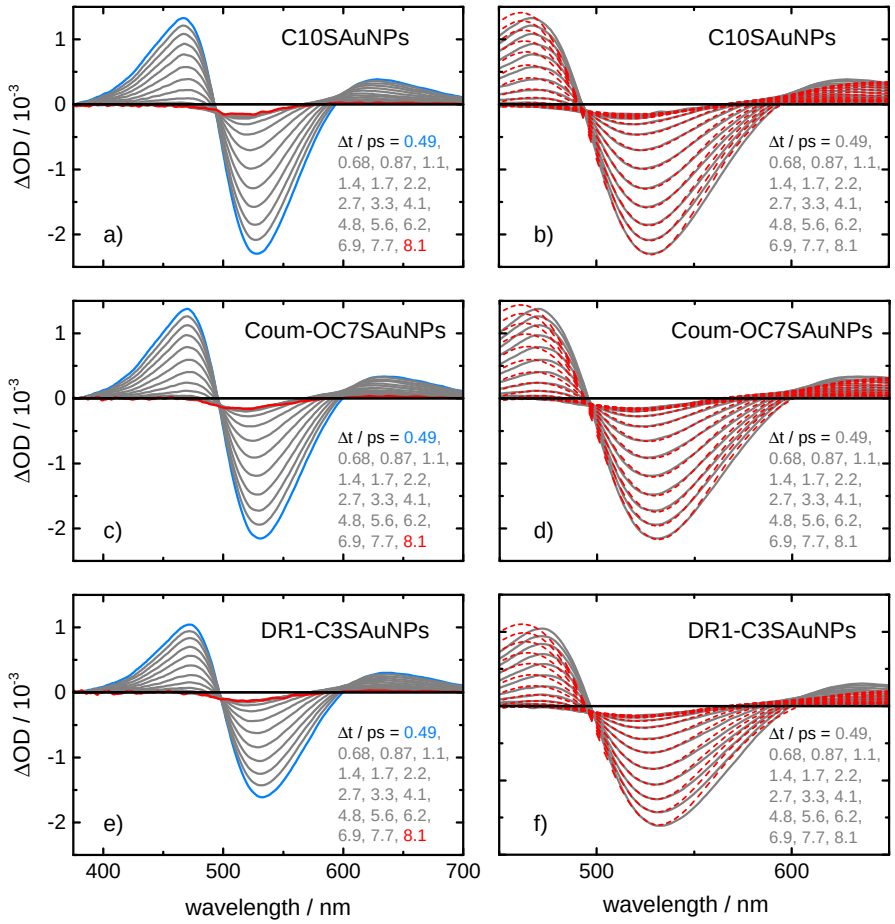

Figure 6.7: Measured transient absorption spectra of (a) C10SAuNPs, (c) Coum-OC7SAuNPs, and (e) DR1-C3SAuNPs and the same respective spectra fitted using the temperature-dependent Mie theory model ((b), (d) and (f)). In the right column the measured spectra are shown in gray and the fits in red. In case of DR1-C3SAuNPs the fit using the scaled C10SAuNP spectrum for determination of the ground state parameters is depicted. The fit using the measured DR1-C3SAuNPs spectrum is very similar in quality and therefore omitted.

The three absorption bands arising from the broadening of the LSPR are visible in all transient spectra, while no strong ligand-specific signals are observed. The signal intensities are very similar for C10SAuNPs and Coum-OC7AuNPs, whereas the intensity of the bleaching signal in the DR1-C3SAuNP spectra is reduced by ~ 30% compared to the other spectra.

To model the transient spectra with the temperature-dependent Mie theory model, the ground state absorption spectra have to be

fitted first to obtain parameters describing the LSPR in the ground state. Due to the distortion of the LSPR in the DR1-C3SAuNP spectrum the parameters obtained from fitting the measured spectrum do not reflect the real AuNP properties, thus the scaled C10S-AuNP spectrum shown in Figure 6.6b) was used for this purpose. The ground state parameters of all samples are summarized in Table 6.1, for comparison the values for both the measured and the calculated ground state spectrum of DR1-C3SAuNPs are given. The fitting parameters are the width parameters for the absorption bands of the free and the bound electrons in the AuNP core, γ_{free} and γ_{bound}. (For a detailed explanation of the fitting functions and parameters see Chapter 2.)

sample	γ_{free} /10^{15} Hz	γ_{bound} /10^{14} Hz
C10SAuNPs	1.067 ± 0.006	5.224 ± 0.02
Coum-OC7SAuNPs	1.099 ± 0.006	4.896 ± 0.021
DR1-C3SAuNPs meas.	0.993 ± 0.011	5.341 ± 0.038
DR1-C3SAuNPs calc.	1.069 ± 0.006	5.238 ± 0.022

Table 6.1: Fit parameters for the ground state absorption spectra of C10SAuNPs, Coum-OC7SAuNPs, DR1-C3SAuNPs as measured and DR1-C3SAuNP as calculated using the scaled C10SAuNP spectrum. γ_{free} is the width parameter for the intraband transitions, γ_{bound} the width parameter for the interband transitions.

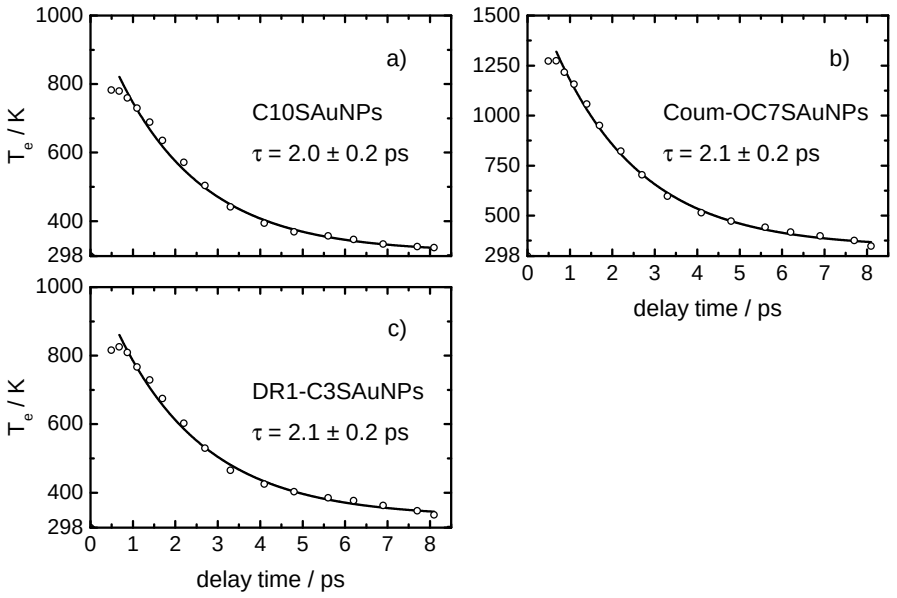

Figure 6.8: Temperature-time profiles of (a) C10SAuNPs, (b) Coum-OC7SAuNPs, and (c) DR1-C3SAuNPs with monoexponential fits (solid line) and the resulting time constants. The given error limits are the 2σ statistical uncertainties of the exponential fit.

Plots of the electronic temperature against delay time lead to the temperature-time profiles shown in Figure 6.8. The absolute temper-

ature values therein are questionable for the same reasons quoted for the data in section 6.3.1. To ensure the validity of the extracted dynamics, the results of fitting procedures with 25 and 50 iterations were compared. The fits shown here are for 25 iterations, as no further improvement was visible at longer iteration times. The resulting decay constants of monoexponential fits to the temperature-time profiles are:

$$\begin{aligned} \tau_{\text{C10SAuNPs}} &= 2.0 \pm 0.2 \text{ ps} \\ \tau_{\text{Coum-OC7SAuNPs}} &= 2.1 \pm 0.2 \text{ ps} \\ \tau_{\text{DR1-C3SAuNPs}} &= 2.1 \pm 0.2 \text{ ps} \end{aligned}$$

6.4 DISCUSSION

As only the Au cores and not the ligands were excited in the above experiments, the recorded transient spectra only show signals of the AuNPs themselves. However, in the spectra of DR1-C3SAuNPs an influence of the ligand onto the signal intensity can be suspected. A decreased signal intensity of the bleach and the positive wing in the UV cannot be explained by different measurement conditions, as all samples were measured directly after one another. The same excitation power and approximately the same AuNP concentration were used in all time-resolved measurements. Therefore, it is valid to assume the same number of absorbed photons per AuNP, $\langle N \rangle \approx 2$, in all cases. In another set of measurements, signal intensity changes in DR-1-functionalized systems have been observed after excitation with $\lambda_{\text{pump}} = 467$ nm light, which excites both ligand and Au core (see Chapter 5). In that study, the changed intensities could not easily be accounted for by superimposed positive DR-1 signals, but hint at stronger coupling of the Au core and DR-1 ligand. The repeated observation of decreased signal intensities is evidence for the existence of an interaction between DR-1 and the AuNP. Classification of the nature of these interactions is difficult based on the present results, but a resonance effect of the close-lying $\pi\pi^*$ band of DR-1 and the LSPR of the AuNP may be suspected. Similar effects have been described in literature.[18–21]

The temperature-time profiles give very similar time constants for all AuNP samples. They are the same within the error limits not only for samples from the same batch of synthesis, which were measured on the same day, but for all examined samples (see Table 6.2). An assignment of the time constants to the electron-phonon scattering process (``hot electron lifetime´´) is supported by literature reports, which give a time scale of ~ 1-5 ps for this process.[2,6,10,11] Furthermore, the results are in agreement with measurements on AuNPs functionalized with alkylthiols, where $\tau_{\text{e-ph}} = 2.3$ ps was found (Chapter 4). In contrast to the influence of the anchoring group on the electron cool-

Batch 1	$\tau_{e\text{-}ph}$ / ps	Batch 2	$\tau_{e\text{-}ph}$ / ps
C10SAuNPs	2.0 ± 0.2	C10SAuNPs	2.0 ± 0.2
Naph-OC7SAuNPs	1.8 ± 0.2	Coum-OC7SAuNPs	2.1 ± 0.2
Phen-OC7SAuNPs	2.2 ± 0.4	DR1-C3SAuNPs	2.1 ± 0.2

Table 6.2: Electron-phonon scattering time constants of C10SAuNPs, Naph-OC7SAuNPs, Phen-OC7SAuNPs, Coum-OC7SAuNPs, and DR1-C3SAuNPs obtained from monoexponential fits to the temperature-time profiles.

ing dynamics reported by Aruda and coworkers,[6] an effect of the head group cannot be inferred from the results presented here. Based on experimental and theoretical results the authors of the aforementioned study stated that the higher density of states near the Fermi level in thiolated AuNPs is responsible for decelerated hot electron cooling dynamics. From our results, we can conclude that the density of states is unaltered upon exchange of the head group and no influence of the ligand on the cooling dynamics is visible, at least as long as only the Au core is excited. Examining the effect of simultaneous excitation of ligand and AuNP would be an interesting aim in future studies.

6.5 CONCLUSION

Small gold nanoparticles ($d \approx 4$ nm) functionalized with decanethiol and a mixed self-assembled monolayer of decanethiol and different aromatic thiols, i.e. naphthol, phenanthrol, coumarin and Disperse Red 1 derivatives, have been synthesized. The samples were investigated using femtosecond time-resolved transient absorption spectroscopy with an excitation wavelength of $\lambda_{ex} = 350$ nm. The recorded transient absorption spectra were subsequently fitted with a temperature-dependent Mie theory model to extract the electronic temperature T_e and compare the hot electron cooling dynamics as a function of the different aromatic head groups in the nanoparticle ligand shell. Very similar electron cooling dynamics were found for all investigated samples, leading to the conclusion that the head groups of the ligands do not influence the dynamics as long as they are not excited simultaneously with the AuNP. The density of electronic states near the Fermi level seems to be unaltered by the different ligands. Weak resonant coupling between LSPR and ligand was found in case of the Disperse Red 1-functionalized AuNPs, whereas none could be observed in coumarin-functionalized AuNPs. The coupling has no detectable influence on the hot electron lifetimes.

BIBLIOGRAPHY

[1] Hartland, G. V. *Chem. Rev.* **2011**, *111*, 3858–3887.

[2] Link, S.; El-Sayed, M. A. *J. Phys. Chem. B* **1999**, *103*, 8410–8426.

[3] Link, S.; El-Sayed, M. A. *Int. Rev. Phys. Chem.* **2000**, *19*, 409–453.

[4] Aruda, K. O.; Tagliazucchi, M.; Sweeney, C. M.; Hannah, D. C.; Weiss, E. A. *Phys. Chem. Chem. Phys.* **2013**, *15*, 7441–7449.

[5] Yau, S. H.; Varnavski, O.; Goodson, T. *Acc. Chem. Res.* **2013**, *46*, 1506–1516.

[6] Aruda, K. O.; Tagliazucchi, M.; Sweeney, C. M.; Hannah, D. C.; Schatz, G. C.; Weiss, E. A. *Proc. Nat. Acad. Sci. U.S.A.* **2013**, *110*, 4212–4217.

[7] Busby, M.; Chiorboli, C.; Scandola, F. *J. Phys. Chem. B* **2006**, *110*, 6020–6026.

[8] Ahmadi, T. S.; Logunov, S. L.; El-Sayed, M. A. *J. Phys. Chem.* **1996**, *100*, 8053–8056.

[9] Logunov, S. L.; Ahmadi, T. S.; El-Sayed, M. A.; Khoury, J. T.; Whetten, R. L. *J. Phys. Chem. B* **1997**, *101*, 3713–3719.

[10] Hodak, J. H.; Martini, I.; Hartland, G. V. *J. Phys. Chem. B* **1998**, *102*, 6958–6967.

[11] Voisin, C.; Fatti, N. D.; Christofilos, D.; Vallée, F. *J. Phys. Chem. B* **2001**, *105*, 2264–2280.

[12] Goldmann, C.; Lazzari, R.; Paquez, X.; Boissière, C.; Ribot, F.; Sanchez, C.; Chanéac, C.; Portehault, D. *ACS Nano* **2015**, *9*, 7572–7582.

[13] Rosei, R.; Antonangeli, F.; Grassano, U. M. *Surf. Sci.* **1973**, *37*, 689–699.

[14] Scaffardi, L. B.; Tocho, J. O. *Nanotechnology* **2006**, *17*, 1309–1315.

[15] Inouye, H.; Tanaka, K.; Tanahashi, I.; Hirao, K. *Phys. Rev. B* **1998**, *57*, 11334–11340.

[16] Köhntopp, A.; Dabrowski, A.; Malicki, M.; Temps, F. *Chem. Commun.* **2014**, *50*, 10105–10107.

[17] Schreiber, F. *Prog. Surf. Sci.* **2000**, *65*, 151 – 257.

[18] Haes, A. J.; Zou, S.; Zhao, J.; Schatz, G. C.; Van Duyne, R. P. *J. Am. Chem. Soc.* **2006**, *128*, 10905–10914.

[19] Zhao, J.; Jensen, L.; Sung, J.; Zou, S.; Schatz, G. C.; Van Duyne, R. P. *J. Am. Chem. Soc.* **2007**, *129*, 7647–7656.

[20] Wurtz, G. A.; Evans, P. R.; Hendren, W.; Atkinson, R.; Dickson, W.; Pollard, R. J.; Zayats, A. V.; Harrison, W.; Bower, C. *Nano Lett.* **2007**, *7*, 1297–1303.

[21] Debnath, T.; Dana, J.; Maity, P.; Lobo, H.; Shankarling, G. S.; Ghosh, H. N. *Chem. Eur. J.* **2015**, *21*, 5704–5708.

Part III

CONCLUDING DISCUSSION

7 SUMMARY AND OUTLOOK

As many applications exploit not only the properties of the ligands, but more and more rely on the characteristic features of AuNPs and their conjunction with the ligands, investigations of their interplay by time-resolved spectroscopies are of great importance. In applications of functionalized AuNPs these complex interactions may prevent the desired function of the system, but they can also create completely new ways for the rational design of smart and possibly photoresponsive materials.

The first goal of this Thesis was the investigation of the photoisomerization and the ultrafast molecular dynamics of azobenzene (AB) and Disperse Red 1 (DR-1) on gold nanoparticle (AuNP) surfaces. The constraints exerted onto the photochromic molecular switch by the close proximity to metallic AuNPs may affect the photoisomerization process or even prevent it altogether. Energy transfer processes leading to quenching of excited states and steric hindrance impeding molecular motion are considered the main reasons for reduced photoisomerization efficiencies in self-assembled monolayers (SAMs) on metal surfaces. Additionally, nanoparticles involve the potential risk of irreversible aggregation when the ligand shell properties change during isomerization. The second part of the Thesis was concerned with the effect of functionalization on the ultrafast dynamics of the AuNP itself. For this purpose AuNPs functionalized with a number of ligands with different electronic and photophysical properties were investigated. The complex relaxation process of AuNPs after excitation is influenced by the refractive index of the surrounding medium, the AuNP size, the excitation energy and the nature and electronic structure of the ligand shell.

The aim of Thesis was the elucidation of important interactions between photochromic switches and gold nanoparticles and their influence on the photoresponsivity of such complex hybrid systems.

7.1 SUMMARY

PHOTOISOMERIZATION OF AZOBENZENE ON GOLD NANOPARTICLES

The isomerization properties of small gold nanoparticles functionalized with a mixed self-assembled monolayer (mSAM) containing azobenzenethiols and simple alkylthiols were investigated. Azoben-

zene ligands with different linker chain lengths were used to adjust the distance between chromophore and AuNP, see Figure 7.1.

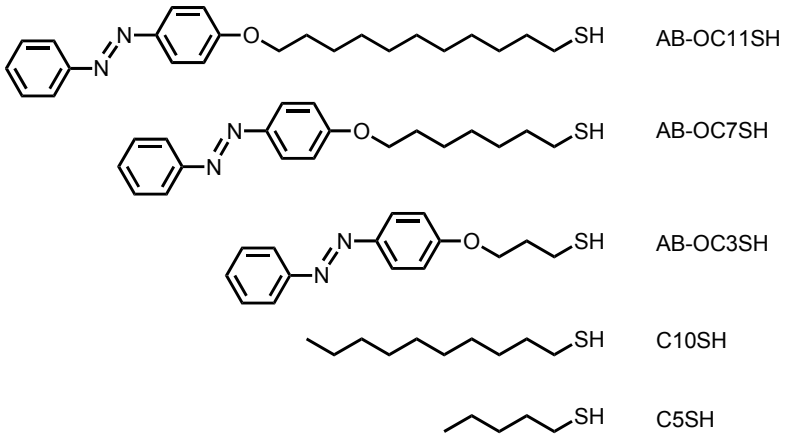

Figure 7.1: Structures of the AB ligands with different linker chain lengths.

The functionalized AuNPs show excellent photoswitching capabilities, multiple *trans-cis* and subsequent *cis-trans* isomerization cycles without significant signs of degradation could be performed for all examined samples. The photostationary states (PSSs) after illumination at $\lambda = 365$ nm and 455 nm, respectively, show high conversion rates: For the longest linker chain (C11) in combination with decanethiol (C10SH) as coligand the PSS365 reaches *cis*:*trans* = 95 % : 5 %, the back isomerization to PSS455 has a conversion rate of *cis*:*trans* = 25 % : 75 %. For very short linker chains (C3), steric or electronic hindrance is observed, which is reflected in the conversion rates of *cis*:*trans* = 70 % : 30 % and *cis*:*trans* = 10 % : 90 % in PSS365 and PSS455, respectively.

In addition to photoisomerization of the AB moiety, reversible aggregation of AuNPs was observed for systems that combine longer linker chain lengths (C7 and C11) with short-chain coligands (C5SH), as schematically shown in Figure 7.2.

Upon conversion of the AB unit to its *cis* form the particles aggregate, visible by a red-shift and broadening of the Localized Surface Plasmon Resonance (LSPR) band in the UV/Vis spectra. Weaker solvent stabilization of *cis*-AuNPs in nonpolar toluene and an enhanced dipole-dipole attraction between particles are the main driving forces for the aggregation. Illumination with $\lambda = 455$ nm light induces *cis-trans* isomerization of the AB moiety and causes the particles to disaggregate again. In this fashion, the particles can repeatedly be switched between the aggregated and non-aggregated state, i.e. the aggregation is fully photoreversible. The strength of aggregation depends on the AB surface coverage, however no precipitation of aggregates is observed even at high AB concentrations of ~ 70 %.

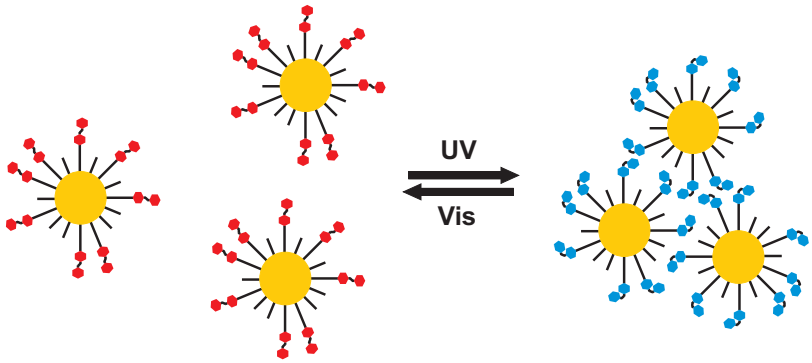

Figure 7.2: Scheme of the reversible photo-induced aggregation of AB-functionalized AuNPs.

DYNAMICS OF AZOBENZENE SWITCHES ON GOLD NANOPARTICLES

To elucidate the interaction between AB and AuNP, femtosecond time-resolved transient absorption spectra of AuNPs functionalized with decanethiol and a mSAM of decanethiol and AB-OC11SH were recorded. The samples were excited at $\lambda = 357$ nm, which simultaneously excites the LSPR and interband transitions of the AuNPs and the AB moiety within its $\pi\pi^*$ band. Fitting of the transient spectra with Lorentzians revealed an excited state absorption (ESA) band of AB around $\lambda = 400$ nm decaying with two time constants of

$$\begin{aligned} \tau_{AB1,AuNP} &= 1.2 \pm 0.2 \text{ ps}, \\ \tau_{AB2,AuNP} &= 4.7 \pm 1.1 \text{ ps}. \end{aligned}$$

The position and the temporal evolution of the band showed only minor differences to the AB dynamics in solution where two time constants are found as well:

$$\begin{aligned} \tau_{AB1,solution} &= 2.0 \pm 0.1 \text{ ps} \\ \tau_{AB2,solution} &= 5.1 \pm 0.4 \text{ ps} \end{aligned}$$

The similarity of the dynamics in the two different environments is further underlined by the amplitude-weighted mean lifetimes of AB on the AuNPs, $\bar{\tau}_{AuNPs} = 2.3 \pm 0.5$ ps, and in solution, $\bar{\tau}_{solution} = 2.7 \pm 0.2$ ps, which again are very similar. In comparison, the transient signals of the LSPR originating from the AuNP itself have a considerably shorter lifetime of $\tau_{LSPR} = 1.5 \pm 0.2$ ps.

The transient spectra of AB-functionalized AuNPs cannot be reconstructed by a simple superposition of the spectra of free AB-OC11SH

and decanethiol-functionalized AuNPs. In conclusion, the data points towards an interaction between AB and AuNP during the excitation (pump) pulse and afterwards the long alkyl linker chain (C11) efficiently decouples the chromophore and the Au core electronically.

To further investigate the interactions in chromophore-AuNP systems, we examined AuNP functionalized with the *push-pull* azobenzene derivative Disperse Red 1 (DR-1). DR-1 exhibits large transient absorption signals, much larger than AB, and the ultrafast dynamics in solution and in more restriced environments are well investigated. The chemical structures of the DR-1 ligand and decanethiol which is used as the coligand in the mSAMs are given in Figure 7.3.

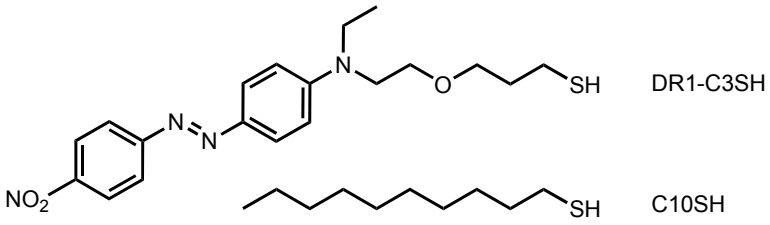

Figure 7.3: Chemical structures of thiol-functionalized DR-1 and decanethiol.

In the DR-1-functionalized AuNPs, evidence for coupling between AuNP and DR-1 ligand is discovered: (i) The pure DR-1 absorption spectrum in the DR-1-functionalized AuNP sample was calculated from the static absorption spectra. The absorption band is blue-shifted by 10 nm compared to free DR-1 in solution. (ii) The DR-1-functionalized AuNPs were compared to purely decanethiol-functionalized AuNPs using transient absorption spectroscopy. The transient spectra were measured after excitation with $\lambda = 467$ nm, which excites both the AuNP and the DR-1 ligand. The data show the same general spectral shape for both samples, no absorption band arising purely from the DR-1 ligand can be identified. However, the transient signal intensities are considerably changed over the whole wavelength range when DR-1 is attached to the AuNPs. As with the AB-functionalized AuNPs, the transient DR1-AuNP spectra cannot be calculated as a superposition of the spectra of alkylated AuNPs and free DR-1. (iii) Long-lived DR-1 product signals that are visible for free DR-1 are absent, indicating that either the *cis* form rapidly isomerizes back or no product is formed at all.

Resonant coupling of the $\pi\pi^*$ band of DR-1 and the LSPR of the AuNPs within the duration of the excitation pulse, which causes an energy and charge transfer from the AuNP to the ligand may be able to explain the observed effects. The subsequent change in the chromophores electronic structure could lead to the observed dramatic intensity differences in the transient spectra.

The excitation of chromophores on AuNPs by UV or visible light inevitably leads to the simultaneous excitation of the AuNP itself. The relaxation processes of excited AuNPs are quite complex and can provide information about the interaction between ligand and substrate. Consequentially, the ultrafast dynamics of the Au core itself have been investigated by transient absorption spectroscopy. The AuNP relaxation after laser excitation proceeds stepwise and each of the four relaxation processes, which comprise the dephasing of coherently excited electrons, electron-electron scattering, electron-phonon scattering, and phonon-phonon coupling, occurs on a certain timescale. The electron-electron scattering process, also termed hot electron cooling, occurs within 1-5 ps, a timescale readily accessible with our setup. Therefore, we concentrated on the analysis of this process and investigated the influence of the ligands head group onto the hot electron cooling dynamics in the Au core.

AB-functionalized AuNPs have been compared with purely decanethiol-functionalized AuNPs and a temperature-dependent Mie theory model was used to fit the transient absorption spectra of both species. This analysis allowed for the determination of the electronic temperature T_e at different delay times after excitation. The identified hot electron lifetimes in both samples

$$\begin{aligned} \tau_{\text{decanethiol}} &= 2.3 \pm 0.1 \text{ ps} \\ \tau_{\text{AB}} &= 2.0 \pm 0.3 \text{ ps} \end{aligned}$$

are very similar and in agreement with literature values for thiolated AuNPs of the same size. The hot electron cooling lifetime strongly depends on the size of the AuNP, excitation energy, surrounding medium and the electronic density of states near the Fermi level in the Au core. The first three factors are the same for the alkylated and the AB-functionalized AuNPs, therefore the electronic density of states is the only influencing factor on the dynamics in this case. The similarity of the electron cooling dynamics in both the alkylated and the AB-functionalized AuNPs indicates that the density of states is not significantly altered upon AB attachment.

To further investigate a possible influence of the ligand head group on the hot electron cooling dynamics, we functionalized AuNPs with ligands bearing aromatic head groups of different size and with different photochemical properties. The chemical structures of the ligands are shown in Figure 7.4. Two purely aromatical head groups of different size, naphthol and phenanthrol, were chosen to shed light on

the role of the ligands heat capacity, which has been discussed as an influencing factor in the literature. Furthermore, two chromophores, a highly fluorescent coumarin derivative and photochromic Disperse Red 1, were brought onto the AuNP surface to investigate the influence of possible resonant coupling between LSPR and the ligand absorption band.

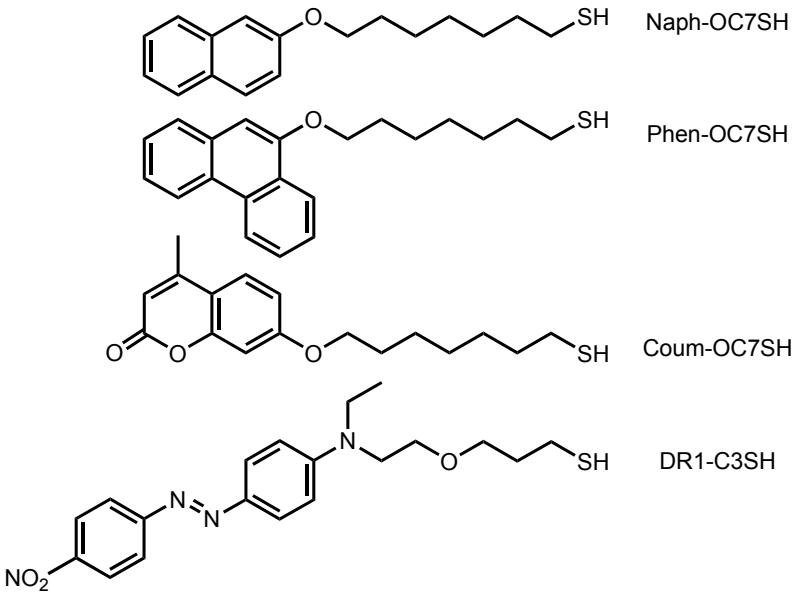

Figure 7.4: Aromatic ligands used to functionalize the AuNPs.

Transient absorption spectra of AuNPs functionalized with only decanethiol and with mSAMs of decanethiol and the ligands shown in Figure 7.4 were recorded after excitation at $\lambda = 350$ nm. At this wavelength only the AuNP absorbs, the ligands are not excited. The extracted hot electron lifetimes are given in Table 7.1, therein batch 1 and 2 denote different batches of AuNP synthesis and transient absorption measurement.

Batch 1	$\tau_{e\text{-}ph}$ / ps	Batch 2	$\tau_{e\text{-}ph}$ / ps
C10SAuNPs	2.0 ± 0.2	C10SAuNPs	2.0 ± 0.2
Naph-OC7SAuNPs	1.8 ± 0.2	Coum-OC7SAuNPs	2.1 ± 0.2
Phen-OC7SAuNPs	2.2 ± 0.4	DR1-C3SAuNPs	2.1 ± 0.2

Table 7.1: Hot electron lifetimes of C10SAuNPs, Naph-OC7SAuNPs, Phen-OC7SAuNPs, Coum-OC7SAuNPs, and DR1-C3SAuNPs. Batch 1 and 2 denote different batches of AuNP synthesis and time-resolved measurement.

With batch 1, we investigated the influence of the ligands heat capacity on the hot electron lifetime. The time constants for the naphthol- and phenanthrol-functionalized AuNPs are the same within the error margins, demonstrating that the heat capacity of the ligand

head group does not influence the hot electron cooling dynamics, at least as long as only the AuNP is excited. With batch 2, we investigated the influence of possible coupling between LSPR and ligand absorption bands. Coum-OC7SH has an absorption band at $\lambda_{max} = 330$ nm, and DR1-OC3SH absorbs at $\lambda_{max} = 470$ nm, much closer to the LSPR maximum at $\lambda_{LSPR} = 510$ nm. Weak coupling between ligand and LSPR is observed in the DR-1-functionalized AuNPs, but not in the coumarin-functionalized ones. The coupling becomes visible through changed signal intensities in the transient absorption spectra, especially pronounced in the LSPR region. However, the same hot electron lifetimes are found for all samples in batch 2, hence the electron cooling dynamics are not affected. In summary, the ligand head group has no influence on the hot electron cooling dynamics, neither through a larger heat capacity nor through weak resonant coupling with the LSPR - at least as long as the ligand is not excited simultaneously with the AuNP.

7.2 OUTLOOK

The results presented in this Thesis initiated a number of ongoing and future investigations regarding functionalized AuNPs in our group. The transient absorption signals arising from the AuNP itself are very large compared with the signals of plain AB. A reduction of the AuNP size would decrease the LSPR intensity and thus the transient signals resulting from it. Subsequently, smaller AuNPs would allow for a clearer interpretation of the molecular dynamics of the ligand. Recently, AB-functionalized AuNPs with a diameter of ~ 2 nm were synthesized as part of a B.Sc. project (E. Moshake, CAU Kiel). First transient absorption measurements on the new AuNPs showed very promising results such that the project will be pursued further.

Variation of the distance between chromophore and AuNP will shed light onto the nature of the interaction, which leads to reduced *trans*-to-*cis* conversion rates in systems with very short linker chain lengths. As the necessary AB compounds are readily available and synthesis of the respective functionalized AuNPs has already been optimized, transient absorption measurements could be started directly.

The presently available results on the dynamics of Disperse Red 1-functionalized AuNPs strongly indicated coupling between the ligand and LSPR of the AuNP. Further investigations on systems bearing higher DR-1 surface coverages could clarify the nature of the interaction and illuminate the DR-1 dynamics on the AuNP surface. For this purpose, new transient absorption measurements with excitation at $\lambda \approx 465$ nm are necessary, in which the scattered pump light is reduced so that the whole spectral region can be analyzed.

The results presented in this Thesis indicate that the ligand head group has practically no influence on the hot electron cooling dynamics as long as it is not excited by the pump pulses. Additional experiments in which ligand and AuNP are excited simultaneously could provide more conclusive proof for the head group-independent behaviour of the Au core. The already synthesized coumarin-functionalized AuNPs are ideal candidates for this type of study, as they exhibit a coumarin absorption band in the near UV ($\lambda \approx 330$ nm), which is easily accessible with our experimental setup, but show no indications of coupling between ligand and LSPR.

Finally, a number of yet unexplored molecular switches, e.g. spiropyrans, diarylethenes, and fulgides, could be investigated on the gold nanoparticle surface using different ultrafast spectroscopy techniques available in our laboratory. Investigation of spiropyran-functionalized AuNPs in collaboration with the group of R. Klajn from the Weizmann institute, Israel, is already planned.

DANKSAGUNG

An erster Stelle möchte ich mich ganz herzlich bei meinem Doktorvater Prof. Friedrich Temps für die wertvolle Unterstützung und engagierte Betreuung während der letzten Jahre bedanken. Sein stetes Interesse an allen Aspekten der wissenschaftlichen Arbeit und seine große Hilfsbereitschaft und Motivation bei Fragen und Problemen haben diese Arbeit erst möglich gemacht.

Allen ehemaligen und aktuellen Mitgliedern der Arbeitsgruppe Temps danke ich für die große Hilfsbereitschaft und das tolle Arbeitsklima während der letzten Jahre. Ohne euch hätte es nur halb so viel Spaß gemacht!

Großer Dank gilt Dr. Joachim Gripp für seine Unterstützung bei allen Arbeiten im Chemielabor und seine immerwährenden Bemühungen das Chaos nicht zu groß werden zu lassen.

Ganz besonders danke ich Katharina und Julia, nicht nur für die immense Hilfe im Femtolabor und bei wissenschaftlichen und nichtwissenschaftlichen Fragen, sondern auch für die Unterstützung in allen übrigen Lebenslagen. BMF!

Alexander Thrun danke ich dafür, dass er mich durch die gesamte Diplomarbeits- und Promotionszeit begleitet hat, sei es durch seine Hilfe bei technischen Problemen und Latex-Fragen oder einfach nur durch seine Fröhlichkeit bis hin zu absoluter Albernheit.

Ich danke auch Alexander, Hendrik, Michal, Tracy und Alexandra für die schöne gemeinsame Zeit in der LMS8 im Büro mit der schönsten Aussicht.

Katharina, Julia und Rebecca danke ich für das tolle Büro in der MES1, wo das geordnete Chaos und der Kommunismus regieren und wo seit 3 Jahren auch im Sommer Weihnachten ist.

I would like to thank Dr. Michal Malicki for introducing me to the art of nanoparticle synthesis and for his support during the early stages of this work.

Dank geht auch an meine Hiwis, F3-Praktikanten und Bachelorstudenten Dennis Bank, Sebastian Beil, Alexandra Dabrowski, Mark Dittner und Rebecca Stellmacher, die meine Arbeit wesentlich unterstützt und vorangebracht haben.

Ich bedanke mich außerdem bei allen Mitarbeitern der Werkstatt, Klaus-Dieter Will, Frank Laasch, Frank Herzog, Andreas Sievers und Olaf Wendt, und natürlich auch den technischen Mitarbeitern, Uwe Eggers, Michael Karstens und Klaus Warns, für die Hilfe bei den diversen kleinen und größeren technischen Problemchen.

Unseren Sekretärinnen Ursula von der Heydt und Tanja Sharif danke ich für die stetige Unterstützung und schnelle und unbürokratische Hilfe bei allen möglichen Dingen des Alltags.

Ich danke außerdem Dr. Ulrich Schürmann und Dr. Venkata Sai Kiran Chakravadhanula von der technischen Fakultät für die Durchführung der vielen TEM-Messungen über die Jahre.

Für das Korrekturlesen der Arbeit danke ich Julia, Katharina und Dennis.

Meinen Freunden danke ich für die vielen fröhlichen Stunden und Abende dir wir auf diversen Feiern oder auch einfach ohne einen besonderen Anlass zusammen verbracht haben. Ihr seid klasse!

Jag tackar också Raja för att göra det så enkelt att lära svenska. Det var alltid roligt med dig, tack så mycket!

Meiner Familie danke ich für ihre rückhaltlose Unterstützung, das sichere Gefühl eine Heimat zu haben und die Gewissheit, dass ich mich immer auf euch verlassen kann. Die vergangenen 10 Jahre wären ohne euch einfach nicht möglich gewesen!